CYRIC

ANNUAL REPORT

2014-2015

(January 2014 - December 2015)

CYCLOTRON AND RADIOISOTOPE CENTER
TOHOKU UNIVERSITY

CYRIC

ANNUAL REPORT

2014-2015

(January 2014 - December 2015)

CYCLOTRON AND RADIOISOTOPE CENTER
TOHOKU UNIVERSITY
http://www.cyric.tohoku.ac.jp/

PREFACE

CYRIC was established in 1977 as an institution for carrying out multidisciplinary research with the cyclotron and radioisotopes, and for training researchers of Tohoku University for safe treatment of radioisotopes and radiations. The cyclotron of CYRIC was manufactured by Sumitomo Heavy Industry Inc., Japan, form the design of CGR-Mev, France. The first beam was extracted at the end of December 1977. The scheduled operation of the cyclotron for research studies started in July 1979. We usually operate the cyclotron four whole days a week for research studies. The Great East Japan Earthquake occurred on March 11, 2011, the accelerator facilities were severely damaged because of strong shaking that continued for a few minutes. We have made great efforts on the recovery of our daily research activities until now. Fortunately, the scheduled operation of the cyclotron for collaborative research studies has re-started since October, 2012 from the one year and half interruption of our services. CYRIC consists of four buildings: cyclotron building (5400 m^2), radioisotope building (2000 m^2), molecular imaging research building (1000 m^2), and CYRIC Collaboration building (250 m^2). As the example of medical and pharmaceutical fields, our CYRIC demonstrated the usefulness of FDG-PET scans in patients with cancer for the first time in early 1980's. Other highly respected achievement of CYRIC is the application of molecular imaging to drug development including the imaging of neurotransmitter receptors and amyloid and tau proteins in Alzheimer disease. Fully functioning CYRIC facilities can ensure the further development of molecular imaging in near future.

In conformity with the aim of establishment of CYRIC, the cyclotron has been used for studies in various fields of research, such as nuclear physics, nuclear chemistry, solid-state physics and element analysis by PIXE and activation, and for radioisotope production for use in engineering, biology, pharmaceutical science and medicine. Six divisions (Division of Accelerator, Division of Instrumentations, Division of Radio-pharmaceutical Chemistry, Division of Cyclotron Nuclear Medicine, Division of Radiation Protection and Safety Control, and Division of Geriatric Behavioral Neurology) work for maintenance, development of facilities, and for studies of their individual research fields. The divisions belong to the graduate schools of Tohoku University.

Both the K=110 MeV AVF cyclotron and the K=12 MeV AVF cyclotron have been

steady operated in the last two years. Cocktail beams of a mass-to-charge ratio to 5, $^{129}Xe^{5+}$ - 454 MeV, $^{84}Kr^{17+}$ - 323 MeV, $^{40}Ar^{8+}$ - 150 MeV, $^{20}Ne^{4+}$ - 75 MeV, and $^{15}N^{3+}$ - 56 MeV, have been developed and started being provided for beam time using the 10 GHz ECR ion source. With the cocktail acceleration technique, the quick switch of the ion species and the beam energy has been realized. Moreover, the ions of ^{28}Si and ^{56}Fe extracted from solid materials, such as quartz and stainless steel, were also newly been provided for beam times at CYRIC.

The development of the laser cooled RI beam line constructed at TOF trough TR5 has been continued. This new beam line is used to study the fundamental physics using heavy elements such as an electric dipole moment (EDM) of francium atoms, and will be extended for the research on atomic physics and radiation chemistry. The thermal ionizer, neutralizer and optical trapping system are ready, and the improvement to realize the high trapping efficiency is in progress. The development of the atom interferometer to measure the EDM was also performed, and Dr. T. Hayamizu, who was PD at CYRIC, received Inoue Research Award for Young Scientists for this work.

In the research program on proton therapy, a micro-pattern gaseous detector (MPGD) based on gas electron multiplier technology (GEM detector) has been developed and applied as a new transmission beam monitor for charged particle therapy to simultaneously measure a two-dimensional beam profile and the amount of dose of the therapeutic charged-particle beam. Following the recent success of the prototype detector, a new MPGD monitor which can be applied to clinical situations was developed. The feasibility tests were successfully performed using an 80-MeV proton beam and the beam irradiation system for proton therapy experiments installed in the experimental room 5.

Translational research on radiopharmaceuticals for positron emission tomography (PET) made satisfactory progress during the reporting period. [^{18}F]THK-5351, an original new PET tracer for tau imaging, entered the first-in-human study in September 2014 and played the leading role in clinical PET studies on dementia. Overall, the rate of supply of PET tracers for tau and amyloid-β came to be higher than that of other PET tracers. It should be mentioned that in-house preparation and supply of [^{18}F]FDG was terminated because [^{18}F]FDG is now commercially available by delivery. PET tracers prepared and supplied for clinical studies in the two years were [^{18}F]THK-5351 (29 preparations), [^{18}F]THK-5117 (3), [^{11}C]doxepin (11), [^{11}C]raclopride (10), [^{11}C]BF-227 (24), [^{11}C]PiB (44), and [^{15}O]water (4).

Preclinical research on relationship between structure and activity of 2-arylquinoline derivatives revealed a precise binding characteristics of [^{18}F]THK-5351 as a tau imaging tracer. Based on the findings of the study, several backup compounds for THK-5351 were

newly designed and synthesized. Preclinical development of other type of PET tracers were also advanced steadily. For examples, we succeeded to prepare a ^{11}C-labeled scFv antibody by using [^{11}C]MET and cell-free protein synthesis system. In addition, we developed a novel convenient method for radiosynthesis of ^{18}F-labeled phosphonium compounds that could be useful for imaging tissues rich in mitochondria such as myocardium. Furthermore, research on nucleophilic radiofluorination of aromatic compounds had started and are yielding some encouraging results.

Various clinical PET studies were published in 2014 to 2015, including studies on brain, heart and skeletal muscles. A follow-up study of tau accumulation in Alzheimer's disease (AD) patients using [^{18}F]THK-5117 had a very high impact in the fields of gerontology, neurology and psychiatry. This study was in a strong association with another brain PET study on amyloid β accumulation in AD patients with or without diabetes mellitus using [^{11}C]BF-227. Additional important study was a measurement of histamine H_1 receptor occupancy for levocetirizine, a new-generation antihistamine, using [^{11}C]Doxepin in healthy volunteers. This study was also associated with a car driving study using a driving simulator. These studies were conducted in collaboration with a major pharmaceutical company, and this kind of study might increase in near future. A new study that showed an association between the prognosis and [^{18}F]FDG uptake in the right ventricular free wall of pulmonary hypertension patients was also very important in the field of cardiology. Skeletal muscle imaging using [^{18}F]FDG has been getting more and more popular in the field of not only sports medicine but also in orthopedic surgery. In addition, recent achievement at CYRIC in education on scientific visualization is also reported.

The research program on PIXE analysis has been carried out by using a 4.5 MV Dynamitron accelerator at the Fast Neutron Laboratory, Graduate School of Engineering, Tohoku University, under the scientific tip up between CYRIC and FNL. A high-current microbeam system (MB-II), which is dedicated to chemical state mapping was installed. Energy resolution of the accelerator was improved by developing the terminal voltage stabilizing system (TVSS) to get better performance of these microbeam systems. Research studies using submilli-PIXE camera, microbeam analysis systems, and micron-CT has been carried out. A total of 1500 hours of beam-time including test was served to this program without serious problems in FY2014 and 2015.

We conducted the beginners training for safe handling of radiation and radioisotopes twice a year in 2014 and 2015 for staffs and students of Tohoku University. The courses

included 1) Radiositopes and radiation generators (412 trainees in 2014 and 431 trainees in 2015), 2) X-ray machines and electron microscope (347 trainees in 2014 and 343 trainees in 2015), and 3) Synchrotron Radiation (113 trainees in 2014 and 119 trainees in 2015). The total numbers of trainees in English classes for foreign students and scientists were 84 in 2014 and 103 in 2015, respectively.

There were no persons who were exposed occupational radiation more than 5.0 mSv among 233 (2014) and 244 (2015) radiation workers at CYRIC.

The aim of Division of Geriatric Behavioral Neurology is to study the neuroscience of dementia and contribute to the welfare of elderly people. Our work in the northern area of Miyagi prefecture has always been our priority. Since 1988, our research group and the town of Tajiri (now the city of Osaki) have been performed the community-based stroke and dementia prevention (the Osaki-Tajiri Project), followed by the similar projects in the cities of Kurihara, Tome, and Wakuya. We have reported the prevalence and incidence of dementia, and clinical validity of drug treatment and/or psychosocial intervention with reference to PET examinations using the following tracers: [^{15}O]oxygen, [^{11}C]CO, [^{18}F]fluorodeoxy glucose, [^{18}F]fluorodopa, [^{11}C]YM-09151-2, and [^{11}C]donepezil. Unfortunately, dementia patients in a community do not always receive an adequate medical and welfare management based on a scientific evidence including diagnosis of dementing diseases, psychosocial intervention, and caregiver education. Therefore, the Division of Geriatric Behavioral Neurology aims the followings: 1) to establish a method for assessing cognitive functions of older adults and database; 2) to develop a comprehensive model for dementia including medical and welfare management based on the neurological basis; and 3) to improve the level of medical and welfare for dementia and education.

We are most grateful to Tohoku University and to the Ministry of Education, Sports, Culture, Science and Technology for continuous support.

December 2016

Kazuhiko YANAI, Director
Masatoshi ITOH
Yasuhiro SAKEMI
Atsuki TERAKAWA
Shozo FURUMOTO
Manabu TASHIRO
Shigeo MATSUYAMA
Hiroshi WATABE
Kenichi MEGURO

CONTENTS

I. NUCLEAR PHYSICS

I. 1. Proton-^{3}He Scattering at 70 MeV with Polarized ^{3}He Target ····· *1*
Wada Y., Watanabe A., Sekiguchi K., Akieda T., Eto D., Itoh M., Kon H., Miki K., Mukai T., Nakai S., Shiokawa Y., Uesaka T., and Wakui T.

I. 2. Measurement of the α Decay from the Broad 10 MeV State in ^{12}C ····· *4*
Itoh M., Ando S., Aoki T., Arikawa H., Harada K., Hayamizu T., Inoue T., Ishikawa T., Kato K., Kawamura K., Sakemi Y., and Uchiyama A.

I. 3. Experiment of Measurement of Elastic Scattering for the Search for α-cluster Gas-like Structure in ^{13}C ····· *8*
Nasu Y., Itoh M., Hayamizu T., Matsuda Y., and Okamoto J.

I. 4. Fourth Training School on Nuclear and Particle Physics Experiments Using Accelerator Beams ····· *12*
Inoue T., Sakemi Y., Itoh M., Dammalapati U., Harada K., Kawamura H., Kato K., Aoki T., Uchiyama A., Ito S., Kaneda M., and Tamura H.

II. NUCLEAR INSTRUMENTATION

II. 1. A Wien Filter as a Mass Filter to Purify the Francium Beam ····· *13*
Kawamura H., Aoki T., Arikawa H., Harada K., Hayamizu T., Inoue T., Ishikawa T., Ito S., Itoh M., Kato K., Koehler L., Mathis J., Sakamoto K., Uchiyama A., and Sakemi Y.

II. 2. Present Status of the Development of an Optical Dipole Force Trap System towards the Electron Electric Dipole Moment Search ····· *17*
Harada K., Hayamizu T., Kato K., Sakamoto K., Kawamura H., Inoue T., Arikawa H., Ishikawa T., Aoki T., Uchiyama A., Ito S., Ando S., Itoh M., Aoki T., Hatakeyama A., Dammalapati U., and Sakemi Y.

II. 3. Development of an Electric Field Application System toward the Electron EDM Search Experiment ····· *20*
Inoue T., Ando S., Aoki T., Arikawa H., Dammalapati U., Harada K., Hayamizu H., Ito S., Itoh M., Kato K., Kawamura H., Uchiyama A., and Sakemi Y.

II. 4. Development of the $^{28}Si^{9+}$ Ion Beam toward the Search for Alpha Cluster Gas State in ^{28}Si ····· *23*
Okamoto J., Itoh M., Hayamizu T., and Nasu Y.

III. NUCLEAR ENGINEERING

III. 1. Development of a Multi-channel Charge-readout System for a Micro-pattern Gaseous Detector ····· *27*
Terakawa A., Ishii K., Matsuyama S., Sato T., Inano K., Sakemi Y., and Fujiwara T.

III. 2. Three-dimensional Imaging of Human Cells by Using PIXE-μ-CT ····· *30*
Matsuyama S., Ishii K., Toyama S., Watanabe K., Koshio S., Kasahara K., Ito S., Terakawa A., Fujiwara M., Ortega R., Carmona A., and Roudeau S.

IV. PIXE AND ENVIRONMENTAL ANALYSIS

IV. 1. Development of a High-current Microbeam System ····· *37*
Matsuyama S., Ishii K., Suzuki S., Terakawa A., Fujiwara M., Koshio S., Toyama S., Ito S., Fujisawa M., and Nagaya T.

IV. 2. Development of the Terminal Voltage Stabilizating System of the Dynamitron Accelerator ····· *42*
Matsuyama S., Fujisawa M., and Nagaya T.

V. RADIOCHEMISRTY AND NUCLEAR CHEMISTRY

V. 1. Measurement of Alpha-induced Reaction Cross Sections for Cr Isotopes on Natural Ti ····· *49*
Kikunaga H., Takamiya K., Ohtsuki T., and Haba H.

VI. RADIOPHARMACEUTICAL CHEMISTRY AND BIOLOGY

VI. 1. Concentration of [^{11}C]Methyl Triflate for Microreactor Radiosynthesis of ^{11}C-Probes ····· *53*
Ishikawa Y., Iwata R., Terasaki K., and Furumoto S.

VI. 2. Preparation of [^{18}F]FRP-170 by Microfluidics and Solid-phase Extraction ··· *57*
Iwata R., Terasaki K., Takahashi K., Ishikawa Y., and Furumoto S.

VI. 3. Structure-activity Relationship Study of 2-Arylquinoline Derivatives for Tau Imaging in Alzheimer's Disease ····· *62*
Tago T., Furumoto S., Okamura N., Harada R., Adachi H., Ishikawa Y., Yanai K., Iwata R., and Kudo Y.

VI. 4. Development of ^{18}F-labeled Phosphonium Derivatives for Mitochondria Imaging by PET ····· *66*
Furumoto S., Tominaga T., Itoh H., Ishikawa Y., and Iwata R.

VI. 5. Development of ^{18}F-labeling Method for Proteins Using a Cell-free Translation System and ^{18}F-fluoro-L-proline ····· *69*
Harada R., Furumoto S., Yoshikawa T., Ishikawa Y., Iwata R., and Yanai K.

VI. 6. Measurement of Free Fraction in Plasma for Biomathematical Prediction of *SUVR* of Amyloid PET Radiotracers ····· *73*
Nai Y.-H., Shidahara M., Seki C., Watanuki S., Funaki Y., Ishikawa Y., Furumoto S., and Watabe H.

VII. NUCLEAR MEDICINE

VII. 1. Longitudinal Assessment of Tau Pathology in Patients with Alzheimer's Disease Using [^{18}F]THK-5117 Positron Emission Tomography ····· *79*
Ishiki A., Okamura N.,, Furukawa K., Furumoto S., Harada R., Tomita N., Hiraoka K., Watanuki S., Ishikawa Y., Funaki Y., Iwata R., Tashiro M., Yanai K., Kudo Y., and Arai H.

VII. 2. Enhanced [^{18}F]Fluorodeoxyglucose Accumulation in the Right Ventricular

Free Wall Predicts Long-term Mortality of Patients with Pulmonary Hypertension ····· *82*
Tatebe S., Fukumoto Y., Oikawa-Wakayama M., Sugimura K., Satoh K., Miura Y., Aoki T., Nochioka K., Miura M., Yamamoto S., Tashiro M., Kagaya Y., and Shimokawa H.

VII. 3. Brain Histamine H_1 Receptor Occupancy after Oral Administration of Levocetirizine: a PET Study ····· *85*
Hiraoka K., Tashiro M., Grobosch T., Maurer M., Oda K., Toyohara J., Ishii K., Ishiwata K., and Yanai K.

VII. 4. Muscle Activity Pattern of the Shoulder External Rotators Differs in Adduction and Abduction: an Analysis Using Positron Emission Tomography ····· *88*
Kurokawa D., Sano H., Nagamoto H., Omi R., Shinozaki N., Watanuki S., Kishimoto K.N., Yamamoto N., Hiraoka K., Tashiro M., and Itoi E.

VII. 5. Brain Accumulation of Amyloid Protein Visualized by PET and BF-227 in Alzheimer's Disease Patients with or without Diabetes Mellitus ····· *91*
Tomita N., Furukawa K., Okamura N., Tashiro T., Une K., Furumoto S., Iwata R., Yanai K., Kudo Y., and Arai H.

VII. 6. A Simulated Car-driving Performance on the Effects of Administration of Levocetirizine, Fexofenadine, and Diphenhydramine in Healthy Japanese Volunteers ····· *95*
Inami A., Matsuda R., Grobosch T., Komamura H., Yamada Y., Ito T., Koike D., Takeda K., Miyake M., Hiraoka K., Maurer M., Yanai K., and Tashiro M.

VIII. RADIATION PROTECTION AND TRAINING OF SAFETY HANDLING

VIII. 1. Beginners Training for Safe Handling of Radiation and Radioisotopes at Tohoku University ····· *101*
Watabe H., Ohtomo K., Mayama F., Tojo I., Miyake Y., and Yuki H.

VIII. 2. Radiation Protection and Management ····· *105*
Yuki H., Ohtomo K., Watabe H., and Nakae H.

IX. Scientific Visualization

IX. 1. Educational Practice of Scientific Visualization at CYRIC ····· *107*
Ariga K. and Tashiro M.

X. PUBLICATIONS ····· *113*

XI. MEMBERS OF COMMITTEES ····· *127*

XII. STAFF AND STUDENTS ····· *133*

I. NUCLEAR PHYSICS

I. 1. Proton-^{3}He Scattering at 70 MeV with Polarized ^{3}He Target

Wada Y.[1], Watanabe A.[1], Sekiguchi K.[1], Akieda T.[1], Eto D.[1], Itoh M.[2], Kon H.[1], Miki K.[1], Mukai T.[1], Nakai S.[1], Shiokawa Y.[1], Uesaka T.[3], and Wakui T.[2]

[1]*Department of Physics, Tohoku University*
[2]*Cyclotron and Radioisotope Center, Tohoku University*
[3]*RIKEN Nishina Center*

One of the main interests in nuclear physics is understanding the forces acting between nuclear constituents. A hot topic in the study of nuclear forces is to clarify the roles of three-nucleon forces (3NFs) in nuclei, and to describe various phenomena of nuclei by explicitly taking into account nucleon-nucleon (NN) interactions combined with 3NFs. The 3NFs arise naturally in the standard meson exchange picture[1)] as well as in the framework of chiral effective field theory which has a link to QCD[2)]. Few-nucleon scattering offers good opportunities to investigate dynamical aspects of these forces, such as momentum, spin, and iso-spin dependencies. First indication of the 3NFs in the scattering system was pointed out in the cross section minimum for nucleon-deuteron elastic scattering at intermediate energies (E/A> about 60 MeV). Since then nucleon-deuteron elastic scattering at incident energies of up to around 300 MeV have been extensively performed both experimentally and theoretically[3)]. The nucleon-deuteron scattering has provided an solid basis to nail down detailed properties of 3NFs, however, the total isospin channel of the 3NFs is limited to T=1/2. Recently importance of the iso-spin dependence study of 3NFs have been pronounced for understanding of nuclear system with larger-isospin asymmetry, e.g. neutron-rich nuclei, neutron matter, and neutron stars[4)]. The p+^{3}He scattering is an attractive probe since this system is the simplest one where the 3NFs in the channels of total isospin T=3/2 can be studied. In order to explore the properties of three-nucleon forces via proton-^{3}He scattering we are planning the measurements of ^{3}He analyzing powers at 70 MeV. We started construction of polarized ^{3}He target as well as the detection system in 2013[5)].

Schematic view of the polarized ^{3}He target is shown in Fig. 1. Spin-exchange optical pumping method is adopted for polarizing ^{3}He nucleus[6], where Rb atoms are polarized by optical pumping and their polarizations are transferred to ^{3}He nucleus by hyper-fine interactions. The target cell consists of double chamber which includes the target chamber and the optical pumping one. Both are connected by a thin transfer tube. This is designed to separate the target chamber from the optical pumping one which needs external oven to produce Rb vapor. The target cell contains the ^{3}He gas with pressure of 3 atm at room temperature together with a small amount of N_2 gas and Rb vapor. During operation the pumping chamber is heated to about 430 K to provide a high Rb vapor density and maintain the polarization of ^{3}He nucleus. Circularly polarized photons with power of 30 W are used to optically pump Rb atoms. Polarized ^{3}He nuclei are allowed to diffuse into the target chamber. The target cell is made of GE180 glass which is known to have a very long relaxation time for the polarization of ^{3}He. The polarizations are monitored by the adiabatic fast passage (AFP) NMR method. The NMR signals give relative values of the polarization. The absolute values of the target polarization are calibrated by using frequency shift of the electron spin resonance of Rb atoms. Typical values of polarizations are 10% now[7].

Experiments with 70 MeV proton beams in conjunction with the newly developed polarized ^{3}He target were performed at the room TR4. Proton beams bombarded the polarized ^{3}He target and they were stopped in the faraday cup. Beam intensities were about 5 nA during the experiment. Scattered protons at 55 and 70 degrees in the laboratory system were detected by the *dE-E* scintillation counters. They consisted of a plastic scintillator with thickness of 1mm and a NaI(Tl) scintillator with thickness of 55 mm. In the measurement we successfully obtained asymmetry of the events from proton-^{3}He scattering.

Further developments of the polarized target, e.g. to increase laser power, to reduce spin relaxation time, are now in progress to obtain high polarization. This is necessary to obtain high precision analyzing power data.

References

1) Fujita J, Miyazawa H, *Prog Theor Phys* **17** (1957) 360.
2) Epelbaum E, *Prog Part Nucl Phys* **57** (2006) 654.
3) Sekiguchi K, et al., *Phys Rev* C **65** (2002) 034003; *ibid,* **89** (2014) 064007.
4) For example, Pieper SC, et al., *Phys Rev* C **64** (2001) 014001; Demorest PB, et al., *Nature* **467** (2010) 1081; Gandolfi S, et al., *Phys Rev* C **85** (2012) 032801.

5) Wada Y, Master thesis, Tohoku University (2014).
6) Happer W, et al., *Phys Rev* A **29** (1984) 3092.
7) Watanabe A, Master thesis, Tohoku University (2016).

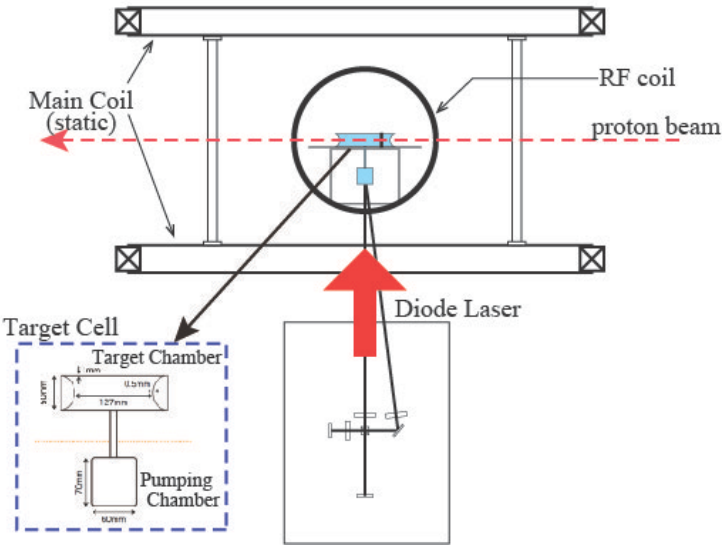

Figure 1. Schematic view of the polarized ^{3}He target.

I. 2. Measurement of the α Decay from the Broad 10 MeV State in ^{12}C

Itoh M., Ando S., Aoki T., Arikawa H., Harada K., Hayamizu T., Inoue T., Ishikawa T., Kato K., Kawamura K., Sakemi Y., and Uchiyama A.

Cyclotron and Radioisotope Center, Tohoku University

The α cluster structure in the nucleus becomes one of active topics in recent years, again. Stimulating the concept of the α cluster gas as the Bose gas proposed by Tohsaki *et al.*[1], many researches have been performed theoretically and experimentally. The broad 10 MeV state in ^{12}C is considered to be one of the α gas-like states. According to the 3α orthogonality condition model with a complex scaling method, the broad 0^+ state around 10 MeV is considered to be a higher nodal of the second 0^+ state at 7.65 MeV in ^{12}C[2]. However, a variational calculation after spin-parity projection in the framework of antisymmetrized molecular dynamics indicates a linear-like 3α structure appears around 10 MeV in ^{12}C[3]. Recently, it was reported that the broad 10 MeV state consisted of two 0^+ components[4,5]. In this experiment, we investigated the decay property of the broad 10 MeV state in order to verify and study these two 0^+ states.

The measurement was performed with a large scattering chamber at the 41 course in CYRIC. The $^{12}C^{4+}$ beam accelerated up to 110 MeV bombarded the self-supported natural carbon foil with a thickness of 104 μg/cm^2. The experimental setup is shown in Fig. 1. The beam was stopped at a Neodymium magnet just in front of the silicon strip detector. Inelastically scattered ^{12}C beam, excited to the broad 10 MeV state, was immediately broken to three alpha particles. Since break-up three alpha particles had almost same kinetic energy per nucleons, they were easily detected even with a relatively small solid angle detector. Two double-sided silicon strip detectors (DSSD) were used as shown in Fig. 1. DSSD1 has horizontally 16 channels and vertically 16 channels with a size of 50 × 50 mm^2 and a thickness of 1500 μm. DSSD2 has horizontally 40 channels and vertically 40 channels with a size of 40 × 40 mm^2 and a thickness of 1000 μm. To reduce numbers of readout channels, two or

three strips were connected into a channel. Then, the total readout channels were reduced into 32 channels.

Figure 2 shows the energy spectrum around the broad 10 MeV state measured in this experiment. The center of mass angle for three break-up alpha particles was limited within 4.8 degrees. The prominent peak is the 9.641 MeV 3^- state. The broad hill at both side of the 3^- state is the broad 10 MeV state. The broad 10 MeV state was divided into four parts, as shown in Fig. 2, in order to see the energy dependence for the decay branch. In each energy region, the energy distribution of break-up three alpha particles was compared with those obtained in the Monte-Carlo simulation for two decay mechanisms as the decay through the ground state of ^{8}Be, ^{8}Be(g.s.), and that through the first 2^+ state of ^{8}Be, ^{8}Be(2^+). In this case, the direct 3α decay could not be distinguished from the ^{8}Be(2^+) channel. Figure 3 shows the preliminary results of the comparison between the experiment and the Monte-Carlo simulation. The experimental data are plotted with closed circles. The red dashed, the cyan solid, and the green dotted lines show the energy distributions obtained in the Monte-Carlo simulations for the ^{8}Be(g.s.), the ^{8}Be(2^+), and the sum of these two channels, respectively. The experimental energy distribution was reproduced well with the sum of the ^{8}Be(g.s.) and ^{8}Be(2^+) channels. The energy dependence for the branching ratio of the ^{8}Be(g.s.) channel is shown in Fig. 4. Open and closed circles indicate results of the RCNP experiment obtained in Ref. 5 and of the CYRIC experiment, respectively. While branching ratios of the ^{8}Be(g.s.) channel obtained in the RCNP experiment suddenly drop at the excitation energy of 10.8 MeV, those obtained in the CYRIC experiment gradually go down. Since the momentum transfer of the reaction in the CYRIC experiment was larger than that in the RCNP experiment, the energy spectrum at CYRIC in Fig. 1 contains higher multipole components, such as the 1^- state at 10.8 MeV and the 2^+ state at 10 MeV. According to the experiment by Alcorta *et al.*[6], the 1^- state at 10.8 MeV decays 100% through the ^{8}Be(g.s.) channel. Therefore, the branching ratio of the ^{8}Be(g.s.) channel around 11 MeV became nearly 90%. We need to estimate the contributions from higher multipole components, correctly. The estimations for the higher multipole contributions are in progress.

References

1) Tohsaki A, *et al.*, *Phys Rev Lett* **87** (2001) 192501.
2) Kurokawa C, Katō K, *Nucl Phys A* **792** (2007) 87; Kurokawa C, Katō K, *Phys Rev C* **71** (2005) 021301.
3) Kanada-Enyo Y, *Prog Theor Phys* **117** (2007) 655.

4) Itoh M, *et al*., *Phys Rev C* **84** (2011) 054308.
5) Itoh M, *et al*., *J Phys Conf Ser* **436** (2013) 012006.
6) Alcorta M, *et al*., *Phys Rev C* **86** (2012) 064306.

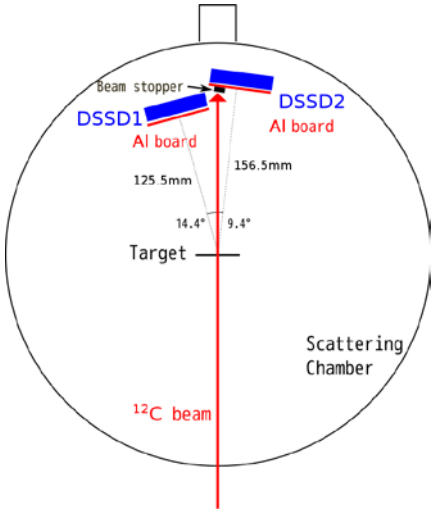

Figure 1. Experimental set-up.

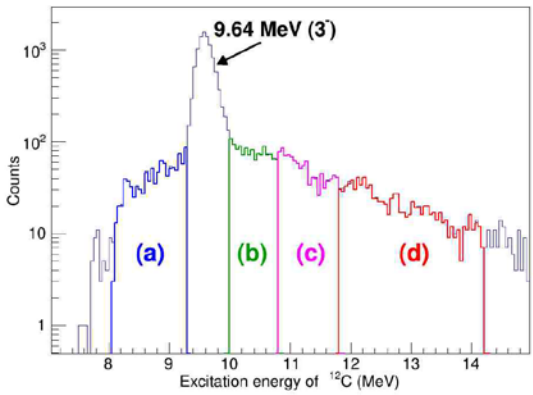

Figure 2. Energy spectrum around the broad 10 MeV state.

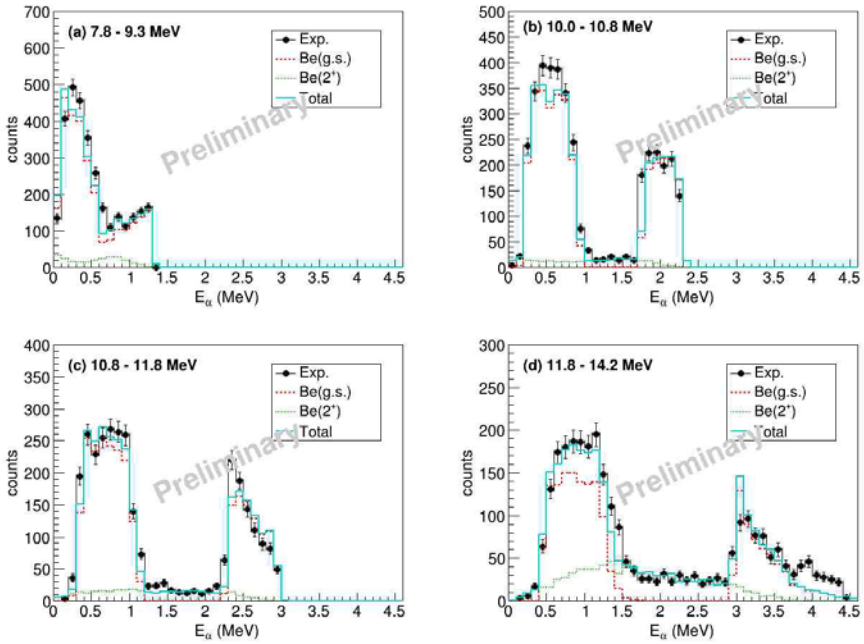

Figure 3. Energy distributions of decay α particles in the broad 10 MeV state.

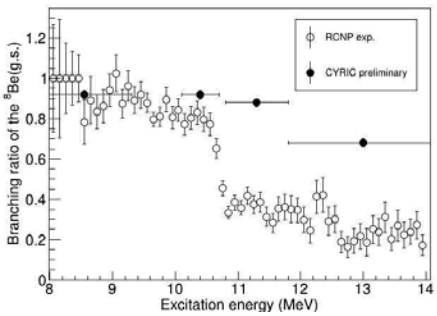

Figure 4. Energy dependence of the branching ratio to the ^{8}Be(g.s.) channel.

I. 3. Experiment of Measurement of Elastic Scattering for the Search for α-cluster Gas-like Structure in ^{13}C

Nasu Y., Itoh M., Hayamizu T., Matsuda Y., and Okamoto J.

Cyclotron and Radioisotope Center, Tohoku University

α-cluster structures appear in excited states in 4*N*-light nuclei which have equal numbers of protons and neutrons. For example, the Hoyle state, which is the second 0^+ state at E_x = 7.65 MeV in ^{12}C, is well studied experimentally and theoretically. The Hoyle state is considered to have a dilute gas-like structure in which the α cluster is loosely coupled to each other[1,2]. This structure is called an α gas-like structure.

The α gas-like structure is also considered to appear in $A \neq 4N$ light nuclei. In this report, we focus on the α gas-like structure in ^{13}C. At the Research Center for Nuclear Physics (RCNP), Osaka University, the $1/2^-_4$ state was found at E_x = 12.5 MeV by the measurement of inelastic α scattering at extremely forward angle[3]. This state is a candidate for the α gas-like structure in ^{13}C. On the other hand, according to Orthogonality Condition Model (OCM) calculation, the $1/2^+_5$ state at E_x= 14.9 MeV is considered to have the α gas-like structure, although the state have not been identified experimentally, yet[4]. Therefore, it is intriguing to make sure these predictions and investigate the role of the excess neutron in the α gas-like structure.

To study the α gas-like structure in ^{13}C, we plan to measure the decay 3α particles via the ^{12}C(^{13}C, ^{13}C*$(1/2^-_4)$[3α+n])^{12}C reaction at the 41 course in CYRIC. For the experiment, it is important to optimize the experimental setup for detecting three α particles from ^{13}C*$(1/2^-_4)$. In order to estimate the cross section with the Distorted Wave Born Approximation (DWBA) calculation, we measured the angular distribution for the ^{12}C(^{13}C, ^{13}C)^{12}C reaction and obtained the optical potential parameters.

The experiment was performed at the 41course. Figure 1 shows the experimental setup in the scattering chamber. The $^{13}C^{4+}$ beam was accelerated up to 129 MeV with the AVF cyclotron and bombarded on a self–supported natural carbon foil with a thickness of 100

μg/cm^2 installed in the scattering chamber. Recoil ^{12}C particles were detected in three Si detectors (SDs).

Figure 2 shows the obtained angular distribution of elastic scattering. The angular distribution was fitted to obtain optical potential parameters. The optical potential[5] is written as

$$U(r) = -V_0 \mathrm{f}(r, r_0, a_0) - iW\mathrm{f}(r, r_i, a_i) ,$$
$$f(r, r_{0/i}, a_{0/i}) = \frac{1}{1 + exp(\frac{r - r_{0/i}A^{1/3}}{a_{0/i}})} ,$$

where V_0 and W represent the real and imaginary parts, respectively, r is the distance between the centers of a projectile and a target, r_i is the nuclear radius, and a_i is the diffuseness. The potential has six independent parameters. In order to obtain parameters, roughly, five parameters (V_0, r_0, a_0, W, r_i) were fixed to those obtained in Ref 6), and the parameter, a_i was determined to fit the angular distribution of elastic scattering. Table 1 shows the obtained optical potential parameters.

We calculated the angular distribution of the ^{12}C(^{13}C, ^{13}C*(1/2$^-_4$))^{12}C reaction using the obtained optical potential and DWBA code DWUCK4[7]. The calculated angular distribution of the ^{12}C(^{13}C, ^{13}C*(1/2$^-_4$)[3α+n])^{12}C reaction is shown in Fig 2. The distribution indicates the diffraction maxima appear around θ_{cm} = 0°, 7.5°, 15°, 22°. We determined that the measurement angle is θ_{cm} = 22°. At this angle, the recoil particle energy is sufficiently high to measure with a SD. In the laboratory frame, the corresponding angles of the recoil ^{12}C and scattered ^{13}C* are 60° and 10°, respectively. Figure 3 shows a schematic view of the next experimental setup. Two double-sided silicon strip detectors (DSSDs) with a size of 50 × 50 mm^2 and a 1 mm strip DSSD with a size of 40 × 40 mm^2 will be used for the detection of 3α particles and recoil ^{12}C particles, respectively.

In summary, the configuration of the next experimental setup for measurement the decay 3α particles via the ^{12}C(^{13}C, ^{13}C*(1/2$^-_4$)[3α+n])^{12}C reaction was determined by measurement of the angular distribution for the ^{12}C(^{13}C, ^{13}C)^{12}C reaction. We expect to obtain a new knowledge of the role of the excess neutron in the α gas-like structure.

References

1) Uegaki E, et al., *Prog Theor Phys* **57** (1977) 1262.
2) Kamimura K, *Nucl Phys* A **351** (1981) 456.
3) Sasamoto Y, et al., *Mod Phys Lett* A**21** (2006) 2393.
4) YamadaT and Funaki Y, *Phys ReV* C**92** (2015) 0343.

5) Mcfadden L, Satcher GR, *Nucl Phys* **84** (1966) 177.
6) Bohlen HG, et al., *Z Phys* A**322** (1985) 241.
7) Kunz PD, Computer code DWUCK4, unpublished.

Table 1. Obtained optical potential parameters.

V_0 (MeV)	r_0 (fm)	a_0 (fm)	W (MeV)	r_i (fm)	a_i (fm)
-175	0.65	0.79	-22.5	1.15	0.56

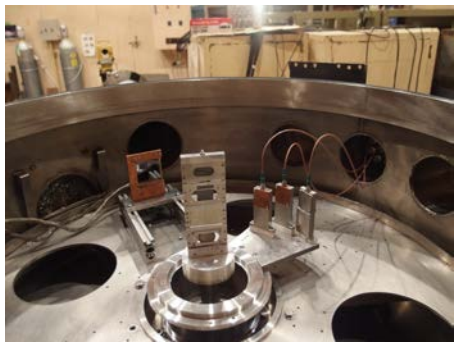

Figure 1. Inside of scattering chamber. The natural carbon foil target is placed at the center of the chamber. Three SDs are located at the right side of the chamber.

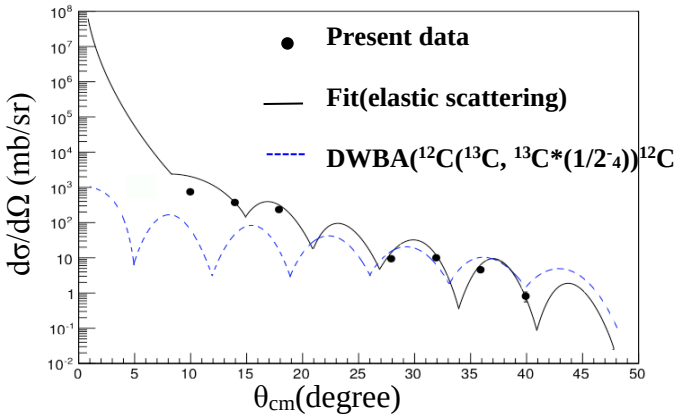

Figure 2. Angular distributions of elastic and inelastic scattering. Closed circles: present data; solid line: fitted result of elastic scattering; dashed line: DWBA calculation of the $^{12}C(^{13}C, ^{13}C^*(1/2^-_4))^{12}C$ reaction.

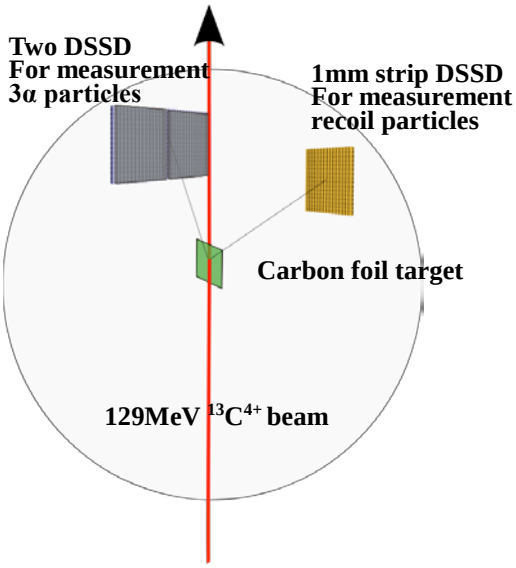

Figure 3. A schematic view of the setup for the planning experiment. Two DSSDs and 1mm strip DSSD are placed at angles determined in this experiment.

I. 4. Fourth Training School on Nuclear and Particle Physics Experiments Using Accelerator Beams

Inoue T.[1,2], Sakemi Y.[1], Itoh M.[1], Dammalapati U.[1], Harada K.[1], Kawamura H.[1,2], Kato K.[1], Aoki T.[1], Uchiyama A.[1], Ito S.[1], Kaneda M.[3], and Tamura H.[2]

[1]*Frontier Research Institute for Interdisciplinary Science, Tohoku University*
[2]*Cyclotron and Radioisotope Center, Tohoku University*
[3]*Department of physics, Tohoku University*

The 4th "Training school on nuclear and particle physics experiments using accelerator beams" (SCHOOL) in the Support Program of KEK and Tohoku University was held at CYRIC from February 22nd through 26th, 2016. The purpose of SCHOOL is to support the human resources development of Japanese accelerator science by having undergraduates who are interested in accelerator science, such as nuclear elementary particle physics or beam physics, experiment using the accelerator beam. The six participating students came from five universities (Yokohama National University, the University of Electro-Communications, Osaka University, Yamagata University and Keio University).

In the SCHOOL, the students had two experiments. One was an online experiment using an AVF cyclotron, and the other was offline. In the online experiment, francium (Fr), which is a radioactive element, was produced through the nuclear fusion reaction with the $^{18}O^{5+}$ primary beam accelerated by the AVF cyclotron and ^{197}Au target, as $^{18}O + {}^{197}Au \rightarrow {}^{215-x}Fr + xn$. The students actually performed the nuclear experiment using the accelerator by measuring the decay energy and the life time of the produced Fr nucleus using the solid state detector (SSD). In the offline experiment by using the americium sealed radioactive source, the operating principle of the SSD was studied and the SSDs were calibrated to be used in the online experiment. At the end of the SCHOOL, the students presented and discussed the training contents. Since all students were very active and hard workers, a bright future in Japanese accelerator science is expected.

The authors would like to thank the staff of CYRIC machine group. The SCHOOL will be held every year.

II. NUCLEAR INSTRUMENTATION

II. 1. A Wien Filter as a Mass Filter to Purify the Francium Beam

Kawamura H.[1,2], Aoki T.[2], Arikawa H.[2], Harada K.[2], Hayamizu T.[2,], Inoue T.[1,2], Ishikawa T.[2], Ito S.[2], Itoh M.[2], Kato K.[2], Koehler L.[2], Mathis J.[2], Sakamoto K.[2], Uchiyama A.[2], and Sakemi Y.[2,†]*

[1]*Frontier Research Institute for Interdisciplinary Sciences (FRIS), Tohoku University*
[2]*Cyclotron and Radioisotope Center, Tohoku University*

A factory of radioactive francium (Fr) atoms has been developed in order to better search for an electron's electric dipole moment and study the nuclear anapole moment[1,2)]. We can produce francium via a fusion-evaporation reaction of a gold target and an oxygen beam from 930 AVF cyclotron, and produce Fr ions with a thermal ionization on the surface of the hot gold. Various impurities, and gold itself, as well as francium will be ionized and become background components. Since electrostatic fields are used to extract and transport the produced ions, any ion can be extracted and transported independently of its mass. The low beam purity might negatively affect experimental processes, as the purity of the Fr beam was roughly 10^{-6}. The beam purity should be improved by using a Wien filter, which can separate the desired components from the others.

Figure 1 shows the aspect of the Fr factory, which has been built at the 51-beam course. The Wien filter was installed between the 1st and 2nd electrostatic quadrupole triplets. Figure 2 indicates the configuration of the filter electrodes. The beam component was analyzed using the filter. This study utilized the fact that the mass-charge ratio of the ion passing through the filter can vary by scanning the intensity of the electrical field with the fixed magnetic field. A typical result is shown in Fig. 3[4)]. The transverse axis shows the voltage difference between the electrodes with a gap of 60 mm, so the 100 V corresponds to the electric field 1.67 V/mm. The relation of the coil current to the magnetic field intensity is shown in Fig. 4. This result was obtained with the ions produced only by heating the target without the primary beam from the AVF cyclotron.

---

[*]*Present address: University of British Columbia, Vancouver, Canada*

[†]*Present address: Center for Nuclear Study (CNS), the University of Tokyo*

We can irradiate the gold target with a rubidium atomic beam and control the intensity of the rubidium ion. The beam current was measured with a copper plate (used as a Faraday cup) in a beam diagnosis system at just after the 2nd triplet. In Fig. 3, gray and black lines show events with and without the rubidium atomic beam, respectively. The peaks at ~600 V and ~500 V correspond to the rubidium ion and cesium ion, respectively, according to the mass-charge ratio expected from the intensity of the applied fields and the composition ratio of the rubidium source (Table 1[5]). Also, the peaks at ~900 V and ~1200 V are expected to be potassium and sodium as alkali elements. Potassium and sodium originate in the impurities of constructional elements of the apparatus because their peaks are not sensitive to being with/without a rubidium source. Massive gold is the best possible matter for this because every impurity of the gold target has a large ionization potential and is difficult to ionize (Table 2[6]). The peak corresponding to the mass-charge ratio ~200 had been observed by Stancari et al[7].

We confirmed that the Fr ion beam can be transported by removing light elements with the Wien filter. The transportation efficiency, which is defined as the ratio of the beam intensity reached the first diagnosis system and the final one, was 26%, while the transportation efficiency without the Wien filter was 15%. The facts that the beam condition was not so stable and that the transport efficiency had a fluctuation demonstrate why using the Wien filter led to better efficiency. The other possible reason is the fact that the electromagnetic field of the filter acts as a kind of focusing lens[8].

The beam purity is defined as the ratio between the number of francium measured by α-ray spectroscopy with a solid state detector and the total beam current measured by the copper plate. The beam purity was roughly 10^{-6} without filter and 10^{-3} with filter. This experiment demonstrated that the Wien filter can increase the beam purity thousandfold, though the intensity of the background components will vary with the surface condition of the gold target.

We gratefully acknowledge Hatanaka K., Tamii A., Yoshida H. P. and other staff of the RCNP at Osaka University for their donation of the Wien filter.

References

1) Kawamura H, et al., *Hyperfine Interact* **236** (2015) 53.
2) Kawamura H, et al., *Rev Sci Instrum* **87** (2016) 02B921.
3) KT Science Ltd., private communication (2014).
4) Aoki T, “Study of an ion to neutral atom conversion process for the search for the electron electric dipole moment (in Japanese)”, Master thesis, Tohoku University (2016).

5) Kurieto Shouji Ltd., private communication (2010).
6) Furuya Metal Co., Ltd., private communication (2015).
7) Stancari G, Corradi L, Dainelli A, *Nucl Instrum Meth A* **594** (2008) 321.
8) Arikawa H, "The development of the high purity francium beam toward the search for the violation of the fundamental symmetry (in Japanese)", Master thesis, Tohoku University (2015).

Table 1. Composition ratio of the rubidium source from KURIETO SHOUJI Ltd.[5].

Rb	99.9%
Na	< 13 ppm
K	< 13 ppm
Cs	639 ppm

Table 2. Composition ratio of the gold target from FURUYA METAL Co., Ltd.[6].

Au	> 99.99%
Ag	7 ppm
Cu	< 1 ppm
Fe	3 ppm
Pb	< 10 ppm
Pd	2 ppm

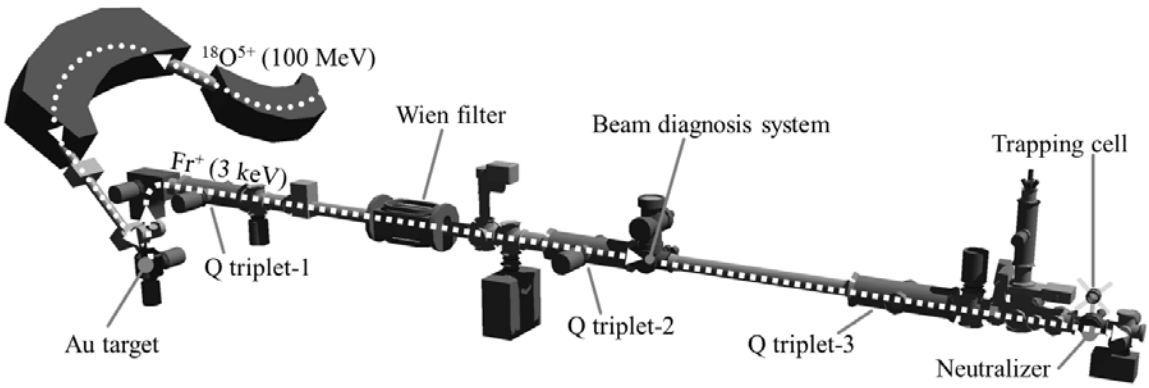

Figure 1. A factory of laser-cooled radioactive francium atoms.

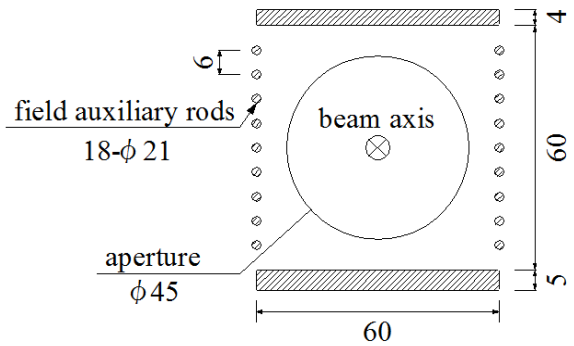

Figure 2. Transverse cross-section of main electrodes of the Wien filter (in units of mm) [3]. The auxiliary rods connect the two main electrodes with stepwise voltages. The longitudinal length is 260 mm.

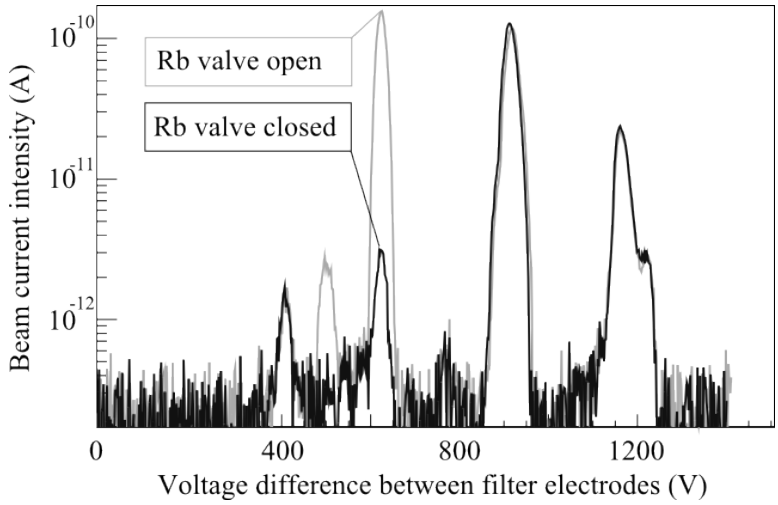

Figure 3. Mass spectra of the ion beam analyzed using the Wien filter[4]. In this measurement, the acceleration voltage of the beam was 3000 V and the current of the magnetic coils was fixed at 40 A corresponding to 1200 Gauss.

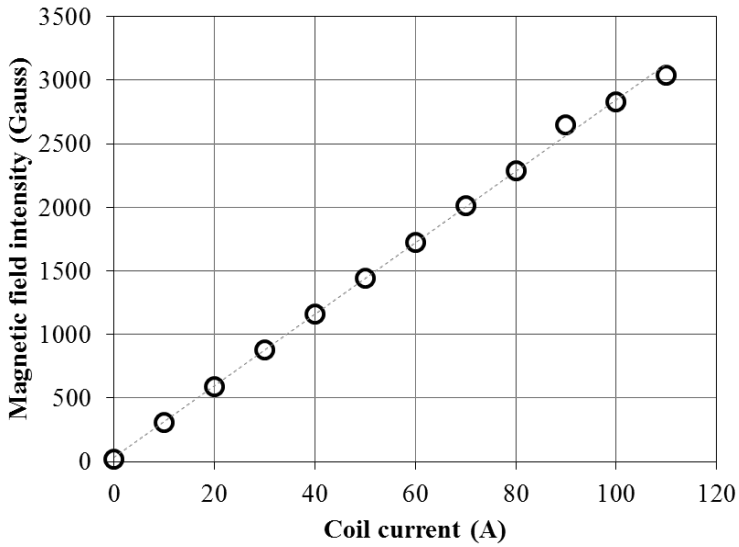

Figure 4. Coil current vs. magnetic field intensity of the Wien filter[3].

II. 2. Present Status of the Development of an Optical Dipole Force Trap System towards the Electron Electric Dipole Moment Search

Harada K.[1], Hayamizu T.[1], Kato K.[1], Sakamoto K.[1], Kawamura H.[1,2], Inoue T.[1,2], Arikawa H.[1], Ishikawa T.[1], Aoki T.[1], Uchiyama A.[1], Ito S.[1], Ando S.[1], Itoh M.[1], Aoki T.[3], Hatakeyama A.[4], Dammalapati U.[1], and Sakemi Y.[1]

[1]Cyclotron and Radioisotope Center, Tohoku University
[2]Frontier Research Institute for Interdisciplinary Sciences, Tohoku University
[3]Graduate School of Arts and Sciences, University of Tokyo
[4]Department of Applied Physics, Tokyo University of Agriculture and Technology

The permanent electric dipole moment (EDM) search experiments for the test of violation of fundamental symmetries using various kinds of atoms and molecules have been vigorously carried out in recent decades. The finite value of an EDM signal provides signature of parity (P) and time reversal (T) violations, which are explicit evidences for a new physics beyond the standard model of particle physics[1)]. The several ingenious experiments for obtaining sufficient sensitivity to detect the EDM are attempted in the world as these signals are extremely small. The signal enhancement calculated in several theories is emphasized by total number of protons (Z) in an atom and the effective internal electric field in a polar molecule and is approximately proportional to Z^3. Hence heavy atoms for EDM search have been widely employed.

The electron EDM measurement using thorium monoxide (ThO) molecule[2)] is well known as the most precise measurement. The upper limit of the electron EDM obtained from the experiment is 8.7×10^{-29} $e$cm. However, in the atomic or molecular beam experiment the significant systematic effects are caused by the motional-magnetic field $v \times E / c^2$ effect that comes from the atoms moving with velocity v through an applied electric field E (c: speed of light) and by the geometric phase shifts generated by complicated field gradients. These systematic errors mimic the true EDM signal and limit the accuracy of measurement of the EDM.

The measurements using laser cooling and trapping techniques for atoms are proposed to achieve more sensitive detection beyond the current upper limit. The velocity of the laser cooled atom is low, and therefore the interaction time between an atom and an

electric field is elongated by approximately three orders of magnitude compared to the conventional beam experiments. Moreover, the significant systematic effects caused by the motional-magnetic field and by the geometric phase shifts are strongly suppressed. Thus, there are several advantages of using optically trapped atoms for these measurements. Additionally, Francium (Fr) being the heaviest alkali atom has a large enhancement factor of about 900[3,4]. The EDM experiment using laser cooled Fr atoms promises to reach sensitivities even with their upper bounds, thus better than that of beam experiments.

We report the current status of the development of an optical dipole force trap (ODT) system for trapping Fr and rubidium (Rb) atoms at Cyclotron and Radioisotope Center (CYRIC), Tohoku University. As Rb atom has similar chemical properties to that of Fr, we mainly employed Rb atoms for the development of the ODT system. The ODT is a versatile technique for trapping neutral atoms into regions of high electric field strength and is useful for the EDM measurement. A Magneto-optical trap (MOT) is widely used as a pre-cooling method before the atoms are loaded into the ODT. The details of development of the MOT system for Rb atoms was previously reported[5,6]. The number of atoms trapped in the magneto-optical trap (MOT) chamber was about 10^8. The size of the atomic cloud was approximately 3 mm. The temperature of the atoms estimated by time-of-flight method was 90 μK. We have already achieved optical dipole force trapping of rubidium atoms. However, the loading efficiency from MOT to ODT was about 0.01%. To overcome this issue, we use polarization gradient cooling method to lower the temperature and a compressed MOT technique to increase the density of atomic cloud, and employ a high-power fiber laser of 50 W for ODT.

We introduced a new light source for optical dipole force trapping of atoms. The light source consists of a seed light and a fiber amplifier. The wavelength of the light was 1064 nm. The experimental setup is shown in Fig.1. Figure 2 shows the output power from seed light source as a function of input current. The maximum power was 550 mW at a current of 1.35 A. The power was measured by a power meter which was set in front of an isolator as shown in Fig 1. After passing through a half waveplate (λ/2) and a polarizing beam splitter (PBS) to optimize the intensity and polarization of the seed light, the light was input into the fiber amplifier. The amplifier is a continuous wave, narrow-linewidth, polarization maintaining fiber amplifier and amplifies a single-frequency light more than 50 W. The power of the seed light required as an input to the fiber amplifier is minimum 50 mW and a maximum of 200 mW, respectively. The output power of about 56 W from the amplifier

measured by a power meter was confirmed when the seed light power was 120 mW.

This research was supported by a Grant-in-Aid for Scientific Research (JP21104005, JP26220705), the Murata Science Foundation and SEI Group CSR Foundation.

References

1) Pospelov M, Ritz A, *Ann Phys* **318** (2005) 119.
2) The ACME Collaboration, Baron J *et al.*, *Science* **343** (2014) 269.
3) Mukherjee D, et al., *Phys Chem* A **113** (2009) 12549.
4) Roberts BM, et al., *Phys Rev A* **88** (2013) 042507.
5) Harada K, et al., *JPS Conf Proc* **6** (2015) 030128.
6) Hayamizu T, et al., *JPS Conf Proc* **1** (2014) 013065.

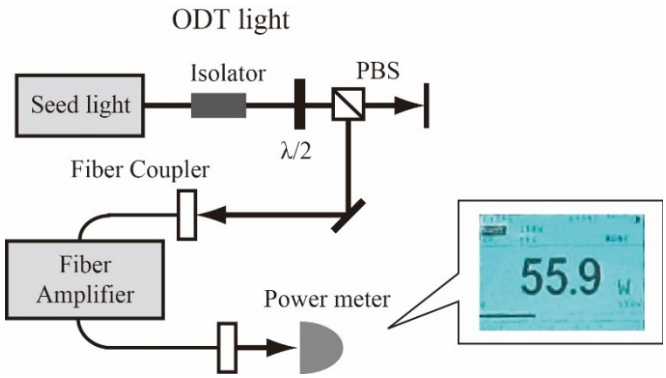

Figure 1. Experimental setup for ODT light. The picture in figure is a display of the output power of 55.9 W obtained from the fiber amplifier.

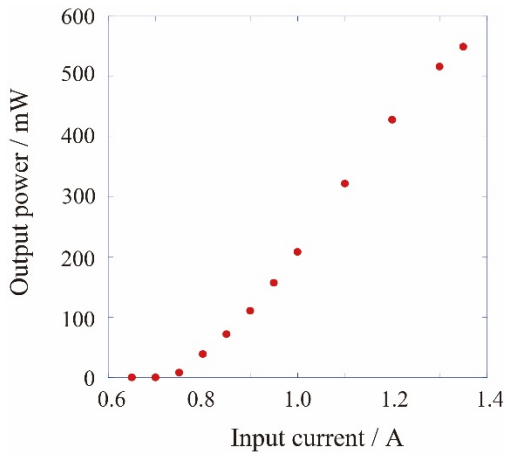

Figure 2. The output power of the seed light as a function of an input current. The threshold current was approximately 0.7 A.

II. 3. Development of an Electric Field Application System toward the Electron EDM Search Experiment

Inoue T.[1,2], Ando S.[2], Aoki T.[2], Arikawa H.[2], Dammalapati U.[2], Harada K.[2], Hayamizu H.[2], Ito S.[2], Itoh M.[2], Kato K.[2], Kawamura H.[1,2], Uchiyama A.[2], and Sakemi Y.[2]

[1]*Frontier Research Institute for Interdisciplinary Science, Tohoku University*
[2]*Cyclotron and Radioisotope Center, Tohoku University*

A permanent electric dipole moment (EDM) of a particle, an atom or a molecule plays an important role in testing the new physics beyond the standard model (SM) of elementary particles, since the EDM is sensitive to CP-violation in the theories beyond the SM[1)]. So far, a finite value of the EDM has not been observed[2)]. We plan to search for an electron EDM by using laser cooled francium (Fr) atoms. Since Fr is the heaviest alkali atom, the enhancement factor of the electron EDM is largest in alkali atoms[3)]. The laser cooling technique can localize atoms. The localized atoms would then have a long coherence time, and hence be able to suppress a statistical error and some systematic errors because of the velocity of the atom, such as a motional magnetic field[4)]. From these features, we have chosen the laser cooled Fr atoms as a substance in which the EDM is searched for.

Experimentally, the EDM is deduced from a change of spin precession frequency induced by the reversal of an electric field applied along a magnetic field. Since the magnitude of the frequency change is proportional to the electric field, the application of the strong electric field is a key issue for the EDM experiment. Our planned experiment will utilize Fr atoms trapped in a three-dimensional optical lattice. In order to realize the three-dimensional optical lattice, three-dimensional optical access is required. We employed disk-shaped glass plates coated with indium tin oxide (ITO) as transparent electrodes. The size of the glass plates was 4 cm and 1 cm thick. The transmittance of electrode was measured to be about 85% at a wavelength of 780 nm. The surface resistance of ITO was about 20 Ω/cm^2. This finite resistance of ITO, which can suppress the stray magnetic field induced from a Jonson noise current, is of advantage to the EDM experiment[5)].

We constructed the electric application system using the ITO electrodes as shown in

Fig. 1. The distance between the electrodes was fixed to be 1 cm with insulators made of ceramic. A calculated gradient of electric field was less than 1 V/mm^2 at the center between electrodes. The electrodes were installed inside a chamber with a vacuum pressure of 10^{-8} Pa. A leakage current across the electrodes was measured with a Pico ammeter which was protected from sudden discharge by inserting a low-pass filter. When positive voltage was applied, we applied the voltage up to 43 kV without discharge. On the other hand, when negative voltage was applied, we observed a sudden increase in leakage current at the voltage of -18 kV as shown in Fig. 2, and the breakdown occurred at a voltage of -20 kV. We are now investigating the difference between the positive and negative voltage applications.

In order to confirm the field strength of the electric field applied to the laser-cooled atom, we measured a DC Stark shift of a rubidium (Rb) atom trapped in a magneto-optical trap (MOT). The DC Stark shift of ^{87}Rb D1 line $\Delta\nu$ is $\Delta\nu = \alpha E^2/2h$, where α = 0.122306(16) Hz/(V/cm^2)[6] is the D1 scalar polarizability of the ^{87}Rb atom, E is the strength of the electric field and h is the Plank constant. Since α is well known, the strength of the electric field is deduced from the DC Stark shift. The ^{87}Rb atoms were trapped in the center between the electrodes. When voltage of 20 kV was applied, the observed DC Stark shift was 26(10) MHz, which corresponded to the strength of the electric field of 21(4) kV/cm. The result showed that the proper electric field was applied to the Rb atoms trapped in MOT, since the distance between the electrodes was 1 cm.

After the improvement of the negative voltage application, we will try the pilot Rb atomic EDM experiment by using the electric field application system.

This work is supported by MEXT/JSPS KAKENHI Grant Number 26220705.

References

1) Engel J, Ramsey-Musolf MJ, van Kolck U, *Prog Part Nucl Phys* **71** (2013) 21.
2) Jungmann K, *Ann Phys* **525** (2013) 550.
3) Mukherjee D, Sahoo BK, Nataraj HS, Das BP, *J Phys Chem A* **113** (2009) 12549.
4) Chin C, Leiber V, Vuletic V, Kerman AJ, Chu S, *Phys Rev A* **63** (2001) 033401.
5) Munger Jr CT, *Phys Rev A* 72 (2005) 012506.
6) Miller KE, Krause Jr D, Hunter LR, *Phys Rev A* **49** (1994) 5128.

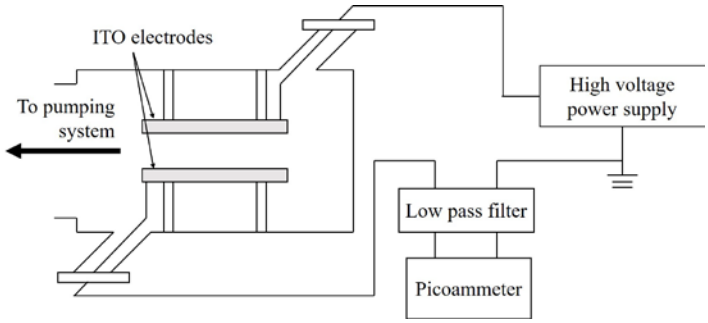

Figure 1. Schematic view of the constricted electric field application system.

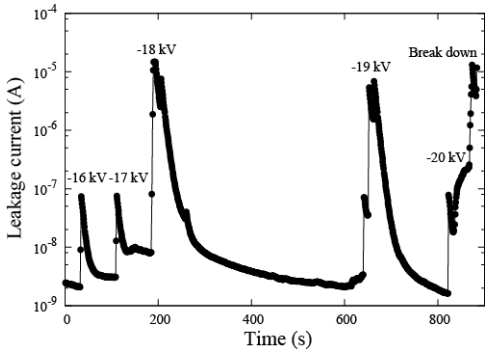

Figure 2. Leakage current with negative voltage application.

II. 4. Development of the $^{28}Si^{9+}$ Ion Beam toward the Search for Alpha Cluster Gas State in ^{28}Si

Okamoto J., Itoh M., Hayamizu T., and Nasu Y.

Cyclotron and Radioisotope Center, Tohoku University

Introduction

The alpha cluster gas state plays an important role to understand the structure of the *4N* light nucleus with equal numbers of protons and neutrons. The study for alpha cluster gas states originates from the discovery of the Hoyle state in ^{12}C[1]. This state can be explained with not the shell model but the cluster model. In the alpha cluster model, three alpha particles are loosely bound like a gas in the Hoyle state[2,3]. The search for such a gas state in *4N* nuclei has been performed up to ^{24}Mg[4].

As a next step, we are planning to search for the state in ^{28}Si, which is the next heavy *4N* nucleus of ^{24}Mg. The experiment will be performed with a 280 MeV $^{28}Si^{9+}$ beam, which has not been accelerated in CYRIC. The required beam current of $^{28}Si^{9+}$ accelerated by the AVF cyclotron is 1 eμA. Therefore, we need to supply the $^{28}Si^{9+}$ beam of 10 eμA from the ion source, since the efficiency of acceleration is 10%. In this paper, we report the test experiment for the extraction of the $^{28}Si^{9+}$ beam from the electron cyclotron resonance (ECR) ion source using a quartz (SiO_2).

Experimental method

As an ion source, we use ECR10[5]. The quartz was directly inserted in the plasma with the solid sample insertion device, as shown in Fig. 1. The extracted $^{28}Si^{9+}$ beam was analyzed by the dipole magnet and collected in the Faraday cup, as shown in Fig. 2. In order to obtain more than 10 eμA stably, we have optimized the following parameters.

1. Support gas[6] (He, O_2, and Ar)
2. Flow rate of each gas
3. Insertion speed of the quartz rod

The first two parameters and the last parameter are related to the beam intensity and the stability, respectively.

Experimental result

First, we studied the effect of the support gases. Figure 3 shows the obtained maximum beam current with each support gas. Among them, a drastic increase of the beam current was obsereved for O_2.

Second, we searched the optimum flow rate of O_2. Figure 4 shows the beam current as a function of the flow rate. The optimum flow rate of O_2 was 0.0220 cc/min (1 atm, 0 ℃). The maximum beam current was 26 eμA. By using O_2 gas and optimum flow rate, we could obtain the sufficient beam current.

Third, we studied the insertion speed of the quartz rod. By changing the speed, the appropriate speed was found to be 4.58×10^{-4} cm/min to supply the stable beam. When the quartz rod was fixed, the beam current gradually decreased as shown in Fig. 5. On the other hand, when the insertion speed of the quartz rod was 10 times faster than the appropriate speed, the beam current suddenly disappeared, as shown in Fig. 6. We found the plasma state was very sensitive to the insertion speed.

Summary

We succeeded in extracting the $^{28}Si^{9+}$ beam from the ECR ion source at CYRIC. By optimizing the support gas and the insertion speed, we could supply the sufficient beam current stably. Finally, we also succeeded in accelerating the $^{28}Si^{9+}$ ion up to 280 MeV with the 930 AVF cyclotron. This was the first time at CYRIC to accelerate the beam extracted from a solid sample. The test experiment of the search for the alpha cluster gas state in $^{28}Si^{9+}$ is scheduled for July 2016.

References

1) Cook CW, Fowler WA, et al., *Phys Rev* **107** (1957) 508.
2) Kamimura M, *Nucl Phys* **A35**1 (1981) 456.
3) Uegaki E, Okabe S, Abe Y, Tanake H, *Prog Theor Phys* **57** (1977) 1262.
4) Kawata T, et al., *J Phys Conf Ser* **436** (2013) 012009.
5) Wakui T, et al., *CYRIC Annual Report 2010-2011*.
6) Tarvainen O, "Studies of electron cyclotron resonance ion source plasma physics".

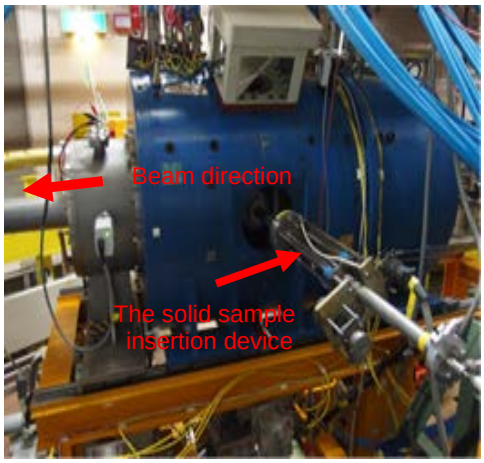

Figure 1. Picture of ECR10.

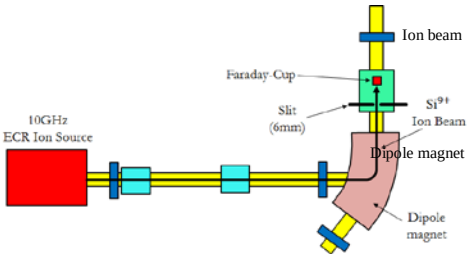

Figure 2. Schematic view around ECR10.

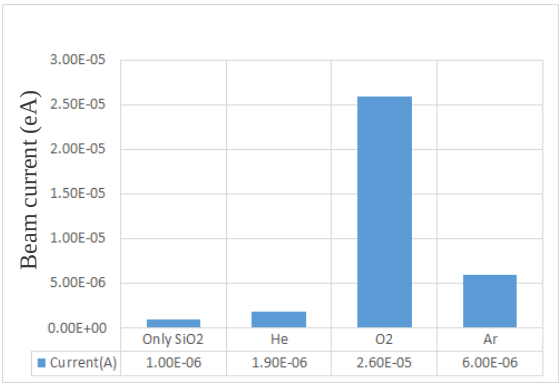

Figure 3. Maximum beam current of $^{28}Si^{9+}$ for each support gas.

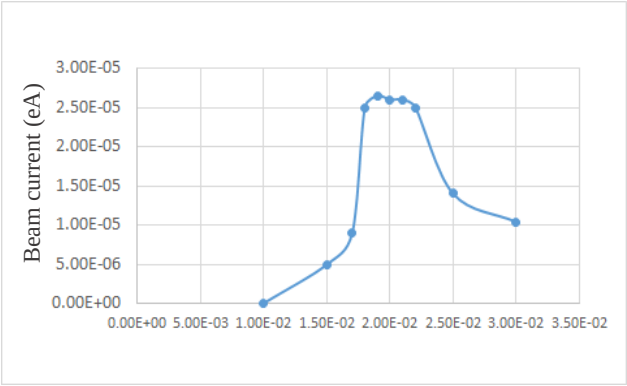

Figure 4. Beam current of $^{28}Si^{9+}$ for O_2 gas.

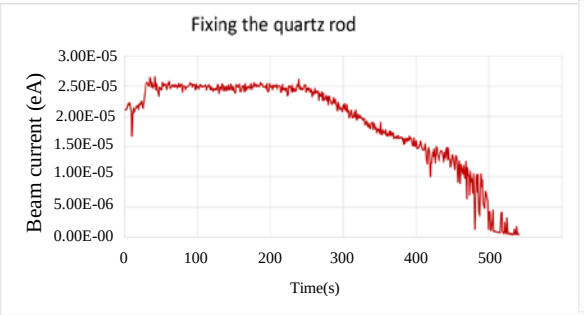

Figure 5. Change of the beam current of $^{28}Si^{9+}$ when the quartz rod is fixed.

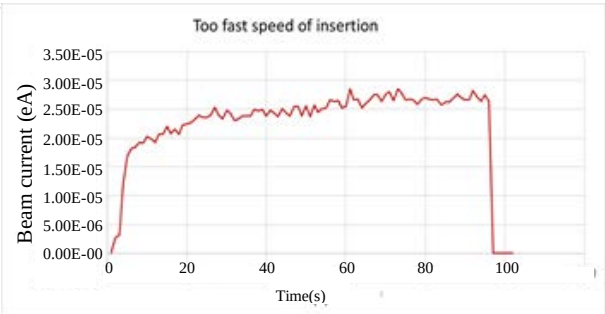

Figure 6. Change of the beam current when the current speed is 2.90×10^{-3} cm/min.

III. NUCLEAR MEDICAL ENGINEERING

III. 1. Development of a Multi-channel Charge-readout System for a Micro-pattern Gaseous Detector

Terakawa A.[1], Ishii K.[1], Matsuyama S.[1], Sato T.[1], Inano K.[1], Sakemi Y.[2], and Fujiwara T.[3]

[1]Department of Quantum Science and Energy Engineering, Tohoku University
[2]Center for Nuclear Science, The University of Tokyo
[3]Graduate School of Engineering, The University of Tokyo

High-precision beam monitoring has been needed to measure beam profiles during beam scanning irradiation in charged-particle cancer therapy. Compared to conventional beam monitors using multiwire proportional counters, micro-pattern gaseous detector (MPGD) technology[1)] has shown several advantages such as the excellent special resolution and stable operation at higher counting rates. We developed a prototype beam monitor of a MPGD design with gas electron multiplier (GEM), and successfully measured the two-dimensional intensity distribution and relative dose of a proton beam using it[2)]. Since the prototype detector was built using a small size of the GEM foil (3×3 mm^2) and a charge-readout board with only 16 channels, it can be used in a limited way as a beam monitor for charged-particle therapy. Thus, we have developed a new MPGD beam monitor with a 10×10 mm^2 GEM and a 256-channels read-out board to apply it to beam monitoring in charged-particle therapy. In this report we described the new beam monitor and the results of beam irradiation experiments.

Figure 1 shows the MPGD beam monitor which contains a cathode plate (Al foil 12.5 μm thick), a Glass-GEM and the read-out board in the monitor chamber. Mylar foil 12 μm thick and Al foil 1 μm thick foil were used as beam entrance and exit windows of the chamber. Ne-CF_4 mixed gas (Ne:CF_4 = 9:1) was flowed at the flow rate of 100 cc/min in the MPGD chamber. The read-out board collects the induced charge of the secondary electrons with vertical and horizontal strips. The number of the strip was 126 in each direction while the strip gap was 1 mm.

We developed a multi-channel charge-readout system by designing and developing a charge-to-time converter module (QTM) for the MPGD system. The QTM developed in this

work was based on an ASIC unit, CLC101EF manufactured by IWATSU Co. Ltd. The CLC101EF has 9 channels for readout, and provides a pulse signal whose duration is proportional to the amount of input charge. We have designed the QTM so that the CLC101EF is easily controlled and connected to the MPGD using a personal computer. Because two CLC101EFs are used in the QTM, it is possible to acquire and process the charge signals up to 18 channels using the single QTM.

To process the output of MPGD in the QTM, a characteristic test was performed using the test charge. The QTM has various parameters for changing the relationship between the amount of input charge and the duration of the output signal. In order to provide appropriate charge of the secondary electrons (approximately 2.5 pC / incident proton) to the readout board leading to the QTM, we applied 800 V/cm between the cathode plate and the GEM, and 715 V between the GEM electrodes. The results of the tests showed that the duration of 1ns approximately corresponded to the collected charge of 80 fC.

Proton irradiation experiments were performed using an 80-MeV proton beam at the beam intensity of 7 nA to measure the two-dimensional beam profile and dose information by processing the output signals from the MPGD using the QTM. The experimental setup is show in Fig. 2. The intensity distribution of the proton beam measured with MPGD combined with QTM is shown in Fig. 3. The results for the MPGD are compared to that for an imaging plate (IP) manufactured by Fuji film Co. Ltd. The two-dimensional distributions measured using the MPGD are in good agreement with that of IP. In addition, we have observed the linear relationship between the integrated charge outputs of the MPGD and irradiation time (Fig. 3). Since the beam intensity was kept constant during this measurement, the result indicate that the MPGD can be used as a dose monitor as well.

In conclusion, it was confirmed that the QTM developed in this work was capable of processing the charge-output signals of the MPGD. We have successfully evaluated not only the intensity distribution but also dose information of the proton beam using the MPGD combined with the QTM.

References

1) Sauli F, *Nucl Instrm Meth* A **386** (1997) 531.
2) Terakawa A, et al., *Nucl Instrm Meth B* **365** (2015) 606.

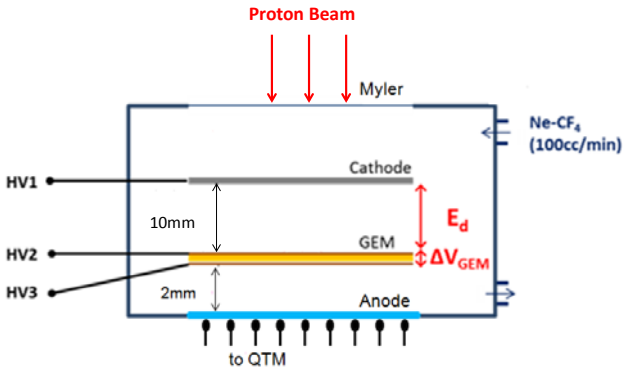

Figure 1. Schematic view of the MPGD beam monitor for proton therapy.

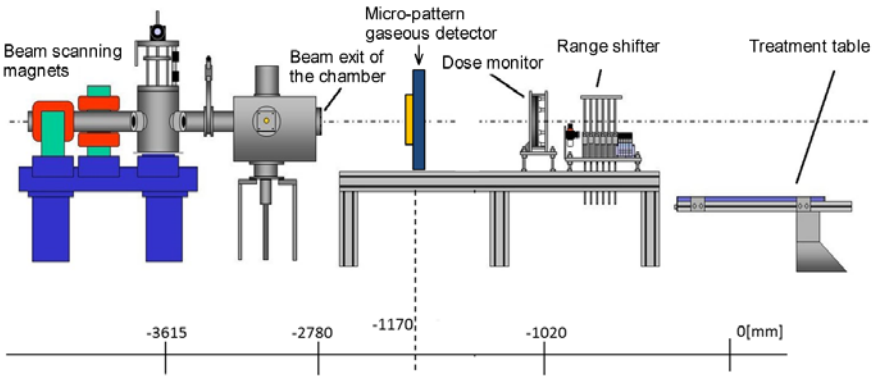

Figure 2. Experimental setup for the beam test of the MPGD beam monitor.

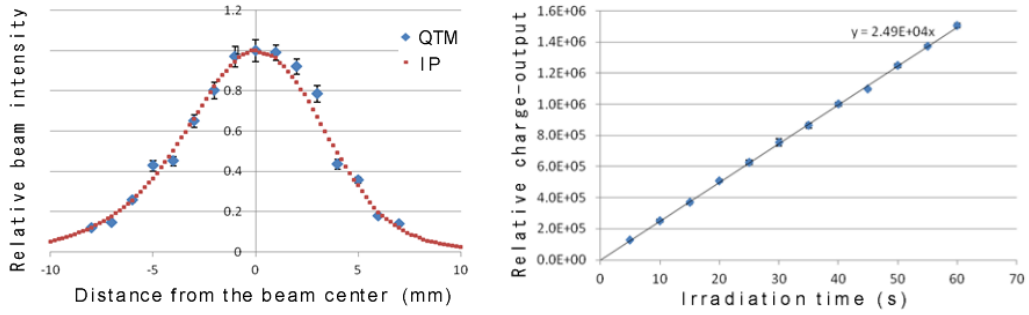

Figure 3. The lateral beam-intensity distribution (left) and the linear relationship between the integrated charge from the MPGD and irradiation time. The beam intensity was kept constant during the measurement.

III. 2. Three-dimensional Imaging of Human Cells by Using PIXE-μ-CT

Matsuyama S.[1], Ishii K.[1], Toyama S.[1], Watanabe K.[1], Koshio S.[1], Kasahara K.[1], Ito S.[1], Terakawa A.[1], Fujiwara M.[1], Ortega R.[2], Carmona A.[2], and Roudeau S.[2]

[1]Department of Quantum Science and Energy Engineering, Tohoku University
[2]CNAB, CNRS Universite Bordeaux 1, France

1. Introduction

Short-term exposure to particulate matter (PM) can adversely affect human health and numerous studies have been carried out. The main route of exposure is via the respiratory tract by inhalation of dusts, fumes and mists. Human tissues and fluids normally contain low levels of trace elements as essential element, but abundance of elements in tissues is increased as a result of environmental or occupational exposures and is highly toxic. Some studies were carried out to know the interaction between these particles and human body at a cellular level by using the micro-PIXE/RBS and synchrotron X-ray fluorescence microprobe[1-3]. While the mechanism was suggested in these studies, distribution of particles in the cell is still uncertain because 2D imaging only gives a projection image of the distribution. The 3D distribution of the particles in the cell will give us crucial information on the suggested intracellular interaction mechanism between the particles and human cells. Only few imaging techniques exist that allow *in-situ* quantification and distribution of the particles in cell[4]. We developed a three-dimensional (3D) computed tomography (CT) imaging system for imaging to observe the interior of small samples with a spatial resolution of a few μm. The imaging system, referred to as PIXEμCT, uses particle-induced X-ray emission (PIXE) produced by proton beam bombardment of a metal target. The 3D PIXEμCT has a capability to measure intercellular distribution of the particles and is one of the most powerful tools. In the previous study, our system was optimized to observe the cell interior[5]. While strong absorption of X-ray was observed in the cell, it is difficult to know where the chromium particles are distributed. Since X-ray absorption in the cell was too low to distinguish between cell and the part where chromium concentration was low. In this study, we applied the dual-energy

subtraction imaging method[6-8] to the 3D PIXEμCT for cell elemental imaging. The dual-energy subtraction method is one of the tools which enhance the contrast of the specific elements. The method is based on the sharp change of attenuation coefficient at K-absorption edge of contrast media, which is applied to the X-ray radiography in a human angiography by adding iodinated contrast media. The method uses two different energy X-rays of higher and lower energies of K-absorption edge and subtract image obtained by the high energy from the one by the lower energy. Thus the subtract image shows enhanced image of iodine[6,7]. In this study, we analyzed human epithelial cells exposed *in vitro* to cobalt oxide. Short-term exposure of cobalt oxide affects human cell and health. The energy of absorption edge of cobalt is 7.71 keV, we choose Sc, Ni and Cu targets, whose characteristic X-ray energy are 4.1, 7.47 and 8.04 keV, respectively. By changing the X-ray energy, we obtained projection data and reconstructed 3D images corresponding to the X-ray energy.

2. PIXE-micron-CT system

The PIXEμCT consists of an accelerator, a proton microbeam system, and a target chamber system with X-ray CCD camera[9-15]. In the PIXEμCT configuration, the X-ray point source and the X-ray CCD are fixed while the sample is placed in between and it is rotated. In this system, 2D X-ray projection data are obtained for each rotation angle of the sample and 3D image can be reconstructed. The most unique feature of this system is to use PIXE method for the generation principle of X-rays. Conventional CT system (medical CT, industrial CT) uses the irradiation of the electron beam to metallic target such as tungsten and generates polychromatic X-ray of bremsstrahlung. In that case, energy range is too wide and too high for intercellular imaging. On the other hand, PIXEμCT uses the irradiation of proton which is about 1800 times heavier than electron. Therefore, X-ray generated with this system consists mainly of characteristic X-ray of target element and is quasi-monoenergetic[16]. These properties allow to get high-contrast imaging of cells and are suitable for this biological samples analysis as exemplified in insect studies.

3. Experiment

3.1. Selection of Target

Since the PIXEμCT can easily change the X-ray energy by changing the X-ray target, the dual-energy subtraction method is suitable for elemental imaging in the system.

Since cells were exposed by cobalt oxide, we choose characteristic X-rays of Sc, Ni and Cu. Since X-ray energy from Sc target is 4.09 keV, strong absorption will be observed for both cell and cobalt oxide particles. Absorption in the cell and cobalt oxide will be minimum for Ni target. Absorption of cobalt will be highest for Cu target. X-ray target was set at 30 degrees with respect to the beam. A thick target was bombarded with a focused 3 MeV proton microbeam of 1.3 × 1.6 μm^2 and a beam current of 900 pA. The geometric magnification was 6.9 for these target. For these parameter spatial resolution is estimated to be less than 5 μm. The measurement time was around 3 hours for each X-ray target. Two-dimensional (2D) transmission data were obtained with the cone beam and sample rotation. A full 3D image was reconstructed from the image data in the vertical plane, using filtered back projection (FBP)[17,18].

3.2. Sample preparation

Sample fixation on the rotating shaft of the PIXEμCT. A micro polycarbonate tube (Hagitec Co. Ltd., PIT-FS(0.08); inner diameter of 80 μm and tube thickness of 13 μm) was used to fix the cells which was adapted from a previous study on lead chromate particles[19]. The tube will be the smallest and thinnest commercially available. Since size of the cell is in the order of 10 to 20 μm, tube thickness is almost same order and not deteriorates the contrast. Furthermore, composition of the tube is similar to that of cells, it will be useful to calibrate the PIXEμCT.

Human epithelial cells exposed *in vitro* to cobalt oxide micro-particles solution, of 400 nm mean size, at 10 μg/mL concentration during 24 h. Cryogenic methods were adopted to fix the cell in the tube, since they consist of immobilizing the intracellular components by cryofixation and later extraction of the water by freeze drying process. The protocol is almost the same as that for SXRF and PIXE analysis[3], except for encapsulate process. Capillary action was used to insert the cell into the tube. After that, the tube was sealed with formvar and cryofixed at -165°C into isopentane chilled with liquid nitrogen. Then the sample was freeze dried at -35°C for 1 week after removing the seal. By this procedure, the cells were fixed in the inner wall of the tube. Then the end of the tube is inserted into the injection needle, and then fixed to rotation shaft by using a pin vice.

4. Results and Discussion

Figure 1 shows maximum intensity projection (MIP) images of human epithelial

cells measured by proton bombardment of Sc, Ni and Cu targets. The MIP image displays only the voxels with maximum intensity along a line from the viewer's eye through the volume of data[20]. Cross sectional images for indicated position are also shown. Strong absorption regions are clearly seen for these figures. Since the size of the cells is around 20 μm, it can be shown that cells incorporated the cobalt oxide intracellularly from this image. Although the micro tube made by polyimide is clearly seen for Sc target, it is not so clear for Ni and Cu targets due to increases of transmission probability. On the other hand, cells are clearly recognized in these images. Cellular chemical composition and density is similar to that of the polycarbonate micro tube and their X-ray absorption is similar. Therefore, the image for Sc target indicates the absorption both for cell and for chromium oxide. Strong absorption for Ni target indicates the presence of Co oxide in the cells. Figure 2 shows the cross-sectional views of the cells indicated in Fig. 1. Although the absorption of the images for tube reduces as X-ray energy, those of cell is not changed so much due to the strong absorption of Co oxide.

Figure 3 shows the line profiles of the cells indicated in Fig. 2. In the CT image, the pixel values correspond to the linear attenuation coefficient (μ) and indicated in CT value in figure 3. As shown Figs. 1 and 2, tube is evident in the line profiles for Sc K X-rays. The peaks in the line profiles for the Sc X-rays are widest, which indicate that the cell absorbed Co oxide in the center of the cell. The ratio of CT value is proportional to that of μ for materials. CT values of the tube are around 7000. CT values of the cell for Sc X-rays are around 25,000-30,000 and higher that for Ni and Cu X-rays. CT values of the cell for Ni target are lower than those for other X-rays, which is expected from μ value of Co. The ratios CT values of the cells for Sc, Ni and Cu X-rays are 1:0.49:0.71, 1:0.79:0.94 and 1:0.3:0.41 for cell 1, 2 and 3, respectively. Because the ratios of μ of Co for Sc, Ni and Cu X-rays are 1:0.18:0.14, respectively, the enhancement due to absorption edges of Co is not so strong in the cell. Since main composition of the cell is O, C, H and N, which are not have absorption edges in this energy region, the enhancement due to the absorption edges of Co is subdued. These results also indicate that the absorption of Co oxide is depend on the cell.

5. Conclusion

In this study, we imaged the human epithelial cells exposed of chromium oxide

micro particles by using the 3D PIXEμCT. The use of energy selectable quasi-monochromatic low-energy X-rays by proton microbeam bombardment in the PIXEμCT improved the image quality by taking advantage of the absorption edge of the elements compared with conventional X-ray CT that uses bremsstrahlung X-rays produced by an X-ray tube. The imaging capabilities were enhanced by using the absorption edge of the elements. The cells absorbed Co oxide in the center of the cell. The ratios CT values of the cells shows that the strong absorption stems from Co oxide. This information is complementary to 2D micro-PIXE analysis which only gives a projection image of the elemental distribution.

Acknowledgements

This study was supported in part by a Grant-in-Aid for Challenging Exploratory Research grant (Grant No. 26630477) from the Japan Society for the Promotion of Science (JSPS). This study was partly supported by a Grant-in-Aid for Challenging Exploratory Research Grant No. 23656583, Japan Society for the Promotion of Science (JSPS). This study was also supported Japan-France Integrated Action Program (SAKURA).

The authors would like to acknowledge the assistance of M. Fujisawa and T. Nagaya for maintenance and operation of the Dynamitron accelerator.

References

1) Ortega R, Devès G, Fayard B, Salomé M, Susini J, *Nucl Instrum Meth B* **210** (2003) 325.
2) Ortega R, Fayard B, Salomé M, Devès G, Susini J, *J Physiq IV* **104** (2003) 289.
3) Ortega, R, Fayard B, Salomé M, Devès G, Susini J, *Chem Res Toxicol* **18** (2005) 1512.
4) Sarkar B, (Ortega R Ed.), *Marcel Dekker Inc*., New York, 2002 pp.35-68.
5) Kawamura Y, Ishii K, Matsuyama S, et al., *Int J PIXE* **19** (2009) 29.
6) Oguri Y, Hasegawa J, Ogawa M, *Proceed 23rd PIXE Symp*.
7) Umetani K, Ueki H, Ueda K, et al., *J Synchrotron Rad* **3** (1996) 136.
8) Rubenstein E, Hughes EB, L. Campbell E, et al., *SPIE* **314** (1981) 42.
9) Ishii K, Matsuyama S, Yamazaki H, et al., *Int J PIXE* **15** (2005) 111.
10) Ishii K, Matsuyama S, Yamazaki H, et al. *Int J PIXE* **15** (2005) 195.
11) Yamaguchi T, Ishii K, Yamazaki H, et al., *Int J PIX*E **15** (2005) 111.
12) Ishii K, Matsuyama S, Yamazaki H, Y. et al., *Nucl Instrum Meth B* **249** (2006) 726.
13) Ishii K, Matsuyama S, Watanabe Y, et al., *Nucl Instrum Meth A* **571** (2007) 64.
14) Kawamura Y, Ishii K, Yamazaki H, et al., *Int J PIXE* **17** (2007) 41.
15) Ohkura S, Ishii K, Matsuyama S, et al., *Int J PIXE* **18** (2008) 167.
16) Ishii K, Morita S, *Int J PIXE* **1** (1992) 1.
17) Yamaguchi T, Ishii K, Yamazaki H, et al., *Int J PIXE* **15** (2005) 195.
18) Paarashar V, Frankel S, G.Luriec A, Rogina B, *Radiat Res* **169** (2008) 707.
19) Kawamura Y., Ishii K., Matsuyama S., et al., *Int J PIXE*, **19** (2009) 29.
20) Wallis JW, Miller TR, Lerner CA, Kleerup EC, *IEEE Trans Med Imaging* **8** (1989) 297.

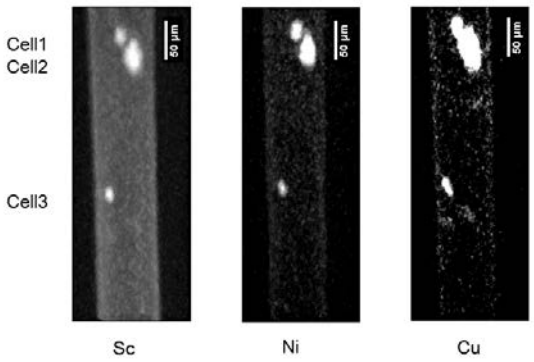

Figure 1. Maximum intensity projection (MIP) images of human epithelial cells measured by proton bombardment of Sc, Ni and Cu targets.

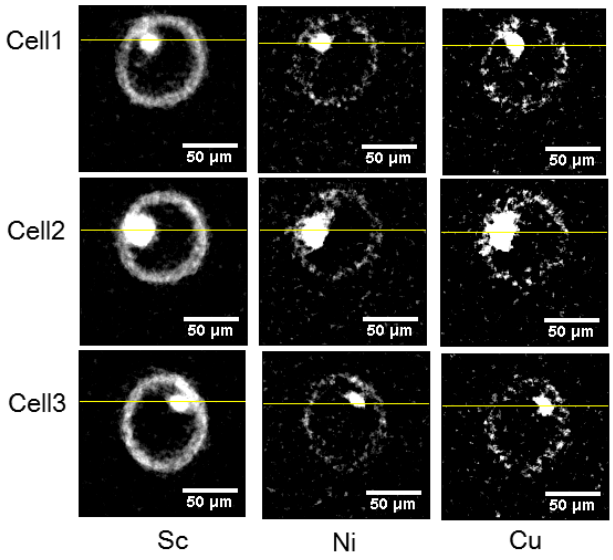

Figure 2. Cross-sectional views of the cells indicated in Fig. 1.

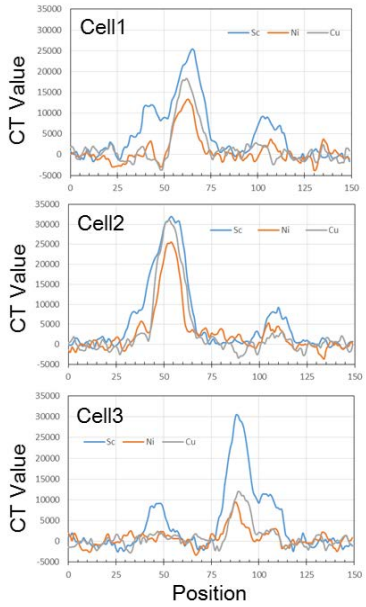

Figure 3. Line profiles of cell 1, 2 and 3.

IV. PIXE AND ENVIRONMENTAL ANALYSIS

IV. 1. Development of a High-current Microbeam System

Matsuyama S., Ishii K., Suzuki S., Terakawa A., Fujiwara M., Koshio S., Toyama S., Ito S., Fujisawa M., and Nagaya T.

Department of Quantum Science and Energy Engineering, Tohoku University

1. Introduction

Characterization of the spatial distribution of elements in a specimen is an important technique. A microbeam system was installed at a Dynamitron laboratory at Tohoku University in 2002 and has been used in several different fields[1)]. The microbeam system has been applied to simultaneous in-air/in-vacuum PIXE, RBS, SE, and STIM analyses, with applications in various fields[2-6)]. While this analysis system is applicable to simultaneous in-air/vacuum PIXE, RBS, and STIM analyses, as well as 3D μCT without changing the target chamber[7)], changes are required in the equipment setup with these techniques, which is time-consuming, and a new high-energy-resolution μ-PIXE system for chemical state mapping is planned. For this, a wavelength-dispersive X-ray (WDX) spectrometer with a high-energy resolution was developed. By combining the WDX and microbeam systems, the chemical state of elements can be mapped. Although the WDX system can be also adapted to the microbeam line without changing the target chamber, the WDX system is large, and precise adjustments are required. To meet these requirements, another microbeam line was recently developed in the Dynamitron laboratory dedicated to chemical state mapping, i.e., a von Hamos X-ray spectrometer with a charge-coupled device (CCD) camera. Although the sensitively of the WDX system was higher than that of conventional crystal spectrometers in terms of detection efficiency, larger beam currents are required in the microbeam system. In this work, we developed a high-current microbeam system dedicated to the WDX-μ-PIXE system for chemical state mapping.

2. Design of the high-current microbeam system

A microbeam system was developed for the WDX-μ-PIXE system and designed so

that the spot size of the beam was 1 × 1 μm^2 with a beam current of several hundred pA. This new microbeam system is termed MB-II to distinguish it from the existing microbeam system (i.e., MB-I, which was developed for biological applications with the aim of achieving a submicron beam size[8-11]. The energy stability of the accelerator was significantly improved to $<10^{-4}$, which is sufficient for submicron beam formation in the doublet system without requiring an analysis system[8,9,10]. MB-II was installed in the –15º beam line. This arrangement allows for a total length of the microbeam line of 7 m. The lens system of MB-II was a quadrupole doublet, and the spherical and chromatic aberration coefficients of the doublet system are smaller than those of the triplet system[8,9]. The beam properties were calculated using TRANSPORT[12] and the ray-tracing software package WinTRAX[13]. The working distance was 24 cm, and the separation from the object slit to the quadrupole doublet lens was 6.04 m. The demagnification factors were 38 in the horizontal plane and 9.5 in the vertical plane. The spot size of the beam was 1 × 1 μm^2 when the beam divergence was limited to 0.2 mrad and the object size was 40 × 10 μm^2. Figure 2 shows a diagram of the layout of MB-II; the system was composed of a quadrupole doublet lens, a micro-slit (MS), and a divergence-defining slit (DS). The total length of the line was approximately 7 m. The MS defines the object size, and the DS defines the beam divergence into the quadrupole doublet, which was located 5.22 m downstream of the MS. In MB-I, a baffle slit (BS) was used to reduce the scattered beam. These components were mounted on a heavy rigid support to provide vibration isolation, which was placed on three concrete blocks with dimensions of 70 × 70 × 70 cm^3.

3. Performance

3.1. Beam brightness

The beam brightness is of primary importance to increase the current of the focused beam. The beam brightness was characterized by measuring the target current in the microbeam with the MS fixed, while varying the DS. The MS widths were 40 × 10 μm^2, which corresponds to a beam spot size of 1 × 1 μm^2. The largest beam brightness of MB-I was 2.3 $pA \cdot \mu m^{-2} \cdot mrad^{-2} \cdot MeV^{-1}$ with a half-divergence of 0.07 mrad. Since the beam line to MB-II is short compared with that of MB-I, the beam brightness at MB-II will be larger than that at MB-I, and the beam transport conditions for MB-II will differ from those of MB-I. The terminal equipment of the Dynamitron accelerator comprises a duoplasmatron ion source along with an extractor, an Einzel lens, an ExB filter, and a gap lens[14]. The

extraction voltage and gap lens voltage significantly affects the beam brightness, which determines the lens effects. These parameter was confirmed by both calculations using OPTIC-III (National Electrostatic Corporation, NEC) and by experiments[8,11,14]. A large beam brightness of 2.4 pA·μm^{-2}·mrad^{-2}·MeV^{-1} was achieved with a half-divergence of 0.1 mrad. The beam brightness of MB-I was decreased significantly for larger divergences, which means the beam intensity was stronger in the central region. The beam brightness at MB-II, however, did not diminish as the beam divergence increased. This difference results from the different beam loss of the beam line components between the accelerator and MB-I. Due to the small spherical and chromatic aberration coefficients, the beam divergence into the quadrupole lens was 0.2 mrad in MB-II. A beam current of more than 300 pA was obtained for a beam spot size of 1 × 1 μm^2, which is larger than that of MB-I.

3.2. Beam spot size

The spot size of the beam was characterized via beam scanning across fine mesh samples (Ni meshes, with 2000 lines per inch) by measuring X-rays. The horizontal and vertical line profiles shown in Figure 3. The horizontal and vertical line profiles were fitted using symmetric double Gaussian convolution to obtain the spot sizes. The line profiles were well reproduced using symmetric double Gaussian convolution, which implies that the beam profile can be assumed to be Gaussian. A spot size of 1 × 1.5 μm^2 was obtained with an MS opening of 40 × 10 μm^2.

4. Conclusions

We developed an MB-II high-current microbeam system dedicated for chemical state mapping, which was composed of two slits and a quadrupole doublet lens mounted on a heavy rigid support. The microbeam system was not equipped with a high-resolution energy analysis system and was connected to a switching magnet. The largest beam brightness was 2.4 pA·μm^{-2}·mrad^{-2}·MeV^{-1} at a half-divergence of 0.1 mrad. A beam current greater than 300 pA was obtained for an object size of 40 × 10 mm^2 with a half divergence of 0.2 mrad. The calculated spot size of the beam was 1 × 1 μm^2, and the measured spot size was 1 × 1.5 μm^2. The WDX-μ-PIXE system is currently operational at the microbeam system.

Acknowledgments

This study was partly supported by a Grant-in-Aid for Challenging Exploratory Research Grant No. 26630477 from the Japan Society for the Promotion of Science (JSPS).

References

1 Matsuyama S, Ishii K, Yamazaki H, et al., *Nucl Instrum Meth B* **210** (2003) 59.
2. Matsuyama S, Ishii K, Yamazaki H, et al., *Int J PIXE* **18** (2008) 199.
3. Matsuyama S, Ishii K, Fujiwara M, et al., *Int J PIXE* **19** (2009) 61.
4. Matsuyama S, Ishii K, Fujiwara M, et al., *Int J PIXE* **21** (2011) 87.
5. Ishii K, Matsuyama S, Yamazaki H, et al., *Nucl Instrum Meth B* **249** (2006) 726.
6. Ishii K., Matsuyama S., Y. Y. Watanabe, et al., *Nucl Instrum Meth A* **571** (2007) 64.
7. Matsuyama S, Ishii K, Yamazaki H, et al., *Nucl Instrum Meth B* **260** (2007) 55.
8. Matsuyama S, Ishii K, Tsuboi S, et al., *Int J PIXE* **21** (2011) 87.
9. Matsuyama S, Ishii K, Watanabe K, et al., *Nucl Instrum Meth B* **318** (2014) 32.
10. Matsuyama S,. Fujisawa M, Nagaya T, et al., *Int J PIXE* **23** (2013) 69.
11. Matsuyama S, Watanabe K, Ishii K, to be published in *Int J PIXE*.
12. Brown KL, SLAC-91 (1977).
13. Grime GW, *Nucl Instrum Meth B* **306** (2013) 2060.
14. Matsuyama S, Ishii K, Fujisawa M, et al., *Nucl Instrum Meth B* **267** (2009) 2060.

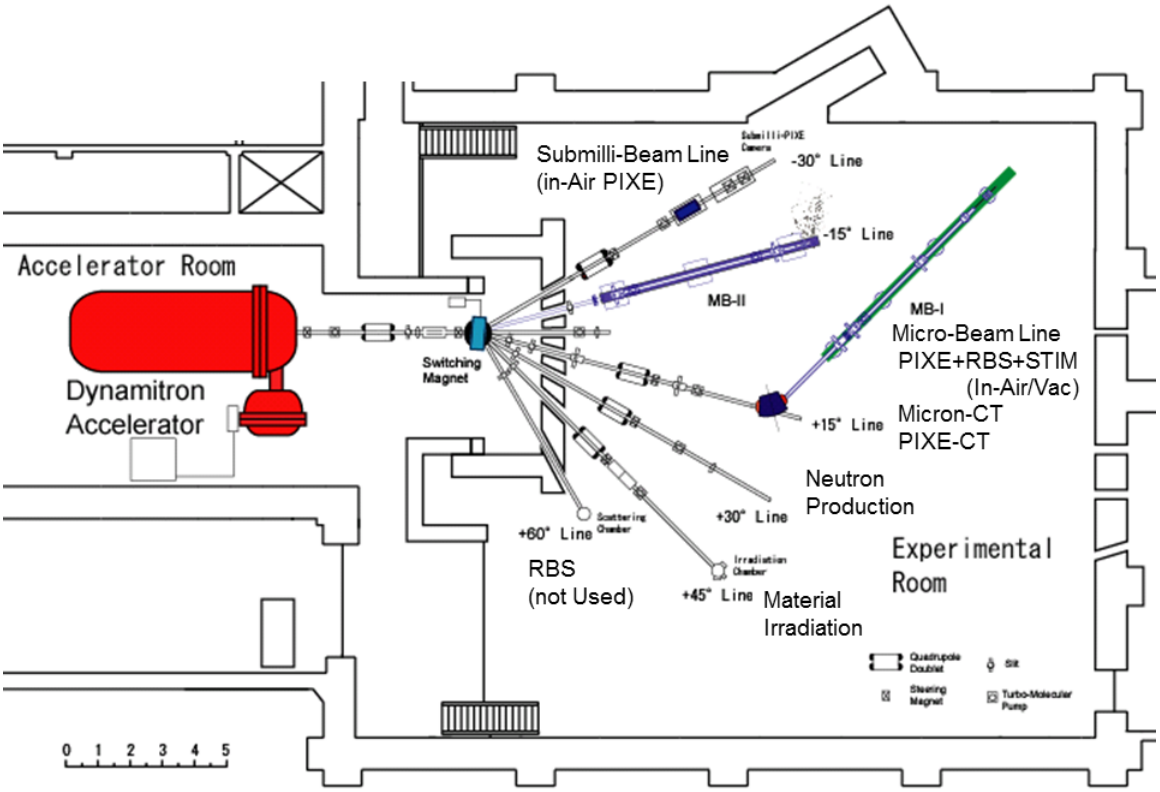

Figure 1. The layout of the Dynamitron laboratory.

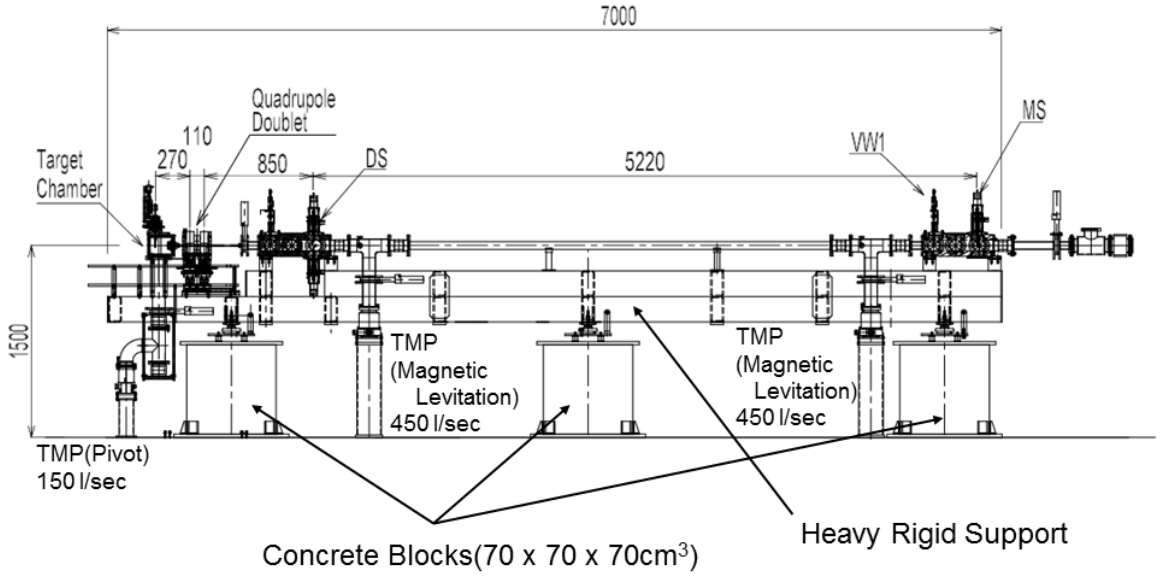

Figure 2. Scale drawing of the microbeam system.

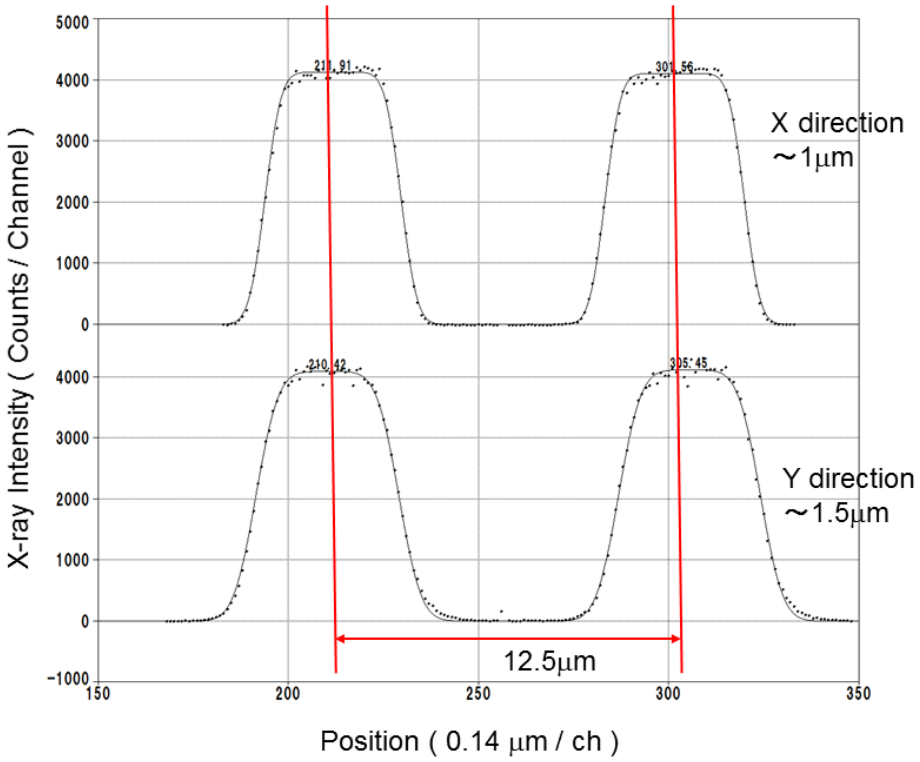

Figure 3. The horizontal and vertical X-ray line profiles of a fine Ni mesh (2000 lines/inch).

IV. 2. Development of the Terminal Voltage Stabilizating System of the Dynamitron Accelerator

Matsuyama S., Fujisawa M., and Nagaya T.

Department of Quantum Science and Energy Engineering, Tohoku University

1. Introduction

A microbeam system of Tohoku university was installed in 2002[1)]. The Tohoku microbeam system comprises a quadrupole doublet and three slit systems and is connected to the Dynamitron accelerator after energy analyzing system. After the installation, the microbeam system has been used for various applications[2-7)]. The microbeam system was upgraded into the triplet lens system for the analysis in the nano-scale region. While the triplet microbeam system has higher demagnification comparing to the previous system, higher chromatic and spherical aberration coefficient degrade the performance. In order to overcome these effects, energy resolution of the accelerator was improved by developing the terminal voltage stabilizing system (TVSS).

2. Terminal Voltage Stabilizing System of the Tohoku Dynamitron Accelerator

The high-voltage generator of a Dynamitron accelerator is a parallel-fed, series-cascaded rectifier system (Schenkel type voltage generator)[8-10)]. The high-voltage generator and the voltage stabilizing system of the Tohoku Dynamitron Accelerator was described precisely in the previous publication[9)]. The high voltage of the terminal is controlled by varying the RF voltage of the oscillator into the L-C tank circuit of the accelerator. The RF voltage is precisely controlled by a high-voltage DC power supply which is stabilized by a feedback system which consists of three loops; a fast feedback loop employing capacitors, an inner loop involving resisters and an amplifier (inner loop amplifier) and an outer loop[11,12)]. The former two loops reference the high-voltage into the oscillation tube and mainly minimize output of 50 and 300 Hz ripple due to the primary power supply and of rather fast ripple components (up to 10^{-5}～10^{-6} sec). In the outer loop, the high voltage is measured

through a resister network (high-voltage divider, HVD) and a high-precision resistor. The voltage generated on the high-precision resistor is compared with a reference voltage. The difference in the voltage is amplified by an integral amplifier and a buffer amplifier, and then the RF voltage is varied until the difference between the measured and reference voltage is eliminated. Thus, the slow fluctuations in the terminal high voltage are removed. The response time is in the order of several hundred msec. which is restricted by the discharge time of the terminal. The feedback system was designed for more than 40 years ago, and consisted of vacuum tubes. In the previous study, adjustment of the feedback gain of the loops and the reduction of the noise form the line frequency were carried out. The ripple was greatly reduced down to 70 V, but was not enough for the triplet system.

In order to reduce the voltage ripple, we redesigned the feedback system and made by using solid state devices. Figure 1 shows a schematic view of the high-voltage generator and the terminal voltage stabilizing system (TVSS). The high voltage of the terminal is measured by using a generating voltage meter (GVM) provided by National Electrostatics Corporation (NEC). The GVM signals are amplified by an amplifier (the sensitivity is Ca. 2 V/ 1MV) and is inputted into a kind of instrumentation amplifier in the TVSS. An instrumentation amplifier is a differential amplifier with two input buffer amplifiers, have characteristics of low drift, low noise and high common-mode rejection ratio and are used where accuracy and stability both short and long-term are required. The voltage signal is compared with a reference voltage (control voltage). The difference of the measured and reference voltages are introduced into a proportional-integral-derivative (PID) or a proportional-integral (PI) circuit after adjusting the gain (GVM feedback gain). Since the response time of the outer loop is in the order of several hundred msec, the PI control is enough for voltage regulation. The output voltage of the controller is ranging from 0 to 10 V, which corresponds to 0 to 5 MV. Since the previous feedback system was composed of vacuum tubes, the voltage range is 0 to -100 V. In order to match the previous system, the output voltage of the controller is further amplified to provide 0 to -100 V signal by a conventional high-voltage amplifier (PA94, Apex Microtechnology, Inc.). The inner loop amplifier was differential amplifier composed of three vacuum tubes, had an open loop gain of more than 300. The inner loop amplifier is also remade using a PA94. The inner loop amplifier is doubly shielded by metal bodies to prevent commingling of noise. The whole system is located in the same room (accelerator room) and is connected as close as possible to reduce the mixing of possible noises and is controlled remotely from a control room by using a programmable logic controllers (PLC, FA-M3; Yokogawa Electric Corp.)

via an Ethernet. The reference voltage and GVM feedback gain are controlled by 0 - 10 V signals from 16 bit digital-to-analog converters (DACs) in PLC. The accelerator conditions (e.g. high voltage, ripple voltage, RF voltage, RF current) are monitored using analog-to-digital converters (ADCs). The control parameters are stored in the memory space of the PLC. A personal computer used as the user interface can only refer to these parameters via an Ethernet network. Control software was designed using a LabVIEW based software. During the start-up process, control software retrieves the control parameters in the PLC and the parameters of the control software are synchronized. The control software send commands only when the control parameters changes. This framework was adopted to address the situation of a possible computer hang-up. In addition to the hardware interlock, software interlock based on the standard operational condition is developed and enables to automatic conditioning of the accelerator.

The voltage ripple of the Dynamitron accelerator was measured using a capacitive pick-off (CPO) unit with an amplifier. The CPO output was measured via an amplifier, the voltage ripple of frequencies less than 1 kHz can be measured with a sensitivity of 8 V/kV[9]. In the previous studies, a notch filter was installed between the auto regulator and the inner loop amplifier to reduce the 50-Hz component. After the modification, the intensity of the 50-Hz component was greatly reduced and a notch filter did not need to install. The peak-to-peak voltage of the ripple was reduced down to 100 Vp-p, which was two third of the previous study. Since the peak-to-peak voltage overestimated the energy resolution, voltage ripple was measured every 400 μs by an oscilloscope for 2000 s. The ripple voltage variations are summarized in Fig. 2. While the peak-to-peak voltage was 100 V, the voltage ripple distribution was ca. 20 V FWHM at a terminal voltage of 2 MV. The energy resolution of 10^{-5} was achieved.

The voltage drift at the accelerator affects the spot size of the beam. Because the microbeam experiment typically requires a few days, the voltage drift should be minimal, i.e., $\leq 10^{-4}$. We measured the voltage drift by using a generating volt meter (GVM) at 2 MV for 10 hours. Figure 3 shows the voltage drift. Terminal voltage increases for the first few hours and becomes stable after that. The voltage drift was <50 V/hour (or 1 kV/day). This may be considered rather large to maintain a constant beam size and decreases the beam current at the microbeam target. Therefore, periodic adjustment of the terminal voltage is required to optimize the target current (although a slit feedback system to reduce the voltage drift is currently under development).

3. Conclusions

The energy resolution of the accelerator was improved by developing the terminal voltage stabilizing system (TVSS) for microbeam application. The energy resolution of the accelerator was greatly improved to Ca. 1×10^{-5} $\Delta E/E$.

Acknowledgements

The authors would like to thank Dr. Arthur W Haberl of the Ion Beam Laboratory University at Albany, NY for his valuable comments, suggestions, and advice to develop TVSS. This study was partly supported by a Grant-in-Aid for Scientific Research, (B) No. 23360419, Ministry of Education, Culture, Sports, Science and Technology (MEXT) and a Grant-in-Aid for Challenging Exploratory Research Grant No. 23656583, Japan Society for the Promotion of Science (JSPS).

References

1) Matsuyama S, Ishii K, Yamazaki H, et al., *Nucl Instr Meth B* **210** (2003) 59.
2) Matsuyama S, Ishii K, Yamazaki H, et al., *Int J PIXE* **14** (2004) 1.
3) Matsuyama S, Ishii K, Abe S, et al., *Int J PIXE* **15** (2005) 41.
4) Matsuyama S, Ishii K, Tsuboi S, Y, et al., *Int J PIXE*,**21** (2011) 87.
5) Ishii K, Matsuyama S, Yamazaki H, et al., *Int J PIXE* **15** (2005) 111.
6) Ishii K, Matsuyama S, Yamazaki H, et al., *Nuc. Instr Meth B* **249** (2006) 726.
7) Ishii K, Matsuyama S, Watanabe Y, et al., *Nucl Instr Meth A* **571** (2007) 64.
8) Thompson CC, Cleland MR, *IEEE Trans Nucl Sci* **NS-16** (1969)124.
9) Langsdorf A, *IEEE Trans Nucl Sci*, **NS-30** (1983) 1453.
10) Wustenbecker S, W.Becker H, Rolfs C, et al., *Nucl Instr Meth A* **256** (1987) 9.
11) Thompson CC, *IEEE Trans Nucl Sci* **NS-14** (1967) 169.
12) Hammer JW, Fischer B, Hollick H, et al., *Nucl Instr Meth B* **161** (1987) 189.

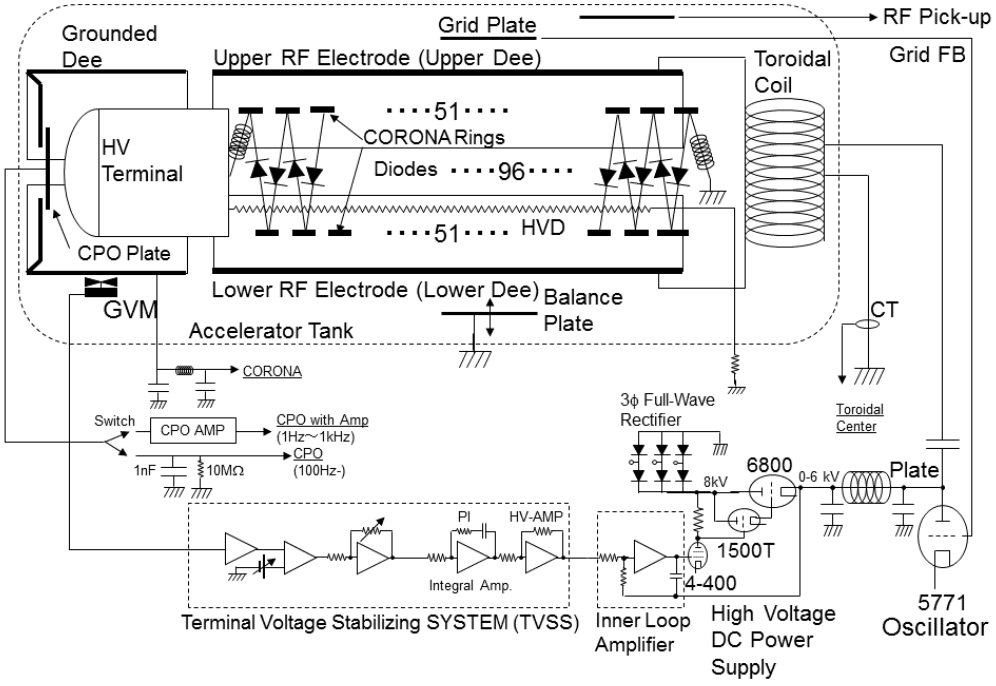

Figure 1. Schematic of the High-Voltage Generator and Control System of the Tohoku Dynamitron Accelerator.

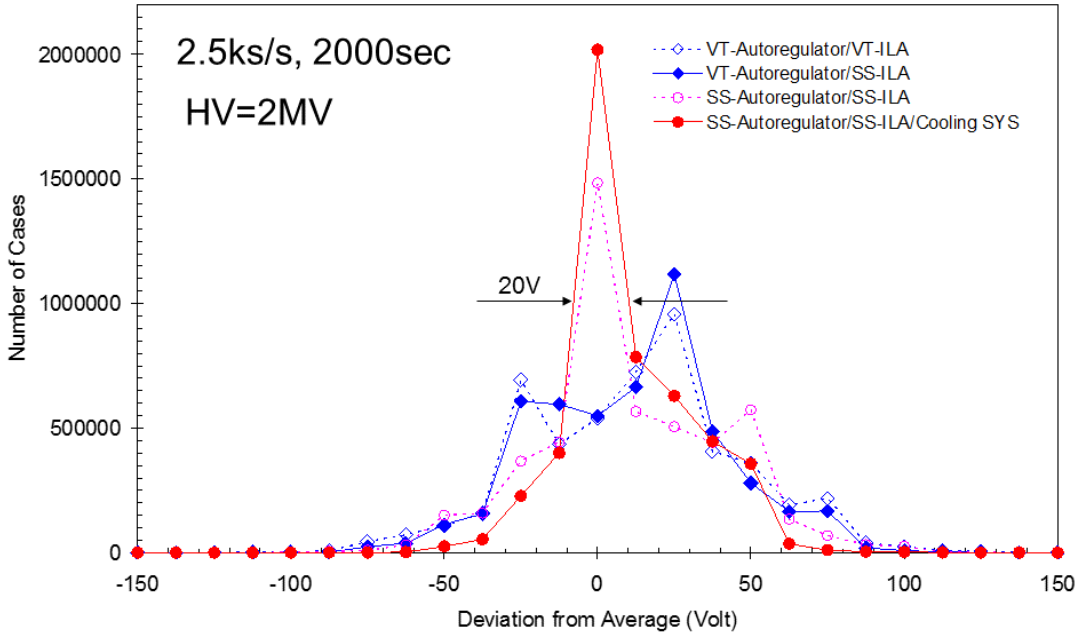

Figure 2. Voltage Ripple Distribution for Ripple Frequencies below 1 kHz.

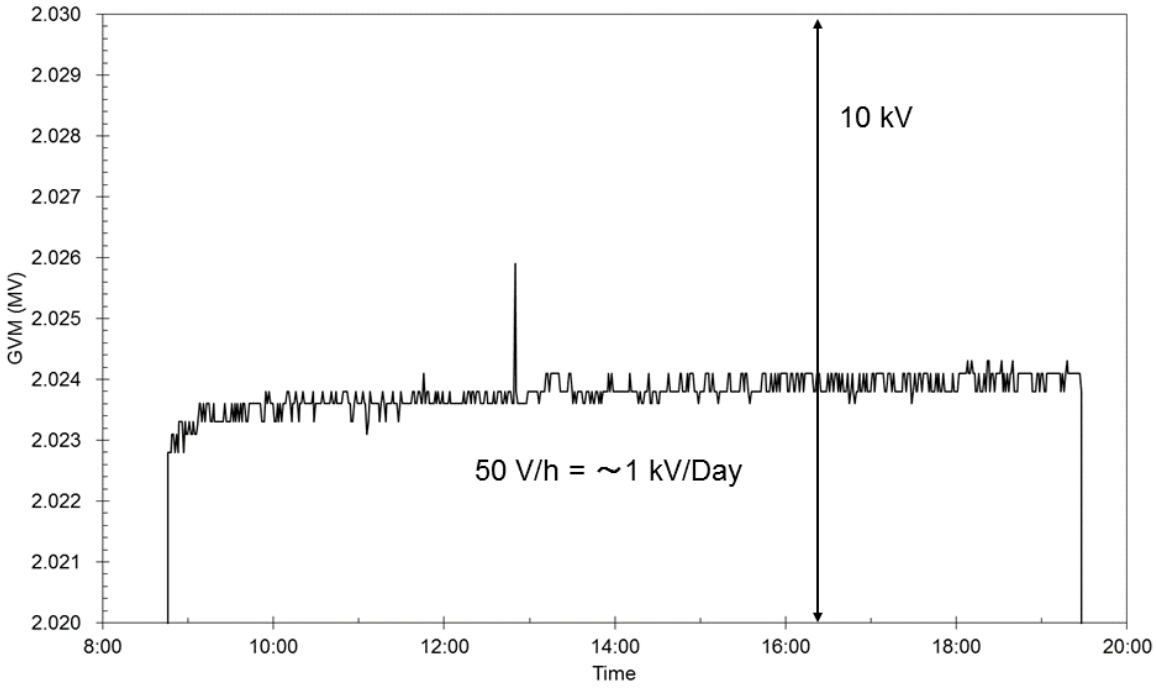

Figure 3. The measured voltage drift with a nominal Terminal voltage of 2 MV.

V. RADIOCHEMISRTY AND NUCLEAR CHEMISTRY

V. 1. Measurement of Alpha-induced Reaction Cross Sections for Cr Isotopes on Natural Ti

Kikunaga H.[1], Takamiya K.[2], Ohtsuki T.[2], and Haba H.[3]

[1]Research Center for Electron Photon Science, Tohoku University
[2]Research Reactor Institute, Kyoto University
[3]RIKEN Nishina Center

Introduction

Chromium is one of essential biotrace elements in some animals but also can be toxic in high concentrations. Understanding the behavior of chromium in animals, plants, and environment is important and influential on the various fields such as biological sciences. The radioactive tracer technique has been widely recognized as a powerful tool for behavior analysis of elements in trace amount. The isotopes ^{48}Cr (Half-life: 21.6 h), ^{49}Cr (42.3 min), and ^{51}Cr (27.7 d) have potential as radiotracers because of their suitable half-lives. In this work, the cross sections for the reactions ^{nat}Ti(α, X)^{48}Cr and ^{nat}Ti(α, X)^{49}Cr up to 75 MeV were measured to produce these isotopes efficiently and quantitatively.

Experimental

The excitation functions of these reactions were measured by the stacked-foil technique. The schematic diagram of the target stacks containing natural Ti (99.5% pure) and Al (99.9% pure) foils are illustrated in Figs. 1 (a) and (b). The target stacks shown in Figs. 1 (a) and (b) were irradiated for 30 min. with an α-particle beam delivered from the RIKEN K70 AVF Cyclotron and the model 680 Cyclotron at Cyclotron and Radioisotope Center (CYRIC), Tohoku University, respectively. The cyclotrons were operated at a beam energy of 50 MeV for RIKEN and 80 MeV for CYRIC with a mean current of around 0.4 μA.

After the irradiation, the target foils were enclosed in a polyethylene film separately and were subjected to γ-ray spectrometry using a high-purity germanium detector. The incident beam energy and flux were determined by activation of the monitor foil technique using the ^{nat}Ti(α, X)^{51}Cr and ^{27}Al(α, X)^{22,24}Na reactions. The reference data were obtained

from the IAEA Reference Data[1]. The energy loss in each foil was calculated using the TRIM code[2].

Results

The cross sections for the ^{nat}Ti(α, X)^{48}Cr and ^{nat}Ti(α, X)^{49}Cr reaction obtained in this work are shown in Fig. 2. For comparison, the earlier experimental data[3–6] of the ^{nat}Ti(α, X)^{48}Cr reaction and the values calculated using the Talys 1.6 code[7] with default parameters are shown in Fig. 3. The cross sections of ^{48}Cr obtained in this work is in good agreement with the earlier experimental data. The calculated values with the Talys code reproduce the experimental values of ^{48}Cr and ^{49}Cr with a reasonable accuracy although each peak position of the excitation functions is deviated slightly.

References

1) IAEA-Tecdoc-1211 2001 Charged particle cross section database for medical radioisotope production: diagnostic radioisotopes and monitor reactions (IAEA, Vienna, 2001).
2) Ziegler JF, et al., The stopping and range of ions in solids (Pergamon Press, New York, 1985).
3) Michel R, et al., *Radiochim Acta* **32** (1983) 173.
4) Weinreich R, et al., *Appl Radiat Isot* **31** (1980) 223.
5) Hermanne A, et al., *Nucl Instrum Meth* B **152** (1999) 187.
6) Peng X, et al., *Nucl Instrum Meth* B **140** (1998) 9.
7) Koning AJ, et al., "TALYS-1.0", *Proc Int Conf Nucl Data Sci Technol ND2007*, Nice, France, 2007-04 (EDP Sciences, 2008) p.211.

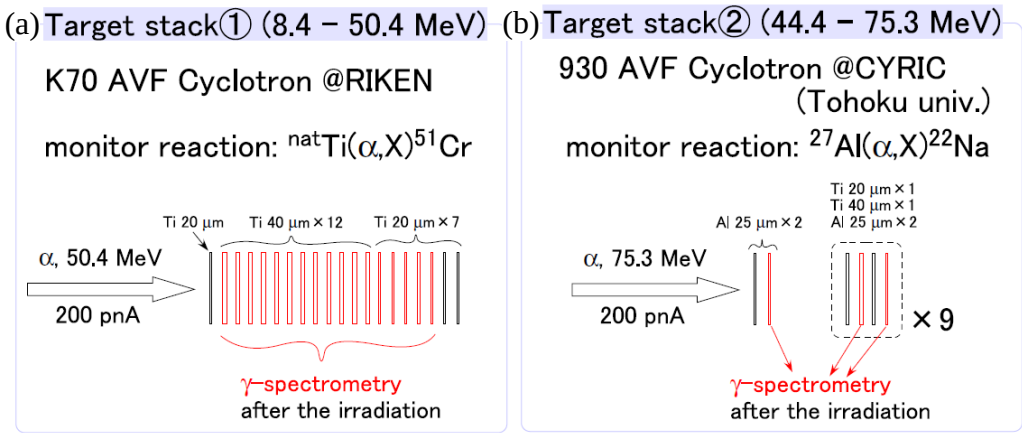

Figure 1. Schematic diagram of the target stacks for the measurement of the excitation function (a) from 8.4 to 50.4 MeV (b) from 44.4 to 75.3 MeV.

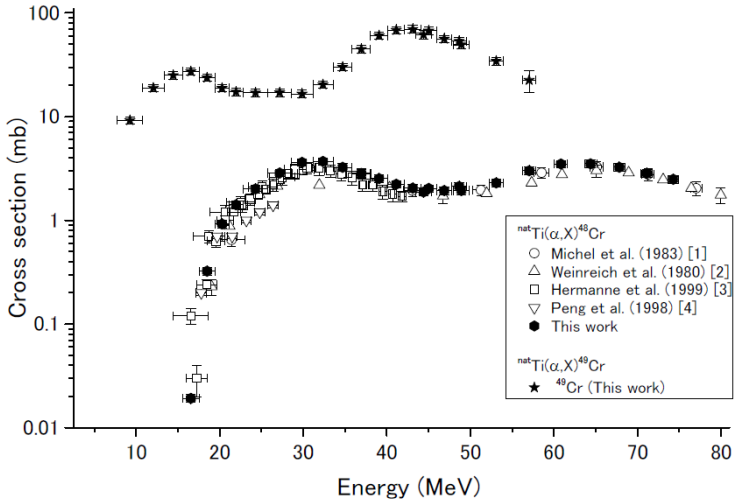

Figure 2. Cross section for the $^{nat}Ti(\alpha,X)^{48}Cr$ and $^{nat}Ti(\alpha,X)^{48}Cr$ reactions.

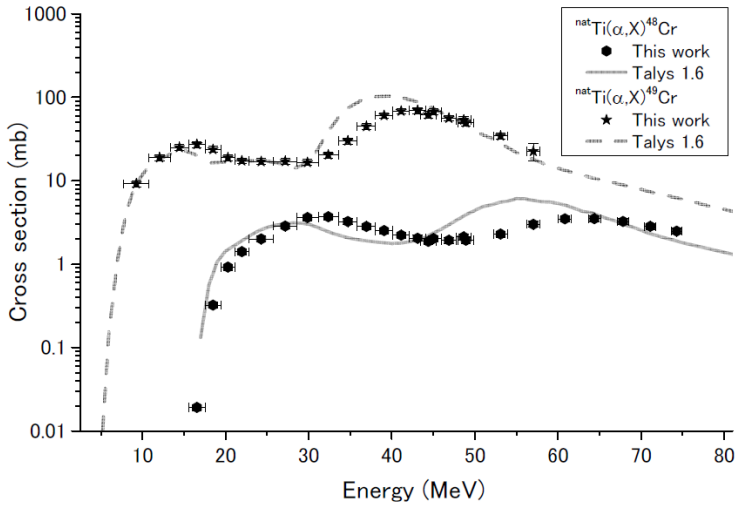

Figure 3. Comparison with the experimental data obtained and the calculated values.

VI. RADIOPHARMACEUTICAL CHEMISTRY AND BIOLOGY

VI. 1. Concentration of [^{11}C]Methyl Triflate for Microreactor Radiosynthesis of ^{11}C-Probes

Ishikawa Y.[1], Iwata R.[1], Terasaki K.[2], and Furumoto S.[1]

[1]Cyclotron and Radioisotope Center, Tohoku University
[2]Cyclotron Research Center, Iwate Medical University

A microreactor has been expected to be a powerful platform for rapid and efficient radiosynthesis of positron-emitting radiopharmaceuticals because their specific activities are generally very high; in other words, carrier amounts involved in radiosyntheses are very low, while their starting labeled precursors such as [^{11}C]methyl iodide ([^{11}C]MeI) and [^{18}F]fluoride are often produced in a large volume of gases or water. Rapid and efficient concentration of these labeled precursors is thus needed to introduce them into a microreactor. Since [^{18}F]fluoride is rather easily concentrated by a combined use of ion exchange and evaporation or more conveniently, electrochemical adsorption and release[1)], many applications have been so far reported for ^{18}F-labeled probes, whereas a very few for ^{11}C-probes[2)] for lack of a practical method for concentrating [^{11}C]MeI in a solvent in microliter volume.

[^{11}C]Methyl triflate ([^{11}C]MT), converted on-line from [^{11}C]MeI, is widely used as a more reactive ^{11}C-methylation agent than [^{11}C]MeI. It can be efficiently trapped even by water due to its higher boiling point (100-102°C). This excellent property led us to develop an automated module for trapping flowing [^{11}C]MT in a small cold trap, recovering it in a small volume of a reaction solvent and introducing it into a microreactor.

[^{11}C]MeI was produced by the gas-phase reaction of [^{11}C]methane and I_2 with a MicroLab MeI module (GE) and supplied to an automated concentration module with a He current (10~50 mL/min). The automated module consists of a AgOTf column heated at 200°C, two syringe pumps (PSD4, Hamilton), and a spiral tube cooled with a thermoelectric cooler as shown in Fig. 1. The thermoelectric cooler was made of a Peltier device (19.5 W) coupled with a small free-piston Stirling cooler (FPSC module UD08, Twinbird). Its

construction is illustrated in Fig. 2. One side of the Peltier device contacted with a metal spiral tube of stainless steel (SS) or Cu (0.3~0.75 mm i.d. x 200~400 mm long) for trapping [^{11}C]MT below -40°C and the other side with the FRSC to remove heat from the Peltier. The module was controlled with a LabVIEW software.

[^{11}C]Methyl triflate carried with He was converted on-line from [^{11}C]MeI on the AgOTf column and continuously flowed through the spiral metal tube. The tube was then warmed up to room temperature and the [^{11}C]MT trapped was eluted with acetone (25 μL/min). The trapping efficiency was obtained by varying the He flow rate and the temperature (see Table 1). The radioactivity of [^{11}C]MT was monitored with two radiation sensors located at the tube (RIS-01) and the mixing line (RIS-02), respectively. The reactivity of a recovered [^{11}C]MT was preliminarily evaluated by preparation of [^{11}C]raclopride. A solution of desmethylraclopride triflate in acetone (1 mg/400 μL) and NaOH (0.5 M, 15 μL) and the [^{11}C]MT in acetone were flowed at a rate of 25 μL/min each and mixed at an inlet of a Y-shaped micromixer (YMC KC-M-Y-SUS, 18.4 μL) at room temperature. The reaction mixture (34 μL) was added to H_3PO_4 (10 mM, 0.8 mL) and then injected into a semi-preparative HPLC column (YMC ODS-A324, 10 x 250 mm). An elution profile was compared with that obtained by the loop method[3].

The results shown in Table 1 clearly indicate that temperature was more critical than the other parameters of material and dimension of the spiral tube and He flow rate. The temperatures below -70°C gave the efficiencies of over 90%, suggesting that the melting point (-64°C) of MT was a critical temperature rather than the boiling point (100-102°C). No difference was found between SS and Cu, and no distinct effect could be drawn from the limited results for the size of tube and the He flow rate. However, it should be mentioned that the decrease in flow rate results in increasing processing time, i.e., more decay of radioactivity although it may be favorable for efficient trapping. The dimension of the tube is apparently an important parameter directly related with the volume of the recovery solvent.

Figure 3 demonstrates a typical trapping and elution profile of [^{11}C]MT (Entry 9 in Table 1). It took nearly 4 min to transfer [^{11}C]MeI from the MicroLab MeI module and flow [^{11}C]MT through the trapping tube at a He flow rate of 15 mL/min since a total volume of He needed for recovering the all from the module was ca. 60 mL. Additional flowing for a few min confirmed that the trapped [^{11}C]MT was not released into He again. Then, the [^{11}C]MT was eluted successfully in 14±6 μL acetone with a recovery of >93%. Microfluidic

radiosynthesis of [^{11}C]raclopride was carried out. Although the reaction was not optimized, it was suggested by comparison of the HPLC separation profiles that the reaction of the concentrated [^{11}C]MT was the same with that used in routine production of [^{11}C]raclopride by the loop method[3]. Further study on microreactor radiosynthesis of ^{11}C-labeld probes is in progress.

Acknowledgement− This study was supported by JSPS KAKENHI Grant Number 25461870.

References

1) Saiki H, Iwata R, Nakanishi H, et al., *Appl Radiat Isot* **68** (2010) 1703.
2) Kawashima H, et al., *Chem Pharm Bull* **63** (2015) 737.
3) Iwata R, et al., *Appl Radiat Isot* **55** (2001) 17.

Table 1. Trapping efficiency of [^{11}C]MT vs. temperature and He flow rate with various metal tube.

Entry	Spiral tube		Temperature	He flow rate	Trapping efficiency
	Material	Inner diameter x length (volume)			
5	SS*	0.75 x 300 mm (132 μL)	-44°C	50 mL/min	<1%
2	SS*	0.75 x 300 mm (132 μL)	-61°C	50 mL/min	2%
3	SS*	0.5 x 200 mm (39 μL)	-79°C	30 mL/min	96%
4	Cu	0.5 x 300 mm (59 μL)	-61°C	15 mL/min	<1%
5	Cu	0.5 x 300 mm (59 μL)	-72°C	15 mL/min	98%
6	Cu	0.5 x 300 mm (59 μL)	-74°C	15 mL/min	95%
7	Cu	0.3 x 400 mm (28 μL)	-74°C	10 mL/min	99%
8	Cu	0.3 x 200 mm (14 μL)	-74°C	10 mL/min	98%
9	Cu	0.3 x 200 mm (14 μL)	-85°C	15 mL/min	98%

*Stainless steel

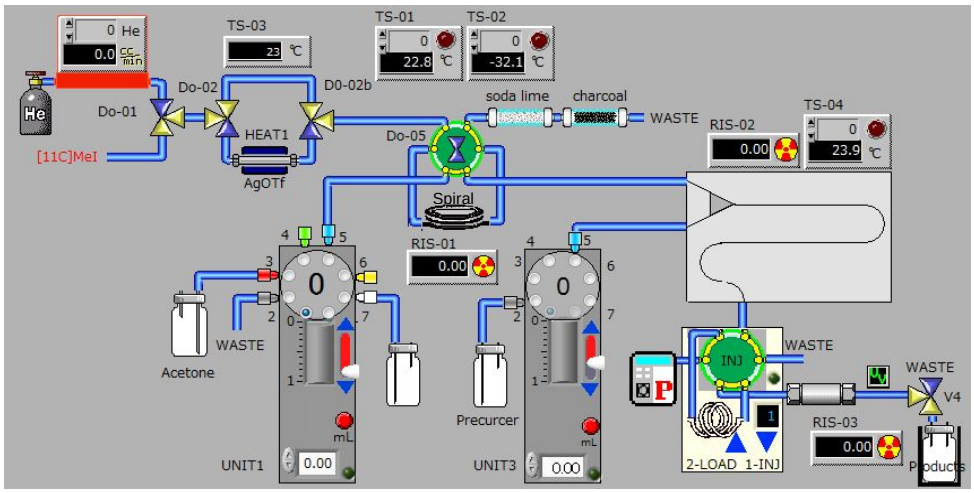

Figure 1. A PC control view of the automated concentration module and reaction/HPLC separation modules.

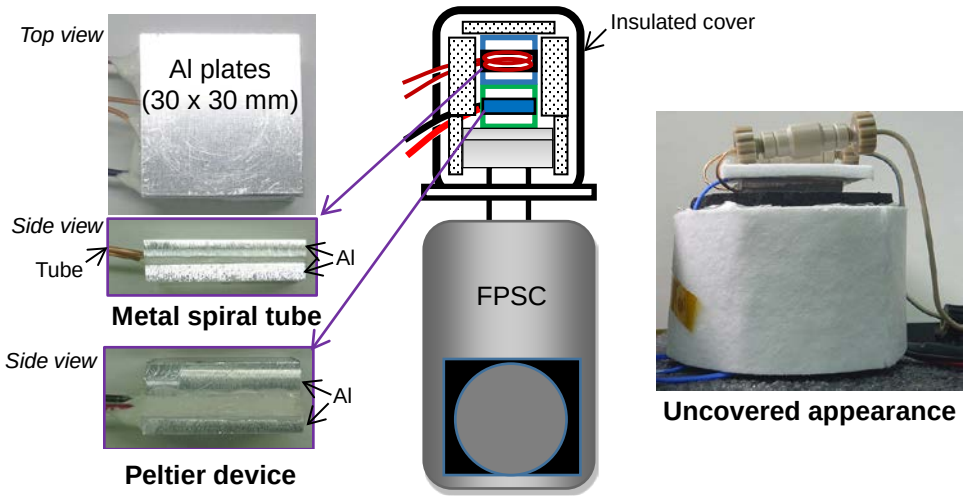

Figure 2. Construction of a trap of flowing [^{11}C]MT with metal tube cooled with a thermoelectric cooler.

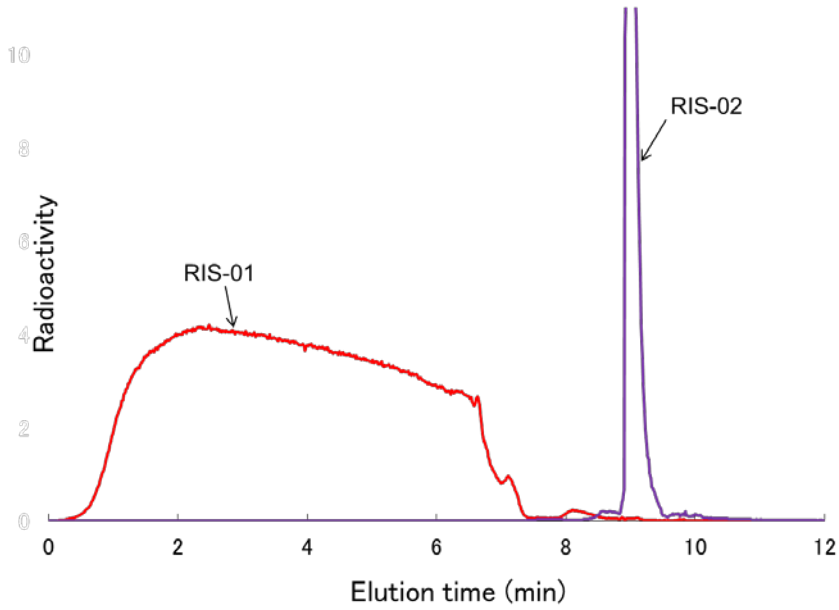

Figure 3. A typical trapping and eluting profile of [^{11}C]MT.

VI. 2. Preparation of [^{18}F]FRP-170 by Microfluidics and Solid-phase Extraction

Iwata R.[1], Terasaki K.[2], Takahashi K.[3,], Ishikawa Y.[1], and Furumoto S.[1]*

[1]Cyclotron and Radioisotope Center, Tohoku University
[2]Cyclotron Research Center, Iwate Medical University
[3]Riken Center for Molecular Imaging Science

[^{18}F]FRP-170 was developed as a hypoxic imaging probe at CYRIC[1)] and has been extensively applied to clinical research at several PET centers in Japan[2-5)]. It was originally prepared with a conventional method based on ^{18}F-fluorination in a glass vessel and HPLC purification, and later modified by introducing on-column deprotection for simplification of the synthetic procedure[6)].

Microfluidics is expected to offer an excellent platform for rapid and efficient radiosynthesis of ^{18}F-radiopharmaceuticals. Its advantages over conventional radiochemistry have been demonstrated in many ^{18}F-PET probe radiosyntheses. We developed a new method for electrochemical concentration of aqueous [^{18}F]fluoride into an aprotic solvent such as acetonitrile[7)] and successfully applied it to microfluidic radiosynthesis of several ^{18}F-radiopharmaceuticals[8)]. In this report, we applied this concentrated [^{18}F]fluoride to the preparation of [^{18}F]FRP-170. The ^{18}F-fluorination in a microfluidic chip was optimized and [^{18}F]FRP-170 with high chemical and radiochemical purities was conveniently prepared by alkali hydrolysis and purification on a single solid-phase extraction (SPE) cartridge.

[^{18}F]Fluoride was produced in ^{18}O-enriched water with the HM-12 cyclotron at CYRIC. It was flowed through a disposable flow chip, where it was electrochemically trapped by carbon electrode, washed with acetonitrile (MeCN) and then released into a small volume of anhydrous MeCN containing a Kryptofix 2.2.2-$KHCO_3$ complex ([K/K.222]HCO_3). The [K/K.222][^{18}F]F recovered from the chip was reacted with the

[*]Present address: Keio University School of Medicine.

precursor in a microfluidic chip according to the scheme shown in Fig. 1. The whole radiosynthesis was carried out on a specially developed automated microreactor module (Shimadzu Corp.) as shown in Fig. 2. The reaction solution eluted from the chip (200 μL/min) was on-line diluted with water (4.0 mL/min) and the mixture was passed through a commercially available SPE cartridge: Sep-Pak Plus tC18 Short, tC18 Long, or PS2 (Waters), or Supelclean ENVI-Carb 100 mg or 250 mg (Supelco). The cartridge was washed with water (10 mL) and then filled with NaOH (0.5 M). After the cartridge was allowed to stand at room temperature for 1 min, NaOH was washed out with water (10 min). The hydrolyzed products on the SPE cartridge were then eluted with water containing ethanol (EtOH) and analyzed by HPLC on a YMC-Triart C18 column (4.6 x 150 mm) with a solvent system of MeCN/H_2O (40:60) at 2.0 mL/min. RP-170 derived from the precursor was quantified by HPLC on an Waters Puresil C18 column (4.6 x 150 mm) with a solvent system of MeCN/H_2O (7:93) at 2.0 mL/min and 280 mm UV.

The conditions were optimized for microfluidic reaction on precursor concentration, time and temperature since the reaction solvent was replaced from dimethylformamide (DMF) to MeCN in the present synthesis. As seen in Figs. 3a-c higher ^{18}F-fluorination yields of over 80% were obtained with the optimal conditions of 5 mg/mL, 0.125 min and 130ºC than those by the conventional method with DMF[1,6]. Microfluidics thus proved to be very powerful for improving radiochemical yields of ^{18}F-radiopharmaceuitcals.

Another advantage expected from microfluidic radiosynthesis is to decrease amounts of precious reagents such as a precursor. In the present microfluidic reaction, however, the precursor amount was decreased only by 0.5 mg (from 2.0 to 1.5 mg) owing to the increased concentration for higher radiochemical yields. Nevertheless, the decrease in precursor amount encouraged us to develop a simple purification method with a SPE cartridge. The same SPE cartridge was used for on-column hydrolysis with NaOH followed by separation of [^{18}F]FRP-170 from other radioactive and non-radioactive byproducts. As seen in Fig. 4a, the hydrolysate contained more polar products than [^{18}F]FRP-170 such as [^{18}F]fluoride and RP-170 and less polar products such as the precursor and partially hydrolyzed products such as Ac-[^{18}F]FRP-170 and Tos-RP-170. Elution of the cartridge with water removed NaOH and the polar products. Subsequent elution with water containing 10% EtOH from a tC18 cartridge gave fairly good recovery of [^{18}F]FRP-170 with high radiochemical purity, whereas a noticeable amount of Tos-RP-170 was observed as seen in Fig. 4b. The [^{18}F]FRP-170

obtained with PS2 and Supelclean ENVI-Carb (250 mg) cartridges suffered from very low recovery probably due to its strong adsorption. Increase in the EtOH content improved the recovery but considerably lowered chemical purity. Among the cartridges examined, Supelclean ENVI-Carb (100 mg) gave satisfactory radiochemical yields of [^{18}F]FRP-170 (55±6%, n=12) and high radiochemical (>99%) and good chemical purities. The amount of RP-170 in the EtOH eluate, however, was estimated to be >20 μg/mL. Since our regulatory recommendation on clinical use of [^{18}F]FRP-170 requires that the maximum injection amount of RP-170 should be 5.5 μg, further efforts to decrease this amount was made. Washing the cartridge with 4% EtOH (20 mL) instead of water (10 mL) successfully decreased the amount below 1 μg/mL by discarding nearly half of the [^{18}F]FRP-170. A [^{18}F]FRP-170 injection with both high chemical radiochemical purities was consequently prepared in radiochemical yields of 38±3% (n=5) by microfluidics and SPE.

Acknowledgement− This study was supported by JSPS KAKENHI Grant Number 25293257.

References

1) Wada H, Iwata R, Ido T, Takai Y, *J Label Compd Radiopharm* **43** (2000) 785.
2) Kaneta T, et al., *J Nucl Med* **43** (2002) 109.
3) Kaneta T, et al., *Ann Nucl Med* **21** (2007) 101.
4) Beppu T, et al., *Mol Imag Biol* **16** (2014) 127.
5) Beppu T, et al., *Ann Nucl Med* **29** (2015) 336.
6) Ishikawa Y, Iwata R, Furumoto S, Takai Y, *Appl Radiat Isot* **62** (2005) 705.
7) Saiki H, Iwata R, et al., *Appl Radiat Isot* **68** (2010) 1703.
8) Wong R, Iwata R, et al., *Appl Radiat Isot* **70** (2012) 193.

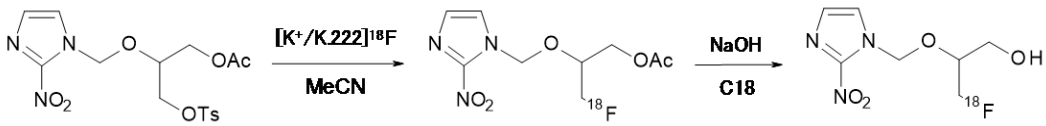

Figure 1. Synthetic scheme of [^{18}F]FRP-170.

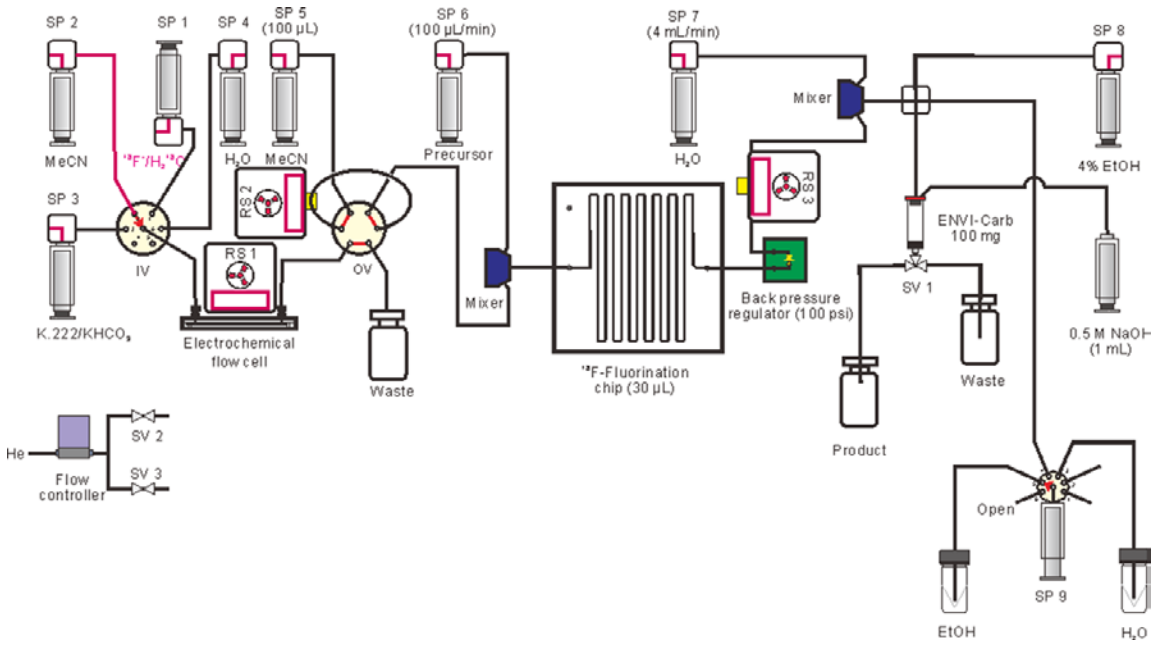

Figure 2. A schematic diagram of the automated microreactor module based on electrochemical concentration method of [^{18}F]fluoride.

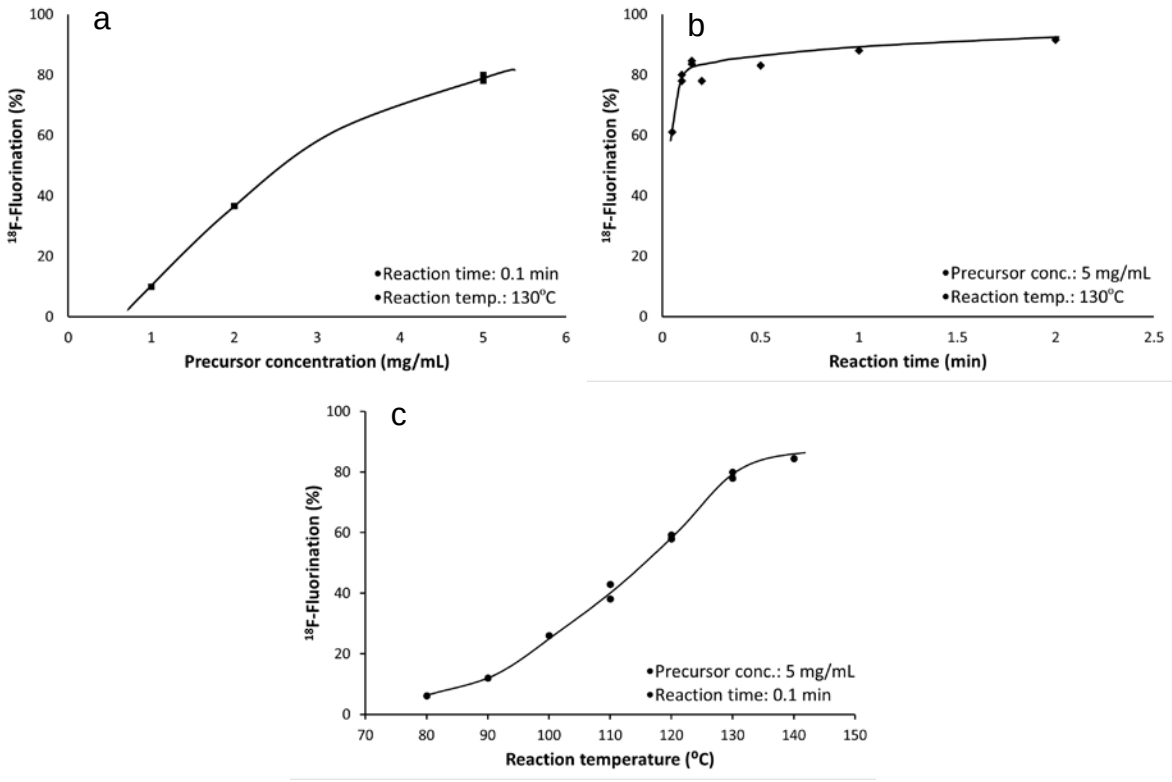

Figure 3. Correlations of ^{18}F-fluorinations with (a) precursor concentration, (b) reaction time and (c) reaction temperature.

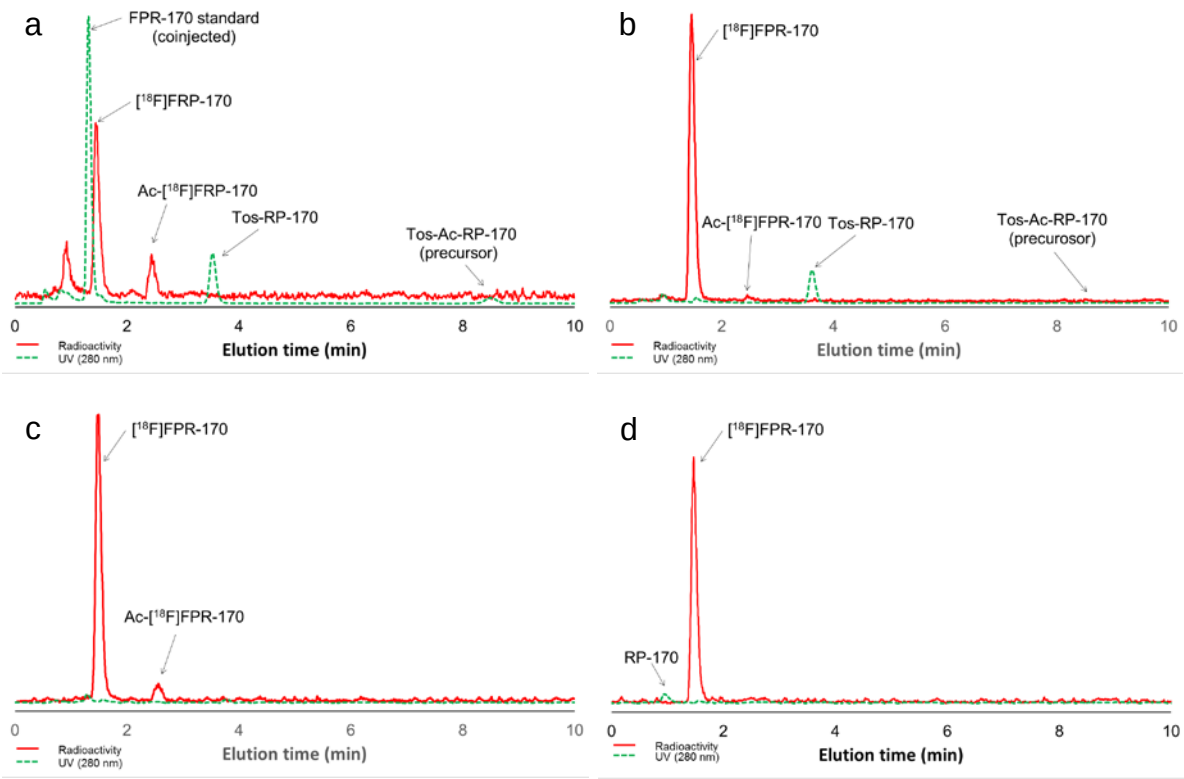

Figure 4. HPLC analyses of (a) the reaction products and the purified [^{18}F]FRP-170 with (b) Sep-Pak Plus tC18 Long, (c) Sep-Pak Plus PS2 and (d) Supelclean ENVI-Carb 100 mg.

VI. 3. Structure-activity Relationship Study of 2-Arylquinoline Derivatives for Tau Imaging in Alzheimer's Disease

Tago T.[1,], Furumoto S.[1], Okamura N.[2,†], Harada R.[3], Adachi H.[1], Ishikawa Y.[1], Yanai K.[1,2], Iwata R.[1], and Kudo Y.[3]*

[1]*Cyclotron and Radioisotope Center, Tohoku University*
[2]*Tohoku University School of Medicine*
[3]*Institute of Development, Aging and Cancer, Tohoku University*

Introduction

Abnormal deposits of amyloid-β and hyperphosphorylated tau protein in the brain cortex are the pathological hallmarks of Alzheimer's disease (AD). In this decade, many radiolabeled small-molecule probes have been developed for the purpose of non-invasive imaging of these pathologies by positron emission tomography (PET)[1)]. Previously, we reported ^{18}F-labeled 2-aryluqinoline (2-AQ) probes which showed selective binding to tau and high brain uptake followed by rapid clearance from the brain in normal mice[2)]. However, they showed a marked white matter retention in both healthy controls and AD patients in the initial clinical studies[3)]. Such characteristics should be minimized in the development of a tau probe because it may complicate visual inspection of PET images. In this study, we conducted a structure-activity relationship study of 2-AQ derivatives to develop a high performance tau PET probe with low background radioactivity in the brain[4)].

Materials and Methods

Radiosyntheses of 2-AQ derivatives were achieved by general nucleophilic substitution with [^{18}F]KF and tosylate precursors. Binding characteristics of compounds were evaluated by autoradiography (ARG) with AD brain sections. *In vitro* binding assays were performed to evaluate the binding affinity for AD brain homogenate. The experiments with human samples were performed under the regulations of the ethics committee of Tohoku

[*]*Present address: Tokyo Metropolitan Institute of Gerontology*

[†]*Present address: Tohoku Medical and Pharmaceutical University*

University School of Medicine. Blood-brain barrier permeability was determined by biodistribution assay with male ICR mice. Metabolism analysis was also performed in mice. The experiments using mice were approved by the Committee on the Ethics of Animal Experiments at Tohoku University School of Medicine.

Results and Discussion

We synthesized fifteen ^{18}F-labeled 2-AQ derivatives (Fig. 1), and the radiochemical yields ranged from 11 to 72% (decay corrected). The specific activities ranged from 16.1 to 118 GBq/μmol. Their radiochemical purities were greater than 99%. Binding assays suggested that most 2-AQ derivatives with a side-chain on position 6 of the quinoline showed higher binding affinity to tau aggregates in AD brain homogenates (K_d: 2.60~11.5 nM); meanwhile, those of derivatives with a side-chain on position 7 of the quinoline or position 3' of the benzene were much lower than other tested compounds. A similar tendency of the binding affinity of compounds was seen in ARG assay with AD brain sections. All derivatives showed high initial brain uptakes ranging from 2.72 percent injected dose (%ID)/g to 9.20 %ID/g in mice. A correlation between the brain uptake ratio 2 min over 10 min post-injection and the lipophilicity suggested that lower lipophilic derivatives tended to exhibit faster washout from the brain.

From the results of the above experiments, we selected a pyridinyl compound named [^{18}F]THK-5151 as the most promising candidate for tau PET imaging. [^{18}F]THK-5151 has a chiral center in its (3-fluoro-2-hydroxy)-1-propoxyl side-chain and thus has two optical isomers called enantiomers. Enantiomers often differ in biological activities such as pharmacokinetics and metabolism; therefore, we synthesized [^{18}F]THK-5351 (*S*-enantiomer) and [^{18}F]THK-5451 (*R*-enantiomer) and evaluated their properties as tau probes. Both enantiomers showed high tau selective binding and low nonspecific binding to white matter in ARG assay (Fig. 2). Interestingly, the biodistribution study in mice revealed that [^{18}F]THK-5351 had a faster clearance from the brain and blood compared with [^{18}F]THK-5451 (Fig. 3A, B). Additionally, bone radioactivity of [^{18}F]THK-5451 injected mice was higher than that in [^{18}F]THK-5351 injected mice, suggesting that [^{18}F]THK-5451 is more susceptible to *in vivo* defluorination than its antipode (Fig 3C). These pharmacokinetic differences between enantiomers were seemed to be caused by stereoselectivity in metabolism.

Conclusion

This structure-activity relationship study revealed the appropriate chemical characteristics of 2-AQ derivatives for tau probes such as ^{18}F-labeling side-chain, fundamental framework and lipophilicity. Altogether, [^{18}F]THK-5351 showed outstanding binding property and pharmacokinetics among tested compounds, and now evaluation of its clinical utility is ongoing by PET studies in AD patients[5)].

References

1) Villemagne VL, Fodero-Tavoletti MT, Masters CL, et al., *Lancet Neurol* **14** (2015) 114.
2) Okamura N, Furumoto S, Harada R, et al., *J Nucl Med* **54** (2013) 1420.
3) Harada R, Okamura N, Furumoto S, et al., *Eur J Nucl Med Mol Imaging*. **42** (2015) 1052.
4) Tago T, Furumoto S, Okamura N, et al., *J Nucl Med* **57** (2016) 608.
5) Harada R, Okamura N, Furumoto S, et al., *J Nucl Med* **57** (2016) 208.

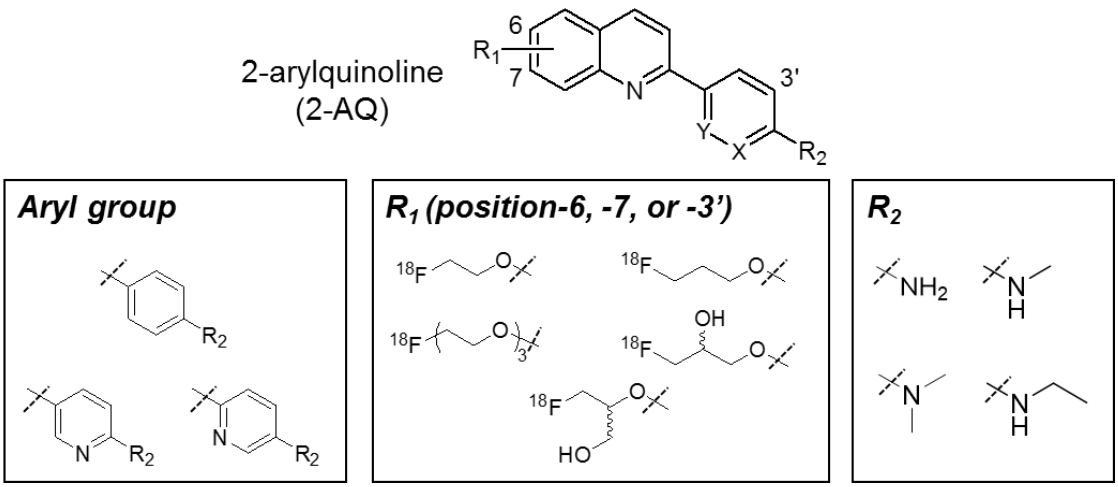

Figure 1. Fundamental structure of [^{18}F]2-AQ derivatives (top) and partial structures investigated in this study (bottom squares).

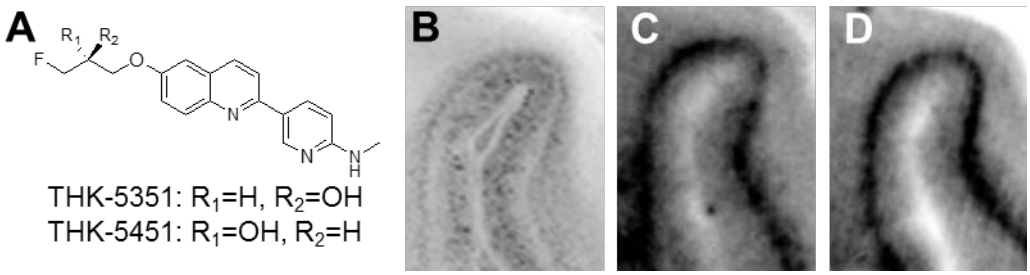

Figure 2. **A**: Chemical structures of THK-5151 enantiomers. **B**-**D**: Tau (Gallyas-Braak) staining (**B**) and

autoradiograms of AD brain sections of [^{18}F]THK-5451 (**C**) and [^{18}F]THK-5351 (**D**).

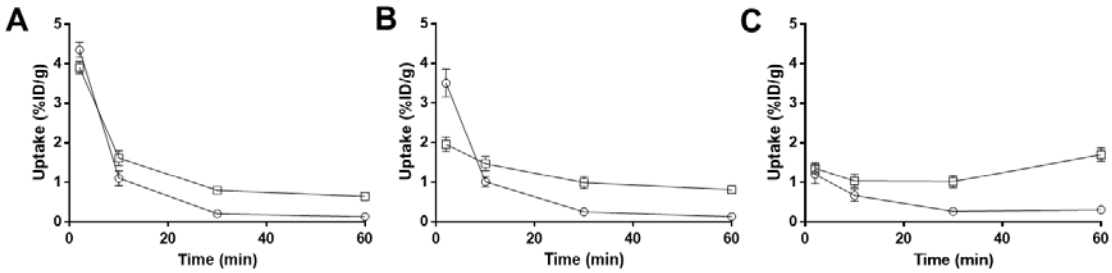

Figure 3. Biodistribution of [^{18}F]THK-5151 enantiomers in mice brain (**A**), blood (**B**) and bone (**C**). circles: [^{18}F]THK-5351; squares: [^{18}F]THK-5451.

VI. 4. Development of ^{18}F-labeled Phosphonium Derivatives for Mitochondria Imaging by PET

Furumoto S., Tominaga T., Itoh H., Ishikawa Y., and Iwata R.

Cyclotron and Radioisotope Center, Tohoku University

Introduction

Triarylphosphonium (TAP) cation has the property of passing through the cell membrane and accumulating in mitochondria depending on mitochondria membrane potential (MMP). ^{18}F-Labeled TAP derivatives such as [^{18}F]fluorobenzyltriphenyl-phosphonium ([^{18}F]FBnTP) are tend to accumulate in heart tissue like [^{99m}Tc]sestamibi and [^{99m}Tc]tetrofosmin, and thus are expected to be used for myocardial perfusion imaging (MPI) agents by positron emission tomography (PET). Although [^{18}F]FBnTP has been used as a "gold standard" PET tracer for MPI[1,2], a corrosive liquid reagent and complicated processes are necessary for the radiosynthesis of the tracer. Biologically, this tracer shows high accumulation in the liver as same as in the heart that may be caused by slow clearance from the liver. In this study, we tried a new method to simplify the preparation of [^{18}F]FBnTP. Then, we designed and synthesized a [^{18}F]FBnTP derivative ^{18}F-labeled-triethylene glycol side chain by the new synthesis method and evaluated the biodistribution property[3].

Methods

A conventional method for [^{18}F]FBnTP synthesis requires the use of Ph_3PBr_2, a corrosive liquid reagent, for conversion of [^{18}F]FBnOH to [^{18}F]FBnBr which reacts with triarylphosphine to form a phosphonium structure. To make this process simplified, we used triphenylphosphine hydrobromide (PPh3•HBr) for direct preparation of [^{18}F]FBnTP from ^{18}F-fluorobenzyl alcohol (Fig. 1A). [^{18}F]FPEGBnTP was also synthesized from [^{18}F]FPEG-BnOH and PPh3•HBr (Fig. 1B). The ^{18}F-labeled phosphoniums were purified by semi-preparative HPLC. Lipophilicity of FBnTP and FPEGBnTP, that is, their octanol/water partition coefficient (LogP) were measured by conventional method. A radiotracer uptake assay and an MMP assay using human cholangiocarcinoma cells (TFK1) and human breast cancer cells (MCF7, MB231, MB453) were performed for evaluation of an MMP-dependent

cellular uptakes of [^{18}F]FPEGBnTP. Then, biodistribution of [^{18}F]FPEGBnTP in normal mice was assessed.

Results and Discussions

Ph_3PBr_2 is not suitable for automatic synthesis devices or conventional uses because it is highly corrosive and unstable to moisture. To avoid such disadvantages, we considered the use of PPh3•HBr, which is stable in the air and react with benzyl alcohol to form a phosphonium structure in one step. Using this reagent, [^{18}F]FBnTP and [^{18}F]FPEGBnTP were successfully prepared in the yields of 12–14% (n=5) and 13–23% (n=8), respectively (decay-corrected). LogP values of FBnTP and FPEGBnTP were -0.38 and -0.92, respectively, indicating that FPEGBnTP is relatively less lipophilic than FBnTP. Cellular uptakes of [^{18}F]FPEGBnTP and MMPs of the four cell lines were summarized as a scatter diagram (Fig. 2). The diagram shows a linear correlation ($R^2 = 0.9972$) between the relative intensity of MMP and cellular uptake values, suggesting the MMP-dependency of the cellular incorporation of [^{18}F]FPEGBnTP. Biodistribution study revealed that [^{18}F]FPEGBnTP tend to accumulate mainly in the heart and kidney (Fig. 3). Furthermore, the tracer shows the lower retention in the liver, resulting in a higher ratio of heart/liver (4.0±0.28 at 60 min) in comparison to that of [^{18}F]FBnTP (1.5±0.61 at 60 min) reported by Madar et al .[2)], indicating that the liver pharmacokinetics of [^{18}F]FPEGBnTP was improved. The time-dependent increase of radioactivity in the bone suggests a low tolerance to defluorination of [^{18}F]FPEGBnTP *in vivo* and further chemical modification to show better *in vivo* stability.

Conclusions

In this study, we established a new synthetic route for [^{18}F]FBnTP using PPh_3•HBr instead for Ph_3PBr_2. According to this method, [^{18}F]FPEGBnTP, a newly PEGylated [^{18}F]FBnTP derivative, was developed. The tracer incorporated into a particular cancer cell line in proportion to the MMP *in vitro* and highly accumulated in the heart *in vivo*, suggesting that [^{18}F]FPEGBnTP would be a possible candidate for a new ^{18}F-labeled MPI agent.

References

1) Ravert HT, Madar I, Dannals RF, *J Label Compd Radiopharm* **47** (2004) 469.
2) Madar I, Ravert HT, Du Y, Hilton J, Volokh L, Dannals RF, Frost JJ, Hare JM, *J Nucl Med* 47 (2006) 1359.
3) Tominaga T, Ito H, Ishikawa Y, Iwata R, Ishiwata K, Furumoto S, *J Label Compd Radiopharm* **59** (2016) 117.

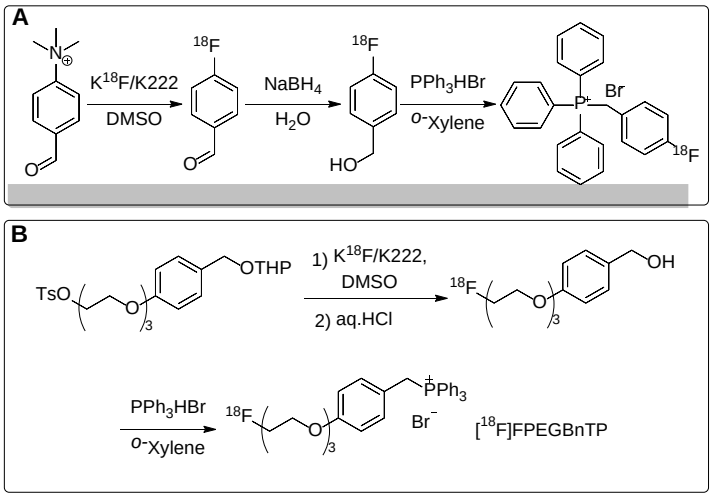

Figure 1. Radiosynthesis schemes of [^{18}F]FBnTP (A) and [^{18}F]FPEGBnTP (B).

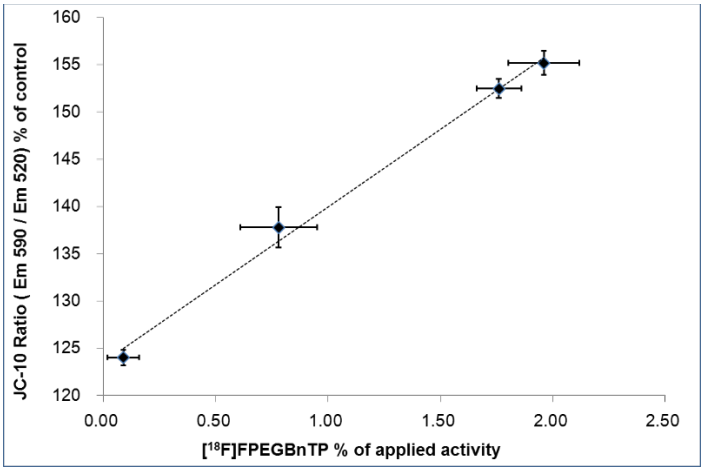

Figure 2. Correlation between cellular uptake of [^{18}F]FPEGBnTP and MMP intensity (JC-10 ratio). A linear correlation was observed ($R^2 = 0.9972$).

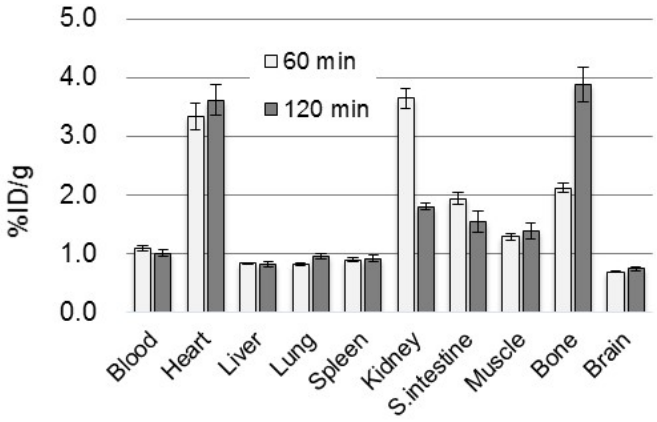

Figure 3. Biodistribution of [^{18}F]FPEGBnTP in normal mice.

VI. 5. Development of ^{18}F-labeling Method for Proteins Using a Cell-free Translation System and ^{18}F-fluoro-L-proline

Harada R.[1], Furumoto S.[2], Yoshikawa T.[1], Ishikawa Y.[2], Iwata R.[2], and Yanai K.[1]

[1]Tohoku University School of Medicine
[2]Cyclotron and Radioisotope Center, Tohoku University

Introduction

PET is a noninvasive molecular imaging technique that visualizes physiologic and pathologic conditions using PET radiopharmaceuticals. Although small molecules based PET radiopharmaceuticals such as ^{18}F-fluorodeoxyglucose (FDG) are widely used in clinical practice and research, bioactive proteins are of interest for PET radiopharmaceuticals to evaluate physiological functions, potentially diagnose diseases, and characterize pharmacokinetics themselves[1)]. We previously proposed a novel strategy for labeling proteins using a cell-free translation system and ^{11}C-methionine[2,3)]. However, in general proteins tend to show slower kinetics than small molecules, thus requiring a longer scanning time[4)]. Here, we show expanded our strategy using a cell-free translation system and ^{18}F-labeled amino acid (Fig. 1). Since ^{18}F-labeled amino acids are unnatural amino acid, it is not easy to incorporate into proteins directly unlike ^{11}C-methionine. Therefore, we searched several fluorinated amino acids that meet criteria for labeling proteins such as easily labeled with ^{18}F and incorporation into proteins instead of natural amino acid and tried to demonstrate proof of concept of our strategy.

Methods

PURExpress® (New England BioLabs) is used in this study as a cell-free translation system because it can be easily customized with respect to the components of the reaction solution. We choose interleukin-8 (IL-8) as a model protein. The reaction solution contains PURExpress reagents and fluorinated amino acids such as (*2S, 4R*)-4-fluoro-L-proine (*trans*-FPro), (*2S, 4S*)-4-fluoro-L-proine (*cis*-FPro), *O*-fluoroethyl-L-tyrosine, and *O*-fluoromethyl-L-tyrosine[5)] instead of each natural amino acids. After incubation at 37°C for 2 hrs, the

samples were analyzed by western blotting (IL-8) and MALDI-TOF MS. Next, we characterized the binding ability of fluorinated IL-8 variants using in vitro competitive binding assay. Finally, ^{18}F-IL-8 was prepared using PURExpress® and ^{18}F-fluoro-L-proline and investigated its pharmacokinetics and utility using Xenograft-bearing mice with small animal PET.

Results

Western blotting showed the fluoro-L-proline (FPro) successfully incorporated into IL-8 instead of natural L-proline, but not fluorinated tyrosine derivatives. FPro has stereoisomers including *trans*-FPro and *cis*-FPro. There were no significant differences in the amounts of synthesized IL-8 between FPro isomers determined by IL-8 ELISA. MALDI-TOF MS also confirmed that incorporation of FPro into IL-8 instead of natural L-proline.

In vitro competitive binding assays using IL-8RA expressing cells indicated that IL-8 variants containing FPro completely inhibited the ^{125}I-IL-8 binding to IL-8RA and showed lower IC_{50} values than wild-type IL-8. The *trans*-FPro variant bound to IL-8 RA with higher affinity (IC_{50} = 1.5 ± 0.1 nM) than the *cis*-FPro variant (IC_{50} = 3.0 ± 0.3 nM). Therefore, we chose *trans*-FPro as an ^{18}F-labeled amino acid source for further investigation.

Trans-^{18}F-FPro was successfully prepared with sufficient radiochemical yield (decay corrected, 30-40%) as previously reported[6]. Next, we investigated whether *trans*-^{18}F-FPro can be incorporated into IL-8 like unlabeled FPro. Gel autoradiography showed a radioactive band at approximately 10kDa, which is consistent with the results of western blotting of IL-8 and the radioactive bands were increased in a time dependent manner (Fig. 2A). After incubation for 120 min to yield maximum amount of radioactive proteins, ^{18}F-IL-8 was purified using a cation exchange spin column within 30 min, with resulting radiochemical purity exceeding 92% determined by gel autoradiography (Fig 2B).

^{18}F-IL-8 showed rapid distribution in the body of mice and the largest uptake in the kidneys and then gradually accumulated in the bladder. The PET images summed from 60 to 130 min after intravenous administration of ^{18}F-IL-8 and *trans*-^{18}F-FPro are shown in Fig. 3. ^{18}F-FPro clearly showed tracer uptake in IL-8 RA xenografts with high contrast, whereas *trans*-^{18}F-FPro did not.

Conclusions

The present study demonstrated proof of concept of our strategy for the labeling

proteins with ^{18}F using a cell-free translation system and *trans*-^{18}F-FPro. We successfully expanded our strategy from ^{11}C to ^{18}F, which is preferable for proteins with slower pharmacokinetics. However, there are several limitations such as 1) the lower radiochemical yield than conventional labeling methods for ^{18}F and 2) slow incorporation rate of *trans*-^{18}F-FPro. To overcome these limitations, further improvement will be needed using novel techniques.

References

1) Miller PW, Long NJ, Vilar R, Gee AD, *Angew Chem Int Ed Engl* **47** (2008) 8998.
2) Harada R, Furumoto S, Yoshikawa T, et al., *Nucl Med Biol* **39** (2012) 155.
3) Matsuda T, Furumoto S, Higuchi K, et al., *Bioorg Med Chem* **20** (2012) 6579.
4) Wu ZH, Kandeel F, *Curr Pharmaceut Biotech* **11** (2010) 572.
5) Iwata R, Furumoto S, Pascali C, Bogni A, Ishiwata K., *J Label Compd Radiopharm* **46** (2003) 555.
6) Hamacher K, *J Label Compd Radiopharm* **42** (1999) 1135.

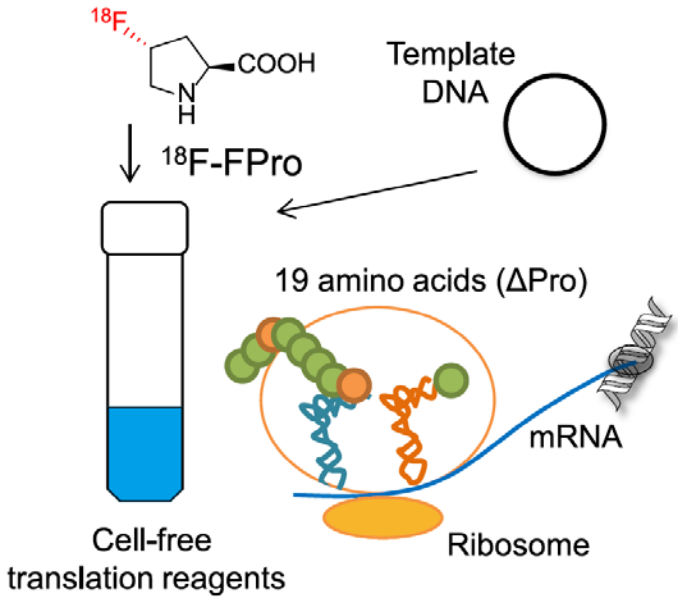

Figure 1. Schematic illustration of our strategy for labeling of protein with ^{18}F.

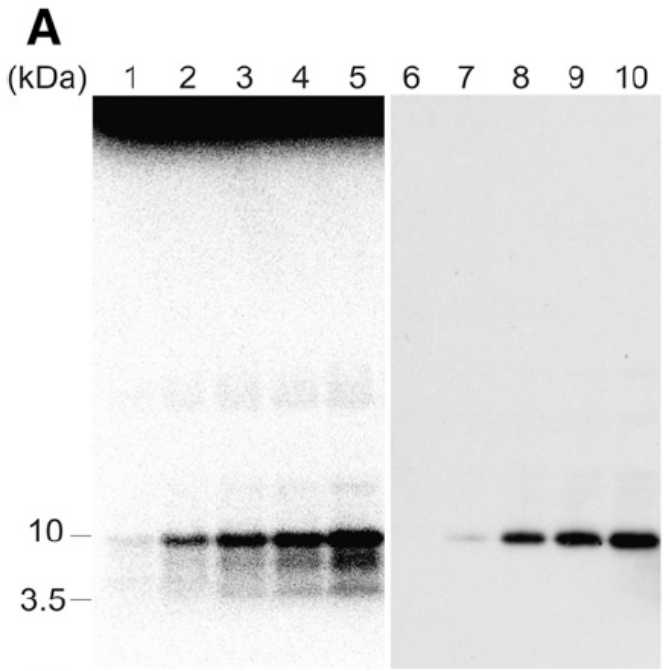

Figure 2. Radiosynthesis of ^{18}F-IL-8 using PURExpress and trans-^{18}F-fluoro-L-proline. (A) gel autoradiograhy and western blotting (IL-8): Lanes 1(6), 2(7), 3(8), 4(9), and 5(10): incubation for 15, 30, 60, 90 and 120 min (B) Chromatogram of ^{18}F-IL-8 from the gel autoradiography analysis

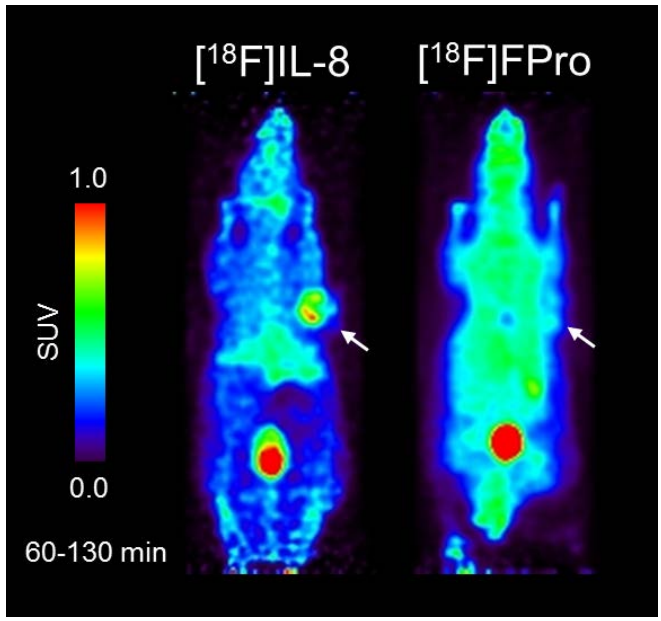

Figure 3. ^{18}F-IL-8 and trans-^{18}F-fluoro-L-proline PET images from 60 to 130 min in IL-8RA expressing xenograft-bearing mice after injection of radiotracers.

VI. 6. Measurement of Free Fraction in Plasma for Biomathematical Prediction of *SUVR* of Amyloid PET Radiotracers

Nai Y.-H.[1,2], Shidahara M.[1,3], Seki C.[4], Watanuki S.[1], Funaki Y.[1], Ishikawa Y.[1], Furumoto S.[1], and Watabe H.[1,2]

[1]Cyclotron and Radioisotope Center, Tohoku University
[2]Graduate School of Biomedical Engineering, Tohoku University
[3]Graduate School of Medicine, Tohoku University
[4]National Institute of Radiological Sciences

Introduction

Alzheimer's Disease (AD) is a form of dementia, defined by histopathological features like senile plaques and neurofibrillary tangles, with clinical symptoms such as loss of memory & executive functions, which may only be apparent many years later[1)]. As there is no known treatment for AD once dementia set in, and with the increasing cost of care for AD, there is a growing interest in diagnosing subjects for possible AD conversion before clinical symptoms appear. Amyloid imaging using Positron Emission Tomography (PET) provides a non-invasive, in-vivo diagnosis of subjects based on cerebral amyloid load. In developing successful amyloid radiotracers to diagnose the amyloid burden in subjects, many challenges to consider (e.g. poor in-vitro to in-vivo conversion, different Aβ and tau binding etc.). To facilitate decision making in moving candidate amyloid radiotracers to clinical application, a screening methodology of amyloid PET radiotracers based on in-silico data and a biomathematical model was developed by the authors.

The biomathematical model developed was based on a 1-tissue compartment model developed by Guo et al. for CNS tracers[2)]. Two in-vitro pharmacological parameters, free fraction in plasma (f_P) and free fraction in tissue (f_{ND}) are required to generate kinetic parameters for *SUVR* simulations. However, f_P values of only three amyloid radiotracers were reported in literatures and were measured using either rat or monkey plasma (Table 1). We proposed a methodology based on in-silico lipophilicity values and a relational model[3)] to derive in-silico f_P and f_{ND} values. The purpose of this project was to validate the in-silico f_P values with in-vitro f_P values measured by means of ultrafiltration for 3 available amyloid

radiotracers in CYRIC, Tohoku University – [^{11}C]BF227, [^{11}C]PIB and [^{18}F]florbetapir.

Methods

Ultrafiltration

One tube of frozen human plasma samples (4 mL, with Heparin) was defrost at 37°C for 30 min in a pre-warmed incubator. Presence of triglycerides and plasma pH were checked[4]. 4 mL of PBS were pipetted into another storage tube and kept in the incubator for 30 min. For each tracer, 1% (F-18) or 5% (C-11) of the total volume of plasma sample (40 µL and 200 µL respectively), of radioactive compounds were pipetted into plasma and PBS storage tubes respectively. Both tubes were vortexed and incubated for 30 min at 37°C, with side-to-side tiling motion to ensure continuous mixing.

Radioactive plasma and PBS were pipetted into 3 Centrifree tubes (1 mL, 10 kDa MWCO, Millipore) each and centrifuged with sliding buckets at 2000 x g for 20 min at 37°C, using a temperature-controlled centrifugal machine (Kubota 2800, Japan)[5]. The Centrifree tubes of both plasma and PBS each, were weighted as a whole with their respective ultrafiltrate containers, before and after centrifugation to obtain the weight of the top plasma (W_{pti}) and bottom ultrafiltrate (W_{pfi}).

Fifteen empty gamma counter tubes were weighed. 100 µL of the plasma in the original storage tubes (C_{pi}), plasma in the top part of the Centrifree tubes (C_{pti}) and the respective ultrafiltrate (C_{pfi}) were pipetted into gamma counter tubes and radioactivity in each tube was measured using WIZARD2 (2480, Perkin Elmer) in three aliquots. The same procedures were repeated for PBS to obtain C_{bi}, and C_{bfi} only. For each tracer, f_P was measured using three aliquots to determine variability within each measurement and measurements were carried thrice to determine reproducibility of measurements.

Calculation of recovery, non-specific binding (NSB) & free fraction in plasma (f_P)

Due to NSB in ultrafiltration, a few methods were proposed to calculate f_P from ultrafiltration measurements, with basic method used as a standard[4]. However, it does not correct for NSB and hence a “reference” method was introduced to correct for NSB[6]. However, correcting f_P measurements using PBS was said to be inappropriate as PBS has different viscosity properties from plasma[7]. Moreover, ultrafiltration measurements were dependent on volume ratio of ultrafiltrate, hence a mass-balanced method[7] was introduced to correct for possible differences in measurements due to differences in volume ratio. The

various methods of determining f_P values were explored to compare with reported f_P values (Table 1).

A. Based on Mass-Balanced Method[7]:

Protein binding, recovery were calculated by mass balance as follows:

$$\%\text{Recovery} = \sum_{i}^{n}\left\{\frac{\left(C_{\text{pf}_i} \times W_{\text{pf}_i}\right) + \left(C_{\text{pt}_i} \times W_{\text{pt}_i}\right)}{\left(C_{\text{p}_i} \times W_{\text{p}_i}\right)}\right\} \times \frac{100\%}{n} \quad (1)$$

$$\%\text{NBS} = \sum_{i}^{n}\left\{1 - \frac{C_{\text{bf}_i}}{C_{\text{b}_i}}\right\} \times \frac{\mathbf{100}\%}{n} \quad (2)$$

$$f_P = \sum_{i}^{n}\left\{\frac{C_{\text{pf}_i} \times V_{\text{pf}_i}}{\left(C_{\text{pt}_i} \times V_{\text{pt}_i}\right) + \left(C_{\text{pf}_i} \times V_{\text{pf}_i}\right)}\right\} \times \frac{100\%}{n} \quad (3)$$

B. Based on Reference Method[6]:

$$f_P = \sum_{i}^{n}\left\{\frac{C_{\text{pf}_i}/C_{\text{p}_i}}{C_{\text{bf}_i}/C_{\text{b}_i}}\right\} \times \frac{100\%}{n} \quad (4)$$

C. Based on Basic Method[4]:

$$f_P = \frac{C_{\text{pf}_i}}{C_{\text{p}_i}} \times 100\% \quad (5)$$

where *i* refers to the no. of samples measured (n = 1 ~ 3), p refers to plasma and b refers to PBS (buffer), t refers to top part of Centrifree tube, f refers to the ultrafiltrate part of the Centrifree tube, without t or f means the total of both top and filtrate part of Centrifree tube. C refers to the radioactive concentration measured using WIZARD and W refers to the weight of the sample. For example, C_{pi} is radioactive concentration in plasma, W_{pi} is the weight of total weight of the samples in the top of the Centrifree tube and in the ultrafiltrate container, C_{ti} and W_{ti} are the radioactive concentration and weight of sample in the top of the Centrifree tube, C_{fi} and W_{fi} are the radioactive concentration and weight of the ultrafiltrate in the filtrate container.

Results

Table 2 shows the calculated recovery, NSB and f_P calculated by the 3 methods mentioned. The in-silico f_P values are also shown in Table 2.

Discussions

Up to date, very few literatures have reported the values of plasma free fraction (f_p),

(Table 1), and the equations used to calculate f_P were not discussed. f_P values were measured by means of thin layer chromatography and ultrafiltration and no f_{ND} values were reported in the literatures. f_P values measured using animals' (rat and monkey) plasma samples were used for measurements (Table 1), instead of human plasma samples, which made comparison of reported and measured f_P values (Table 2) difficult.

Equilibrium Dialysis is the gold standard used to measure both f_P and f_{ND} , but was not carried out due to limitations and long time required for measurement. Ultrafiltration was applied instead but measurements could only be used reliably if verified with ultrafilitration. However, non-specific binding (NSB) should be kept low (<5%)[4], and volume of ultrafiltrate should be kept controlled within 40% of total volume[4,5]. The average volume ratio of the ultrafiltrate is kept less than 20%, with an overall mean of 18.4% and standard deviation of 0.5%. The variabilities within experiment and between the experiments, were less than 5% regardless of the tracers used and the calculation methods applied (Table 2). Hence, the procedure parameters were well-controlled for f_P measurements.

[^{11}C]PIB had the highest NSB to filter membrane, followed by [^{11}C]BF227 then [^{18}F]florbetapir, with the same order for f_P values calculated using mass-balanced and basic methods. [^{11}C]BF227 has the highest referenced f_P values, followed by [^{11}C]PIB then [^{18}F]florbetapir. In-silico f_P values showed similar trend with reference f_P values.

Due to the binding nature of all three amyloid tracers measured, NSB values measured were always greater than 50% and %Recovery values measured were also less than 90%, hence ultrafiltration was not a suitable method for measuring f_P. Moreover, only three clinical amyloid radiotracers were available for f_P measurements hence it was difficult to use the f_P values for validating in-silico f_P values or for correlating with clinical outputs or for use in in-silico/in-vitro model prediction.

Conclusions

The results showed that ultrafiltration was not a suitable method for measuring f_P values. Although only three radiotracers were evaluated, the measured results showed a similar trend in terms of clinical tracer evaluation, whereby [^{11}C]PIB showed better amyloid binding then [^{11}C]BF227 and [^{18}F]florbetapir. If more clinical radiotracers were available, further evaluation on the possible co-relationships could be carried out.

References

1) Perrin RJ, Fagan AM, Holtzman DM, *Nature* **461** (2009) 916.
2) Guo Q, Brady M, Gunn RN, *J Nucl Med* **50** (2009) 1715.
3) Arakawa Y, Shidahara M, Nai YH, Furumoto S, Seki C, et al., OP162 EANM. (2015). (Harmburg, Germany: EANM 2015).
4) Dow N, In: Determination of compound binding to plasma proteins. Current protocols in Pharmacology (2006).
5) Kwong TC, *Clinica Chimica Acta* **151** (1985) 193.
6) Lee K-J, Mower R, Hollenbeck T, et al., *Pharmaceut Res* **20** (2003) 1015.
7) Wang C, Williams NS, *J Pharmaceut Biomed Anal* **75** (2013) 112.
8) Snellma, A, Rokka J, Lopez-Picon FR, et al., *Eur J Nucl Med Mol Imag* **39** (2012) 1784.
9) Seneca N, Cai L, Liow J-S, et al., *Nucl Med Biol* **34** (2007) 681.

Table 1. Free fraction in plasma (f_P) reported in Literatures.

Tracer	f_P (%)	Method of Measurement	Species	References
[^{11}C]PIB	14	Thin-layer Chromatography at 60 min	Rat	(8)
[^{18}F]Flutemetamol	1 (0.9–1.3)[#]	Ultrafiltration	Rat	(8)
[^{11}C]MeS-IMPY	0.83±0.17*	Ultrafiltration	Monkey	(9)

[#]Range of f_P values

*Mean ± Standard deviation

Table 2. Recovery, NSB, Plasma Free Fraction (f_P) and ultrafiltrate volume ratio measured using ultrafiltration (Mean ± Standard deviation) and in-silico f_p values (Right) for [^{11}C]PIB, [^{18}F]Florbetapir and [^{11}C]BF227.

Tracers	Recovery (%)	NSB (%)	Volume ratio (%)	Mass balanced f_P (%)	Referenced f_P (%)	Basic f_P (%)	In-Silico f_P (%)
[^{11}C]PIB	82.1±1.3	99.0±0.2	18.7±0.4	0.04±0.02	15.0±4.4	0.13±0.11	30.3
[^{18}F]Florbetapir	83.3±0.5	65.6±2.3	16.7±0.8	0.64±0.07	9.28±0.62	3.17±0.19	27.0
[^{11}C]BF227	81.7±1.5	94.7±0.3	18.1±0.5	0.19±0.01	16.2±0.7	0.84±0.03	30.4

VII. NUCLEAR MEDICINE

VII. 1. Longitudinal Assessment of Tau Pathology in Patients with Alzheimer's Disease Using [^{18}F]THK-5117 Positron Emission Tomography

Ishiki A.[1], Okamura N.[3], Furukawa K.[1*], Furumoto S.[2], Harada R.[1], Tomita N.[1], Hiraoka K.[2], Watanuki S.[2], Ishikawa Y.[2], Funaki Y.[2], Iwata R.[2], Tashiro M.[2], Yanai K.[2,3], Kudo Y.[1], and Arai H.[1]*

[1]*Institute of Development, Aging and Cancer, Tohoku University*
[2]*Cyclotron and Radioisotope Center, Tohoku University*
[3]*Tohoku University School of Medicine*

The formation of neurofibrillary tangle (NFT) is believed to contribute to the neurodegeneration observed in AD. Postmortem studies have shown strong associations between the neurofibrillary pathology and both neuronal loss and the severity of cognitive impairment. However, the temporal changes in the neurofibrillary pathology and its association with the progression of the disease are not well understood. Previously, we developed ^{18}F-labeled arylquinoline derivatives, including [^{18}F]THK-5117, as tau-selective PET tracers and succeeded in visualizing NFT pathology[2)]. The cross-sectional studies elucidated the differences in the spatial distribution of NFTs between patients with AD and healthy controls (HCs). Here, we performed a longitudinal PET study using the tau-selective PET tracer [^{18}F]THK-5117 in patients with AD and in HCs.

A total of 10 participants (five patients with AD and five HCs) participated in the studies. Participants were followed for 1.3 ± 0.2 years and then re-examined. PET imaging was performed using an Eminence STARGATE scanner (Shimadzu, Kyoto, Japan). After injecting 185 MBq of [^{18}F]THK-5117 or 296 MBq of [^{11}C]PiB, dynamic PET images were obtained for 90 min or 70 min, respectively. [^{18}F]THK-5117 PET images from 60 to 80 min post-injection were used for the following analysis. The PNEURO module in the PMOD software (version 3.6; PMOD Technologies, Zurich, Switzerland) was used to place and evaluate the volumes of interest (VOIs). VOIs were defined in the following regions:

---

[*] *Present address: Tohoku Medical and Pharmaceutical University*

hippocampus, parahippocampal gyrus, fusiform gyrus, middle and inferior temporal gyri, superior parietal cortex, lateral occipital cortex, and cerebellar cortex. The cerebellar gray matter was used as a reference region. The ratio of the regional SUV to the cerebellar cortex SUV (SUVR) was used as an index of tracer retention.

The demographic characteristics of the cohort are shown in Table 1. Significant differences between HCs and patients with AD were observed for the Mini Mental State Examination (MMSE) scores and Alzheimer's Disease Assessment Scale-cognitive subscale (ADAS-cog) scores at baseline. Cognitive testing showed a significant deterioration in the ADAS-cog score at follow-up compared to at baseline in the AD group. The annual change in the [^{18}F]THK-5117 retention in the HC and AD groups are shown in Table 2. The annual percent change in the [^{18}F]THK-5117 SUVR in HCs was within 2%. However, patients with AD showed significantly greater annual changes in [^{18}F]THK-5117 retention, in the middle and inferior temporal gyri (4.98 ± 3.92%) and in the fusiform gyrus (5.19 ± 2.01%). The relationship between the ADAS-cog score and the [^{18}F]THK-5117 SUVR in the middle and inferior temporal gyri is shown in Fig. 1A. HCs showed no remarkable changes in their ADAS-cog scores or in the [^{18}F]THK-5117 SUVR. In contrast, the three patients with moderate AD showed increased [^{18}F]THK-5117 retention compared to HCs and the two patients with mild AD. The annual change in the ADAS-cog score was significantly correlated with the annual change in the [^{18}F]THK-5117 SUVR in the middle and inferior temporal gyri ($r = 0.72$; $p = 0.019$) (Fig. 1B). Significant correlations were also observed in the fusiform gyrus, parahippocampal and ambient gyri, superior temporal gyrus, posterior temporal lobe, superior parietal gyrus, inferiolateral remainder of the parietal lobe, and lateral remainder of the occipital lobe.

In the present study, [^{18}F]THK-5117 was successfully used to visualize the pathologic time course of NFT formation in the human brain. These results suggest that the cognitive decline observed in patients with AD is attributable to the progression of neurofibrillary pathology. Longitudinal assessment of tau pathology will contribute to the assessment of disease progression and treatment efficacy.

References

1) Ishiki A, Okamura N, Furukawa K, Furumoto S, Harada R, et al., *PLoS One* **13** (2015) e0140311.
2) Harada R, Okamura N, Furumoto S, Furukawa K, Ishiki A, Tomita N, et al., *Eur J Nucl Med Mol Imag* **42** (2015) 1052.

Table 1. Demographic and clinical characteristics of the HCs and ADs.

Characteristics	HCs (n=5)	AD (n=5)
Age at baseline (years), mean±SD	71.6±4.2	80.4±13.1
MMSE at baseline	28.8±1.8	21.2±2.6
MMSE at follow-up	29.0±1.7	20.4±3.4
ADAS at baseline	5.1±2.2	19.0±5.1
ADAS at follow-up	4.2±1.5	21.4±5.9
Between PET exams (day)	519.4±45.0	426.4±1.8

Table 2. Annual rate of change in regional [^{18}F]THK-5117 retention ratio for HCs and ADs.

	% annual change of [^{18}F]THK-5117 SUVR	
Region, mean ± SD	Healthy control	Alzheimer's disease
Hippocampus	-0.10±1.95	2.55±4.46
Parahippocampal gyrus	1.23±0.82	3.93±3.18
Middle and inferior temporal gyrus	0.44±0.65	4.98±3.92†
Fusiform gyrus	0.85±1.75	5.19±2.01†
Superior parietal gyrus	-1.77±1.09	0.91±2.97
Lateral occipital gyrus	-1.09±1.11	3.02±1.97

† $p<0.05$ by analysis of variance followed by the Bonferroni's multiple comparison test.

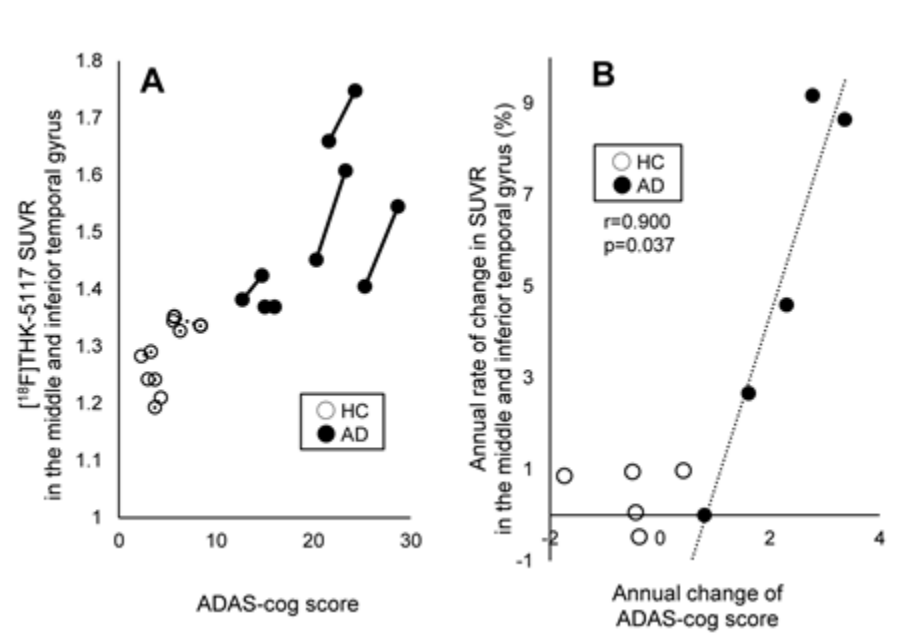

Figure 1. The relationship between the ADAS-cog score and [^{18}F]THK-5117 SUVR.

VII. 2. Enhanced [^{18}F]Fluorodeoxyglucose Accumulation in the Right Ventricular Free Wall Predicts Long-term Mortality of Patients with Pulmonary Hypertension

Tatebe S.[1], Fukumoto Y.[1], Oikawa-Wakayama M.[2], Sugimura K.[1], Satoh K.[1], Miura Y.[1], Aoki T.[1], Nochioka K.[1], Miura M.[1], Yamamoto S.[1], Tashiro M.[3], Kagaya Y.[1], and Shimokawa H.[1]

[1]*Tohoku University Graduate School of Medicine*
[2]*Japanese Red Cross Sendai Hospital, Sendai*
[3]*Cyclotron and Radioisotope Center, Tohoku University*

Background: We have previously demonstrated that [^{18}F]fluorodeoxyglucose (FDG) accumulation evaluated by ECG gated positron emission tomography (PET) is increased in the right ventricular (RV) free wall of patients with pulmonary hypertension (PH) and that this accumulation is ameliorated after medical therapy associated with hemodynamic improvement[1)]. However, it remains to be examined whether RV FDG accumulation has a prognostic significance in patients with PH.

Methods and Results: From March 2001 to June 2004, we performed gated FDG-PET in 27 patients with PH, including 18 with pulmonary arterial hypertension (PAH) and 9 with chronic thromboembolic pulmonary hypertension. We reviewed baseline clinical parameters, invasive hemodynamic data, and imaging data with cardiac MR, electron beam CT and FDG-PET quantified by calculating standardized uptake value (SUV) and corrected for partial volume effect based on the RV free wall thickness. We examined the relationship between baseline clinical parameters and the composite primary endpoint defined as all-cause mortality, lung transplantation, hospitalization for progression of PH and deterioration of WHO functional class and/or >15% reduction in 6-min walk distance (6MWD) from baseline, and all-cause mortality as the second endpoint. During the mean follow-up period of 69±49 [SD] months, 15 patients reached the composite primary endpoint, including all-cause mortality in 4, lung transplantation in 1, hospitalization for PH progression in 9, deterioration of WHO functional class and/or >15% reduction in 6MWD from baseline in 1 and death in 11 (41%). In FDG-PET measurements, corrected RV free

wall SUV was significantly increased in the endpoint group compared with the no endpoint group (10.1±2.7 vs. 7.6±2.2, P=0.02) (Fig. 1). Univariate COX hazard analysis showed that the corrected RV SUV of FDG was significantly correlated with the composite endpoint (hazard ratio 1.25, 95% confidence interval 1.04-1.51, P=0.02). This relationship remained significant even after adjustment for WHO functional class. In Kaplan-Meier analysis for the composite primary endpoint, patients with a corrected RV SUV ≥8.3 had a significantly poor prognosis compared with those with <8.3 (log-rank P=0.005 for the composite endpoint, P=0.07 for all-cause mortality) (Fig. 2).

Discussion: In this study we demonstrate that enhanced RV free wall SUV of FDG predicts long-term prognosis of PH patients. Regarding substrate metabolism, our previous study using autoradiography has demonstrated the shift in cardiac substrate utilization from fatty acids to glucose in pressure-overloaded rats[2)]. We also have demonstrated that myocardial glucose uptake was increased in the pressure-overloaded RV free wall in rats with constricted pulmonary artery[3)]. Furthermore, we demonstrated that FDG-uptake in the RV free wall was significantly increased in accordance with the severity of RV pressure overload in patients with PH[1)]. Thus, RV free wall SUV of FDG could become an early biomarker of RV metabolic dysfunction and make it possible to identify PH patients at a risk of poor prognosis.

Conclusions: These results indicate that enhanced FDG accumulation in the RV is a useful prognostic factor in patients with PH.

Acknowledgements

We thank Shoichi Watanuki for excellent technical support and Satoshi Miyata for support of the statistical analysis. This work was supported in part by the grants-in-aid from the Japanese Ministry of Education, Culture, Sports, Science, and Technology, Tokyo, Japan (Grant Number JP25461037).

This study was reported in “Eur Heart J Cardiovasc Imaging” in 2014[4)].

References

1) Oikawa M., et al., *J Am Coll Cardiol* **45** (2005) 1849.

2) Kagaya Y., et al., *Circulation* **81** (1990) 1353.
3) Otani H, et al., *Cardiovasc Res* **29** (1995) 763.
4) Tatebe S, Fukumoto Y, Sugimura K, et al., *Eur Heart J Cardiovasc Imag* **15** (2014) 666.

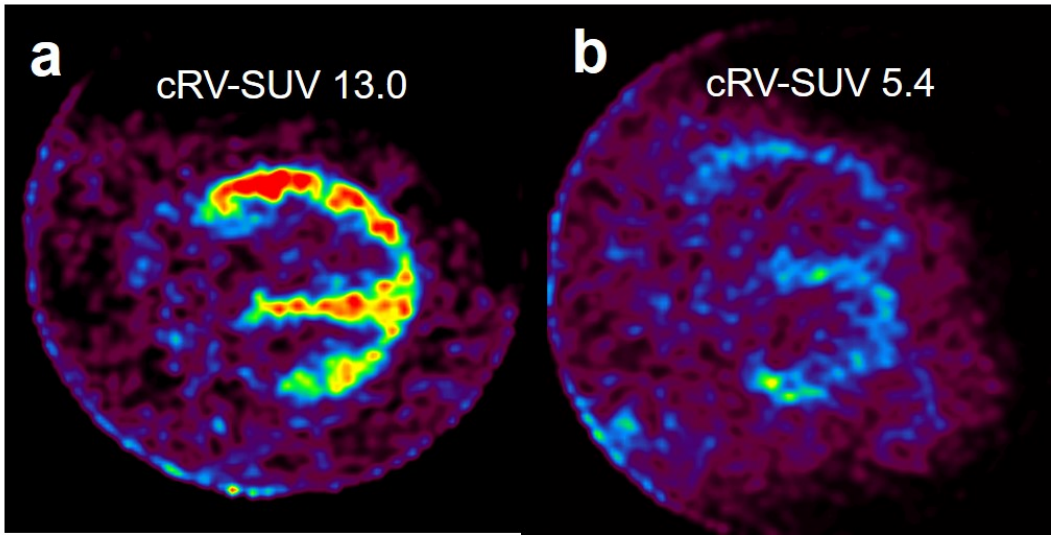

Figure 1. Evaluation of Right Ventricular Glucose Metabolism by FDG-PET in PH Patients
Representative FDG-PET image is shown in a patient with composite endpoint (a) and that without it (b). cRV = corrected right ventricular; SUV = standardized uptake value.

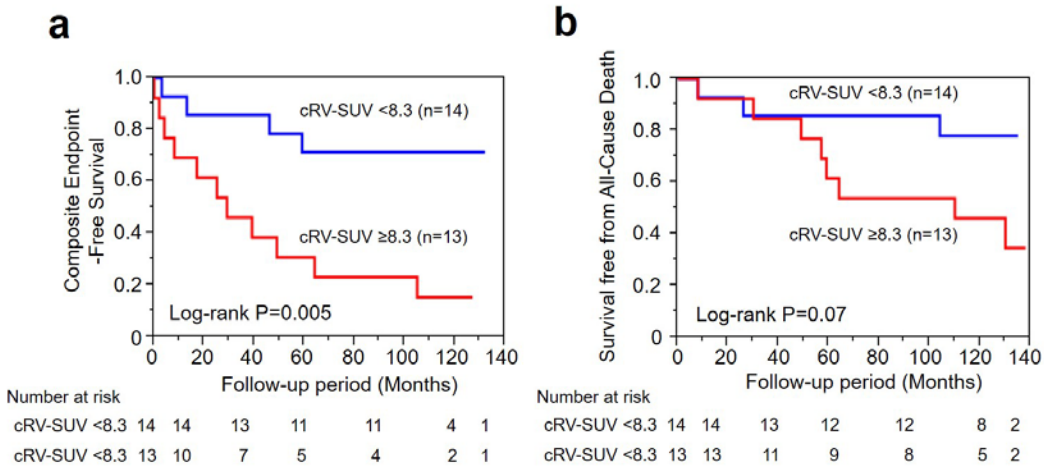

Figure 2. Prognostic Impact of Enhanced Right Ventricular Free Wall FDG Uptake in PH Patients
Kaplan-Meier curves shows that the cut-off level of cRV-SUV of 8.3 is useful to predict the long-term survival free from clinical worsening (a) and the long-term survival free from all-cause mortality (b) in PH patients. See Fig. 1 for abbreviations.

VII. 3. Brain Histamine H_1 Receptor Occupancy after Oral Administration of Levocetirizine: a PET Study

Hiraoka K.[1], Tashiro M.[1], Grobosch T.[2], Maurer M.[3], Oda K.[4], Toyohara J.[4], Ishii K.[4], Ishiwata K.[4], and Yanai K.[5]

[1]Cyclotron and Radioisotope Center, Tohoku University
[2]Labor Berlin - Charité Vivantes GmbH, Berlin
[3]Allergie-Centrum-Charité at the Charité - Universitätsmedizin Berlin, Berlin
[4]Tokyo Metropolitan Institute of Gerontology, Tokyo, Japan
[5]Tohoku University Graduate School of Medicine

Backgrounds

Histamine H_1 receptor (H_1R) antagonists, commonly known as antihistamines, are often used for treating allergic disorders. Their activity on brain H_1Rs leads to central side-effects such as sedation, which are caused by the blockade of the neural transmission of the histaminergic neurons. Levocetirizine is a new second-generation antihistamine. We measured the brain H_1R occupancy (H_1RO) by the drug using positron emission tomography (PET) and the subjective sleepiness after oral administration of the drug[1)].

Methods

Subjects and study design

The study was designed as a 3-arm, placebo-controlled crossover protocol in order to minimize potential errors due to inter-subject variability. Fexofenadine, a non-sedating antihistamine, was used as a negative active control. Eight healthy volunteers (mean ± SD; 23.1±2.9 years old) were enrolled in the study. PET imaging was performed at the Tokyo Metropolitan Institute of Gerontology, Tokyo, Japan.

PET procedures

The subjects underwent PET imaging after a single oral administration of levocetirizine (5 mg), fexofenadine (60 mg), or a lactobacteria preparation (6 mg) often used as placebo. The test medications and placebo were given at 9:30 a.m. on the study day in a blind manner. [^{11}C]Doxepin was injected 90 minutes after oral administration of the test

drugs or placebo. [^{11}C]Doxepin is a potent radiopharmaceutical developed for imaging H_1Rs in the brain. The injected dose [^{11}C]doxepin was 331±26 MBq (8.9±0.7 mCi). Sixty minutes after [^{11}C]doxepin injection, the subjects were positioned on the PET scanner (SET-2400W; Shimadzu, Kyoto, Japan) for transmission scanning (6 min) and emission scanning in the 3D mode for 15 min (70–85 min after [^{11}C]doxepin injection).

Assessment of subjective sleepiness

The subjective sleepiness of each subject was also measured before drug administration and 30, 60, 120, and 180 min post-administration using the Line Analogue Rating Scale and the Stanford Sleepiness Scale.

PET image analysis

The volumes of interest was defined in the neocortices. The cerebellum was defined as a reference region. As a parameter for the specific H_1R binding of [^{11}C]doxepin, we calculated the binding potential ratio (BPR) according to the following equation: (mean uptake value during the 15-min scan of the region ÷ mean uptake value during the 15-min scan of the cerebellum) − 1. H_1RO as a percentage of the placebo control was calculated using the following equation: (1 − BPR of antihistamine÷BPR of placebo)×100 (%).

Results

The mean BPR and H_1ROs of all neocortical regions are shown in Table 1. The BPRs were not significantly different in multiple comparisons with Bonferroni correction after ANOVA, indicating that both antihistamines have no potential to occupy brain H1Rs. The mean cortical H_1ROs following levocetirizine 5 mg and fexofenadine 60 mg administration were 8.1% (95% confidence interval, -9.8% to 26.0%) and −8.0% (95% confidence interval, -26.7% to 10.6%), respectively. During the 3 hours after drug administration, there was no statistical difference in subjective sleepiness between the three groups in the both tests (Fig. 1).

Discussion

The brain H_1RO of levocetirizine 5 mg is much lower than the previously reported H_1ROs of sedating antihistamines. The H_1RO findings were also confirmed by the subjective sleepiness results which were similar for all test groups; i.e. neither levocetirizine

5 mg nor fexofenadine 60 mg showed any potential to cause significant sedation when compared to placebo.

Conclusions

The H_1RO for levocetirizine 5 mg of 8.1% is well within the established range of less than 20% for non-sedating antihistamines. The result of this study shows that levocetirizine, when used in its recommended dose of 5 mg daily, does not penetrate the brain in large enough quantities to cause sedation.

Reference

1) Hiraoka K, Tashiro M, Grobosch T, Maurer M, Oda K, Toyohara J, et al., *Expert Opin Drug Saf* **14** (2015) 199.

Table 1. Binding potential ratios and histamine H_1 receptor occupancies.

	$BPR_{levocetirizine}$		$BPR_{fexofenadine}$		$BPR_{placebo}$		$H_1RO_{levocetirizine}$		$H_1RO_{fexofenadine}$	
	Mean	SD	Mean	SD	Mean	SD	Mean	SD	Mean	SD
Mean of all the neocortical regions	0.32	0.07	0.37	0.06	0.35	0.07	8.11	21.43	-8.02	22.30

$^{*}p<0.05$, paired *t*-test

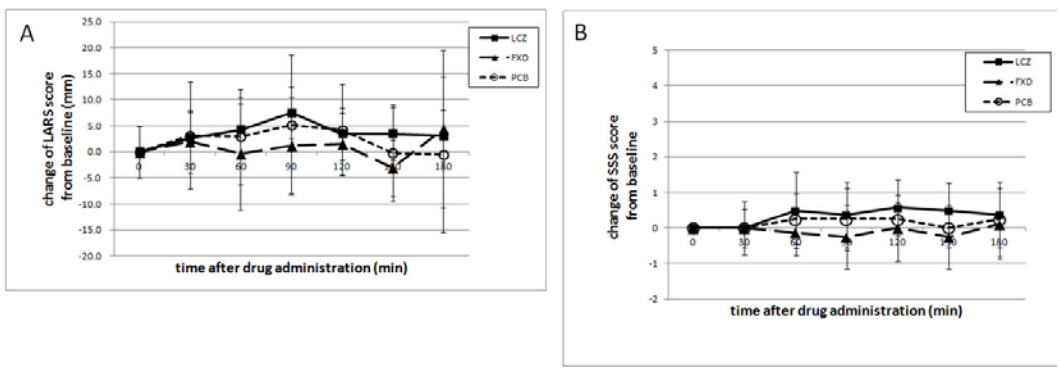

Figure 1. Subjective sleepiness, change from baseline over time, evaluated using the Line Analogue Rating Scale (LARS) (A) and the Stanford Sleepiness Scale (SSS) (B). Error bars represent standard deviations. LCZ, levocetirizine; FXD, fexofenadine; PCB, placebo.

VII. 4. Muscle Activity Pattern of the Shoulder External Rotators Differs in Adduction and Abduction: an Analysis Using Positron Emission Tomography

Kurokawa D.[1], Sano H.[1], Nagamoto H.[1], Omi R.[1], Shinozaki N.[1], Watanuki S.[2], Kishimoto K.N.[1], Yamamoto N.[1], Hiraoka K.[2], Tashiro M.[2], and Itoi E.[1]

[1]Tohoku University School of Medicine
[2]Cyclotron and Radioisotope, Tohoku University

To externally rotate the shoulder in abducted position is necessary for various activities of daily living, such as eating, shaking hands, combing, etc. The infraspinatus and teres minor are known to be the main external rotators of the shoulder. Although several authors investigated the difference in shoulder external rotation between abducted and adducted positions, the muscle activity pattern during shoulder external rotation has not been fully clarified. This study aimed to determine the activities involved in external rotation in adducted and abducted positions using positron emission tomography (PET).

Seven healthy volunteers without any history of shoulder pain or trauma were examined using PET in the present study. All participants were male and their dominant sides were right. Their average age was 33 years (range: 27-42). They underwent PET examinations after performing external rotation using an elastic band at both 0 degrees and 90 degrees of shoulder abduction in the frontal plane.

The FDG was dissolved in approximately 2 mL saline, which was then injected intravenously via the median cubital vein. The mean dose and the standard deviation of injected [^{18}F]fluoro-2-deoxyglucose (FDG) were 75.7 and 3.1 MBq, respectively. As for the external rotation exercise at 0 degrees of abduction, the exercise protocol consisted of repetitive shoulder external rotation in the supine position with the arm at the side. In each exercise, the shoulder was rotated from 30 degrees of internal rotation to 30 degrees of external rotation with a resistance using an elastic band (Thera-Band® Yellow, The Hygenic Corporation, Ohio, USA). The repetition number of exercise was 100 times before FDG injection and 200 times after the injection. PET images were collected 50 min after the

injection with a whole-body positron camera (SET-2400W; Shimadzu Inc., Kyoto, Japan). For each subject, PET scan was repeated two more times on separate days to obtain the data of external rotation exercise at 90 degrees of abduction as well as that of a resting condition (without any exercises).

Each PET image was fused to the corresponding MR image at the identical level using a software Dr. View/LINUX (AJS Inc., Tokyo, Japan) according to the methods reported in our previous paper by Omi et al.[1)], which enabled to delineate the contour of each shoulder muscle. Each PET image was fused to the corresponding MR image to identify each shoulder muscle. Subsequently, the volume of interest (VOI) was placed on the MR image for each shoulder muscle. Then, the standardized uptake values (SUVs) in each segment of the shoulder muscles were calculated to quantify their activities. Following this, we performed the following comparisons. First, the exercise/rest ratio of SUV was compared among five muscles both for 0 degrees and 90 degrees of abduction to clarify which muscle was most activated through the external rotation exercise. Second, TMi/ISP ratio of SUV (TMi: teres minor, ISP: infraspinatus) was established to determine the relative contribution of these two muscles to the external rotation exercise. Then, this ratio was compared at 0 degrees and 90 degrees of abduction.

A high FDG uptake was observed in all 4 rotator cuff muscles after external rotation exercise both in adduction and in abduction (Fig. 1). The infraspinatus showed the greatest muscle activity during external rotation at 0 degrees of abduction, whereas the teres minor showed the greatest activity at 90 degrees of abduction. The teres minor/infraspinatus ratio at 90 degrees of abduction (1.21±0.23; mean±standard deviation) was significantly higher than that at 0 degrees of abduction (0.84±0.15) ($P<0.01$).

The infraspinatus and teres minor are the main shoulder external rotators. The teres minor is more important as an external rotator in abduction than in adduction, as already published[2)].

References

1) Omi R, Sano H, Tashiro M, Itoi E, et al. *J Anat* **216** (2010) 643.
2) Kurokawa D, Sano H, Nagamoto H, Omi R, Shinozaki N, Watanuki S, Kishimoto KN, Yamamoto N, Hiraoka K, Tashiro M, Itoi E. *J Shoulder Elbow Surg* **23** (2014) 658.

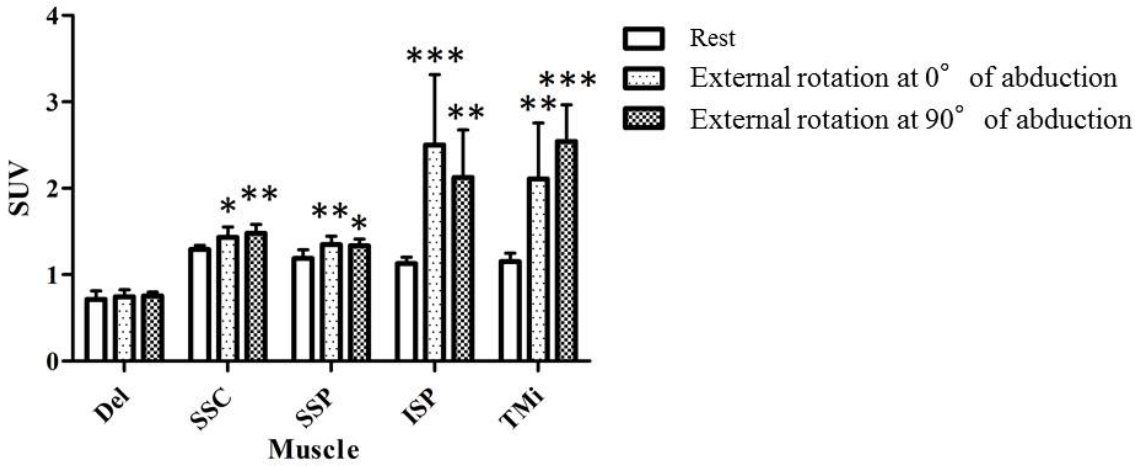

Figure 1. The mean standardized uptake value (SUV) for each shoulder girdle muscle.
Del: deltoid, SSC: subscapularis, SSP: supraspinatus, ISP: infraspinatus, TMi: teres minor. Statistically significant increase compared to at rest (*P<0.05, **P<0.01, ***P<0.001).

VII. 5. Brain Accumulation of Amyloid Protein Visualized by PET and BF-227 in Alzheimer's Disease Patients with or without Diabetes Mellitus

Tomita N.[1], Furukawa K.[1], Okamura N.[2], Tashiro T.[3], Une K.[1], Furumoto S.[3], Iwata R.[3], Yanai K.[2,3], Kudo Y.[1], and Arai H.[1]

[1]Institute of Development, Aging and Cancer, Tohoku University,
[2]Tohoku University Graduate School of Medicine
[3]Cyclotron and Radioisotope Center, Tohoku University

Although diabetes mellitus (DM) is considered to be one of the most consistent risks for developing dementia, it is not known if the pathology in dementia patients with DM is similar to or distinct from typical pathological features of Alzheimer's disease (AD)[1-5]. Several different pathways are important in the pathophysiology of AD, either indirectly, through inflammation or the development of vascular disease, or directly, through effects on amyloid and tau metabolism and the formation of advanced glycation end products(AGEs)[6] (Fig. 1). To find out the mechanism of developing dementia in AD patients with DM in a living state, we studied the distribution of amyloid beta (Aß) protein of the diabetic AD patients.

To evaluate the accumulation of Aß we examined 14 normal controls, 4 diabetic patients with AD and 11 non-diabetic patients with AD by positron emission tomography (PET) using BF-227, a currently developed Aß tracer[7].

Clinical features of the three groups, NC, AD alone, and AD with DM, are described in Table 1. Severities of dementia assessed by MMSE are not significantly different between AD alone and AD with DM. Three patients were treated with only oral DM medications (Patient A: glimepiride + pioglitazone, Patient B: glimepiride + metformin + voglibose, Patient C: metformin + voglibose), whereas only 1 AD with DM patient used insulin in addition to metformin. One DM patient was present in the normal control group. This patient in control group had no oral medication. Insulin injection was the only medication.

Magnetic resonance imaging (MRI) scans revealed none or very little ischemic or hemorrhagic lesions observed in any of the subjects (data not shown).

After we obtained demographic information, we analyzed PET images with BF-227

among the three groups, and representative brain PET images are shown in Fig. 2. As indicated in the figure, both the subjects with AD alone and AD with DM showed significantly more robust retention of BF-227 than NCs. Statistical analysis revealed a significantly higher SUV-R of BF-227 ($P<0.05$) in the cerebral cortex of AD alone and AD with DM than NC as shown in Fig 3. Neocortical SUV-R of BF-227 in AD alone and AD with DM are not significantly different. Both the cases with AD alone and AD with DM showed increased BF-227 uptake in frontal, temporal, parietal, occipital and cingulated gyrus. The pattern of uptake was similar between the DM patients with insulin use and those without the use of insulin (Fig. 2). A similar pattern of uptake between insulin user and non-insulin user was seen both in the control group and the AD with DM group.

The analysis of PET images among the three groups revealed an abundant aggregated Aß accumulation in the cerebral cortex of both AD patients with and without DM. The extent and distributions of BF-227 accumulation in diabetic AD patients were not significantly different from these of non-diabetic AD patients. These results suggest that the degree and extent of Aß metabolism is not much different between AD with DM and AD alone.

References

1) Biessels GJ, et al., *Lancet Neurol* **5** (2006) 64.
2) Schrijvers EM, et al., *Neurol* **75** (2010) 1982.
3) Whitmer RA, et al., *Jama* **301** (2009) 1565.
4) Beeri MS, et al., *J Gerontol A Biol Sci Med Sci* **60** (2005) 471.
5) Matsuzaki T, et al., *Neurol* **75 (**2010) 764.
6) Sims-Robinson C, et al., *Nat Rev Neurol* **6**(2010) 551-9.
7) Kudo Y, et al., *J Nucl Med* **48** (2007) 553.

Table 1. Clinical features of the three groups, NC, AD alone, and AD with DM.

	Diagnostic group		
	Normal Control	AD alone	AD with DM
N	14	11	4
Gender (Male/ Female)	7 / 7	4 / 7	2 / 2
Age	64.5 ± 2.9	78.5 ± 3.9	77.5 ± 5.2
MMSE	29.9 ± 0.1	20.5 ± 0.8	19.4 ± 2.8
ApoE ε4 allele (%)	0.12	0.35	0.37
HbA1c (%)	5.7 ± 0.1	5.8 ± 0.1	7.2 ± 0.4

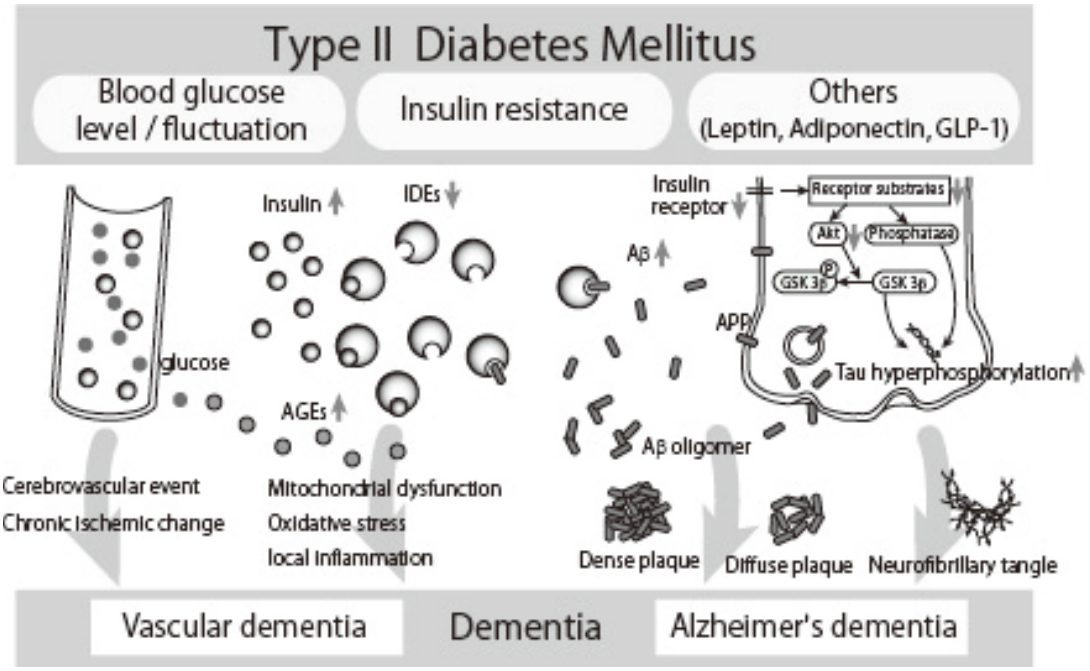

Figure 1. The possible pathological mechanisms associated with the impact of type 2 DM on the central nervous system (CNS). The major components of DM were described in the second column (we described only the three major components for easier understanding, though several other components were mentioned.) Just below the column, the possible mechanism of developing dementia in type 2 DM. (Abbreviation) IDEs: Insulin degrading enzymes, AGEs: advanced glycation end products, A: amyloid beta protein, APP: amyloid precursor protein, GSK-3: glycogen synthase kinase 3, GLP-1: glucagon like peptide-1.

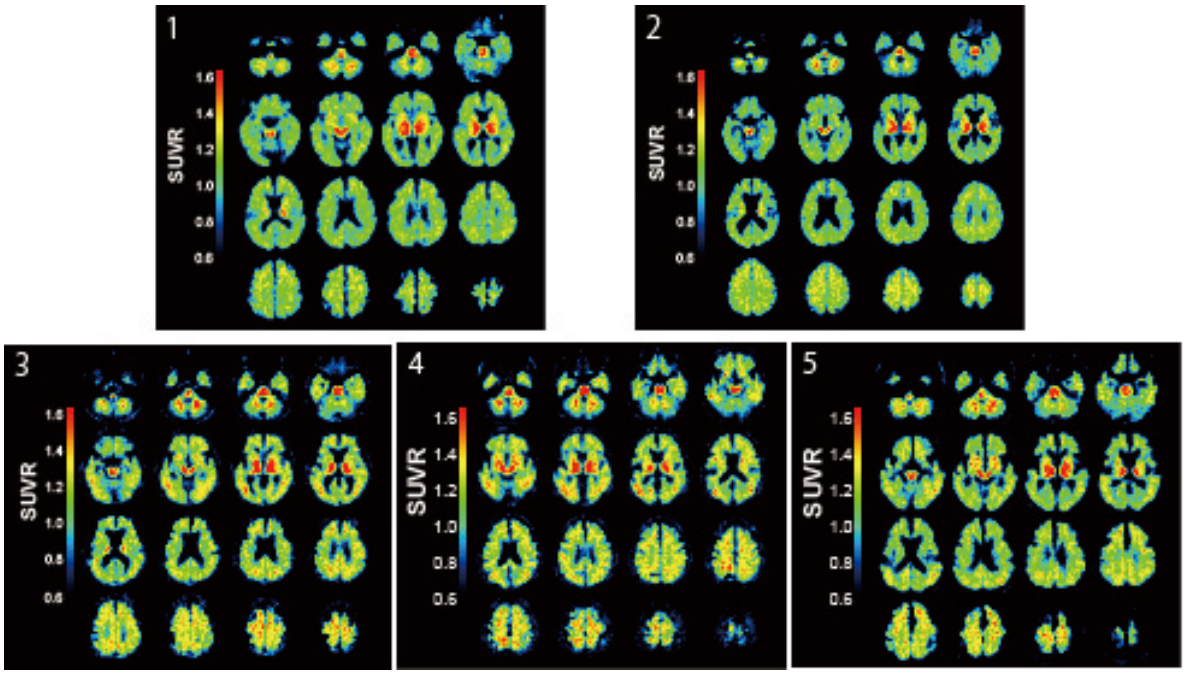

Figure 2. Representative BF-227 PET images of each diagnostic group. 1: Normal control without DM (67 years old, male, no complication; Neocortical SUVR=1.122), 2: Normal control with diabetes mellitus (67 years old, female, insulin user; Neocortical SUVR=1.012), 3: AD alone (75 years old, female; Neocortical SUVR=1.230), 4: AD with DM (79 years old, female, insulin user; Neocortical SUVR=1.240), 5: AD with DM (78 years old, male, non-insulin user; SUVR=1.18).

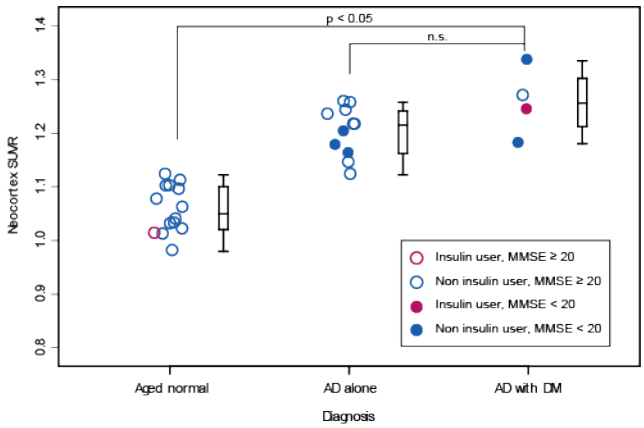

Figure 3. Box and scatter plots of SUVR values with BF-227 in Aged Normal, AD alone and AD with DM. Each circle indicates the mean SUVR from the mean neocorex. Red colored circle represents insulin user, while blue colored circle represents non-insulin user. Filled circle represents the subjects with MMSE score less than 20. Although both AD with DM and AD alone showed significantly higher SUVR than NC ($P<0.05$), difference between AD with DM and AD alone was not significant (n.s.).

VII. 6. A Simulated Car-driving Performance on the Effects of Administration of Levocetirizine, Fexofenadine, and Diphenhydramine in Healthy Japanese Volunteers

Inami A.[1,2], Matsuda R.[1], Grobosch T.[3], Komamura H.[1], Yamada Y.[1], Ito T.[1], Koike D.[1], Takeda K.[1], Miyake M.[1], Hiraoka K.[1], Maurer M.[3], Yanai K.[1,2], and Tashiro M.[1]

[1]Cyclotron and Radioisotope Center, Tohoku University
[2]Tohoku University Graduate School of Medicine
[3]Allergie-Centrum-Charité/ECARF, Charité-Universitätsmedizin, Berlin

Introduction

Histamine H1 receptor (H1R) antagonists, known as antihistamines, have sedative side effects, which are caused by the block of H1R in brain. First-generation antihistamines such as diphenhydramine (DIP) can easily cross the blood-brain barrier (BBB), and they are known to cause strong sedation. The second-generation antihistamines, such as cetirizine, loratadine, and ebastine, may cause little or mild impairment of performance compared with the first-generation antihistamines[1)]. Levocetirizine (LEV) has a high affinity and selectivity for H1R, and it has been reported to show little sedation as well as fexofenadine (FEX)[2)]. However, our previous [^{11}C]doxepin PET study revealed that H1R occupancy of LEV 5mg administration was 8.1%. For elderly patients aged ≥65 years, the US label recommends starting at lower dosages. We performed the examination using a driving simulator to young and elderly groups in order to determine the effect of LEV on driving performance. Here, we report the results of our early analysis on young group.

Materials and Methods

Twenty healthy volunteers (11 men and 9 women) participated in and completed the study. Their mean age and standard deviation was 26.7±5.9 years (men: 25.8±4.7 years; women: 27.7±7.4 years). This study uses a double-blind, placebo-controlled, four-way, crossover design. Single doses of LEV 5 mg, FEX 60 mg, DIP 50 mg, and placebo (PLA) were administered orally with 100 mL water. Driving tests were performed before oral administration (baseline: Driving 1) and at 90 min (Driving 2) and 180 min (Driving 3) post-

administration (Fig. 1) The primary assessment was the driving test, including brake reaction time, lateral stability, and the multiple task, and the secondary assessment was subjective sedation. Subjective sedation was measured prior to and immediately after the driving test at each time point (six times in each test). All subjects performed a simple brake reaction time (SBRT) test, a choice brake reaction time test (CBRT), a lateral tracking (LT) test, and multiple test, using a commercially available simulator (DS-3000, Mitsubishi Precision Ltd., Tokyo, Japan) (Fig. 2). During the SBRT and CBRT, the mean brake reaction time was calculated. In the LT test, the object of the test was to steer an image of a car hood down the center of a winding road as accurately as possible using a steering wheel, and the ability to track continuously was measured. The mean deviation from the center of the lane was calculated as a percentage, taking the deviation to either edge of the lane as 100%. Subjects were also asked to perform the CBRT and the LT tests a second time, as part of a multiple test whose results were analyzed independently of the relevant single tests. The results of the multiple test were calculated separately as the tracking error (mean deviation from the center of the road) and brake reaction time.

The Stanford Sleepiness Scale (SSS) is a seven-point self-report measure of how alert an individual feels, with proven sensitivity in a number of studies. Subjects may indicate feeling active, vital, alert, wide awake, somewhat foggy, sleepy, or asleep. The higher the score, the less alert and more drowsy the subject felt. The line analog rating scale (LARS) is a measure of the subjective effects of psychoactive drugs and has been used to detect sedation in response to many different classes of compounds. Subjects were asked to mark a series of 100-mm line analog scales, indicating their present state of mind. This score was compared with a midpoint that represented their pretreatment state of mind. Mean ratings of drowsiness and alertness were taken as a measurement of perceived sedation. The higher the score, the less alert and more drowsy the subject felt. Plasma concentration of levocetirizine, fexofenadine and diphenhydramine were determined by high performance liquid chromatography and mass spectrometry as we noted in detail on our published paper[3].

For the statistical analyses of subjective sedation, the SSS and LARS scores were examined using the Friedman test. Significant findings were additionally examined by post hoc multiple pairwise treatment comparisons using a Wilcoxon signed rank test (two-tailed; $p \leq 0.05$). Brake reaction time data were examined using repeated measures analysis of variance with factors for LEV, FEX, DIP, and PLA. Significant findings were further examined by post hoc Bonferroni testing in order to examine differences between two drug

conditions (two-tailed; $p \leq 0.05$). For the LT test data, a nonparametric Friedman test was applied. Significant findings were further examined by multiple post hoc pairwise Wilcoxon signed rank tests in order to examine differences between two drug conditions (two-tailed; $p \leq 0.05$)

Results and Discussion

No significant treatment effect was detected for the mean brake reaction time and accuracy in SBRT and CBRT, as well as in the CBRT component of the multiple tests. A significant main effect was found for mean deviation in the LT test when the Friedman test was applied to the 90 and 180 min post-administration data sets ($p<0.001$ and $p=0.003$, respectively). A post hoc Wilcoxon signed rank test revealed that the mean deviation value after PLA treatment was significantly smaller than after DIP both at 90 and 180 min post-administration ($p<0.001$) (Fig. 3). In addition, at 90 min ($p=0.001$) and 180 min ($p=0.037$), the mean deviation values after LEV treatment were significantly smaller than those after DIP treatment (Fig.3). At 90 min ($p=0.001$) and 180 min ($p=0.004$), the mean deviation values after FEX treatment were also significantly smaller than those after DIP treatment (Fig. 3). A significant effect was found for the mean deviation in the LT test component of the multiple task when a Friedman test was applied to the 90 min ($p=0.011$) and 180 min ($p=0.044$) post-administration data sets. A post hoc Wilcoxon signed rank test revealed that the mean deviation value after PLA treatment was significantly smaller than that for DIP at 90 min ($p=0.006$) post-administration (Fig. 4). In addition, at 90 min ($p=0.017$) and 180 min ($p=0.03$), the mean deviation values after LEV treatment were significantly smaller than those after DIP treatment (Fig.4). At 90 min ($p=0.017$) and 180 min ($p=0.03$), the mean deviation values after FEX treatment were also significantly smaller than those after DIP treatment (Fig.4). SSS and LARS showed similar results (Fig. 5). Post hoc tests revealed that subjects given DIP felt significantly more sedated compared with those given LEV, FEX, or a PLA at 90 and 180 min post-administration (Fig. 5). The mean plasma concentrations (ng/mL) ± standard deviation at 90 and 180 min post-administration, respectively, were levocetirizine 171.2±46.0, 156.3±30.3; fexofenadine 165.4±62.1, 137.8±42.8; and diphenhydramine 48.2±31.7, 69.8±22.9. The peak plasma concentrations were achieved for levocetirizine and fexofenadine at around 90 min post-administraion, whereas the peak plasma concentration of diphenhydramine was achieved at a later time point[3)]. These results are not consistent with the prescribing information, and there was no particular abnormality.

The results indicated no significant impairment in the car-driving test parameters after oral administration of an acute dose of LEV 5 mg. Verster et al. in healthy volunteers, in which the standard deviation of lateral position after LEV 5 mg was equivalent with that of the PLA[4]. These results suggest that it is safe to drive a car when taking LEV 5 mg once daily. The present results seem to agree with a recent meta-analysis using the proportional impairment ratio (PIR), where the PIRs for both objective and subjective measures were 0.0 for LEV, while those with cetirizine were 6.38 for the subjective measure and 1.31 for the objective measure[5]. In the present study, DIP significantly impaired car-driving ability, demonstrating that the sensitivity of our driving test was sufficient. Statistical examination showed that the LT results after DIP treatment were significantly different from those after PLA treatment. The subjective assessment was also consistent with the objective findings of the significant impairment of car-driving performance, especially for LT. The observed pattern was that the LT test was more sensitive than reaction time tests under the influence of sedative antihistamine.

Conclusion

The findings of the present and previous car-driving studies suggest that it is safe to drive a car when taking LEV 5 mg once daily. Our results show that after acute oral administration of LEV 5 mg, performance in the car-driving test was not significantly affected in healthy Japanese volunteers. In addition, people using sedative antihistamines, such as DIP, should be warned against driving, because our results clearly show the impairment of LT.

Acknowledgements

This study was supported by an unrestricted research grant from GlaxoSmith Kline. Further support was provided by the Japan Foundation for Clinical Pharmacology.

References

1) Verster JC, Volkerts ER, *Ann Allergy Asthma Immunol* **92** (2004) 294.
2) Devillier P, Roch N, and Faisy C, *Clin Pharmacokinet* **47** (2008) 217.
3) Inami A, Matsuda R, Grobosch T, et al., *Hum Psychopharmacol* **31** (2016) 167.
4) Verster JC, de Weert AM, et al., *Psychopharmacology (Berl)* **169** (2003b) 84.
5) Isomura T, Kono T, Hindmarch I, et al., *PLoS One* **9** (2014) e114336.

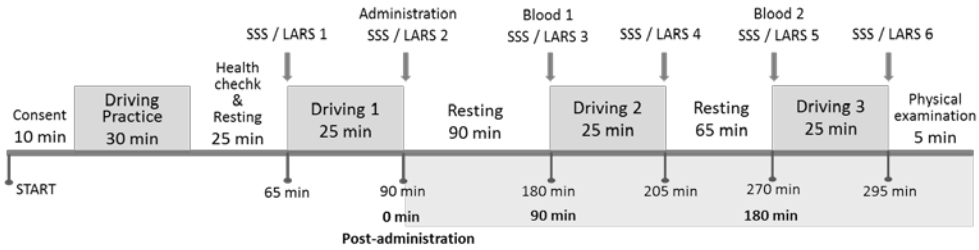

Figure 1. Schematic diagram of the study protocol (reproduced from Ref. 3).

Figure 2. Car-driving simulator (DS-3000, Mitsubishi Precision Ltd).

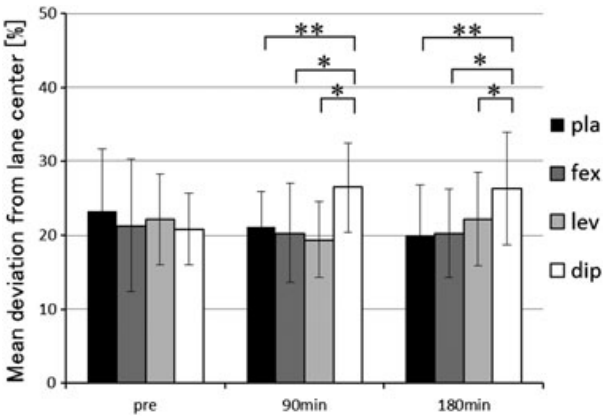

Figure 3. Lateral tracking test results showing the mean deviation from the center of the lane. Values are means (%), and standard deviation is shown by the error bars. *p<0.05, **p<0.001 for the *post hoc* Wilcoxon signed rank test. Pla: placebo, Fex: fexofenadine, Lev: levocetirizine, Dip: diphenhydramine (reproduced from Ref. 3).

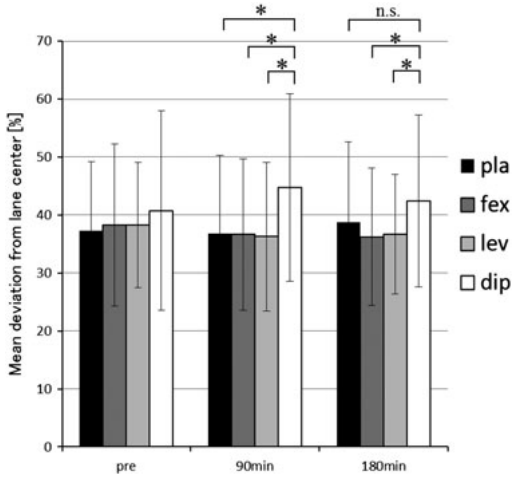

Figure 4. Results of the lateral tracking test component of the multiple task. Values are mean deviation (%), and standard deviation is illustrated by the error bars. *p<0.05, **p<0.001 for the *post hoc* Wilcoxon signed rank test. Pla: placebo, Fex: fexofenadine, Lev: levocetirizine, Dip: diphenhydramine (reproduced from Ref. 3).

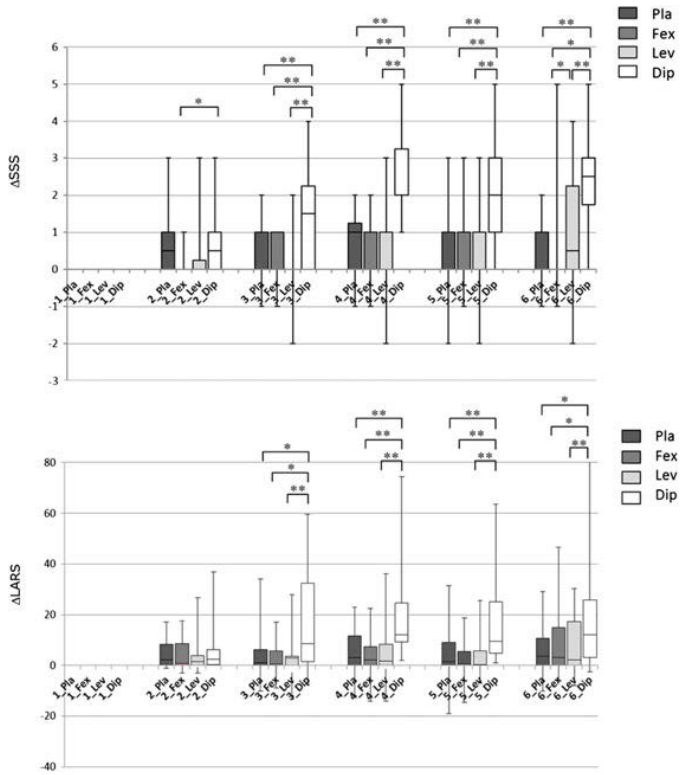

Figure 5. Box plot of subjective sedation measured by the Stanford Sleepiness Scale (SSS) and line analog rating scale (LARS). *p<0.05, **p<0.001 for the *post hoc* Wilcoxon signed rank test. Pla: placebo, Fex: fexofenadine, Lev: levocetirizine, Dip: diphenhydramine (reproduced from Ref. 3).

VIII. RADIATION PROTECTION AND TRAINING OF SAFETY HANDLING

VIII. 1. Beginners Training for Safe Handling of Radiation and Radioisotopes at Tohoku University

Watabe H., Ohtomo K., Mayama F., Tojo I., Miyake Y., and Yuki H.

Cyclotron and Radioisotope Center, Tohoku University

This report summarizes the beginners training for safe handling of radiation and radioisotopes at Tohoku University from 2014 to 2015. Twice a year (in May and in November), we organize three educational courses including lectures and practices, namely 1) Radiation and Isotopes, 2) X-ray Machines and Electron Microscope, and 3) Synchrotron Radiation (SOR). Since November 2002, we have also organized lectures in English for students or researchers who are not familiar with Japanese language. The training was held twice a year, in May and November under the help for lectures and practice from various departments and research institutes of the university.

The training for "Radiation and Radioisotopes" is for persons who use unshielded radioisotopes and accelerators, and has been conducted from 1977. The contents of lectures and practices are shown in Table 1. The departments or institutes to which trainees belong and the distributions of trainees are shown in Table 2 and Table 3.

The training for "X-ray machines and electron microscopes" started at the end of 1983. The training is scheduled at the same time as that for "Radiation and Radioisotopes". In this course, only lectures are given with no practice. The contents of lectures are shown in Table 4. The departments or institutes to which trainees belong and the distributions of trainees are shown in Table 5 and Table 6.

The training for "Synchrotron Radiation" began at the end of 1995. The contents of the lectures are the same as those of the "Radiation and Radioisotopes" but no practice. The departments or institutes to which trainees belong and the distributions of trainees are shown in Table 7 and Table 8.

Table 1. Contents of the lectures and practices for "Radiation and Radioisotopes" in 2014 and 2015.

Lectures (one day)	Hours
Introduction to radiation	0.5
Effects of radiation on human	1.0
Radiation physics and measurements	1.0
Chemistry of radioisotopes	1.0
Radiological protection ordinance including video	1.5
Safe handling of radioisotopes	1.5

Practices (one day)	Hours
Treatment of unsealed radioactive solution	4.0
Measurement of surface contamination and decontamination	1.0
Measurement of gamma-rays and beta-rays	2.0

Table 2. Distribution of trainees for “Radiation and Radioisotopes” in 2014.

Department	Staff	Student	Total	English class
CYRIC	1	4	5	1
Medicine	9	31	40	2
Dentistry	0	3	3	1
Pharmacy	2	44	46	0
Science	5	75	80	5
Engineering	10	117	127	8
Agriculture	2	47	49	1
Research Institutes	18	44	62	5
The others	0	0	0	0
Total	47	365	412	23

Table 3. Distribution of trainees for “Radiation and Radioisotopes” in 2015.

Department	Staff	Student	Total	English class
CYRIC	1	7	8	5
Medicine	14	48	62	2
Dentistry	0	10	10	1
Pharmacy	1	40	41	0
Science	4	88	92	3
Engineering	4	123	127	9
Agriculture	0	35	35	1
Research Institutes	12	44	56	13
The others	0	0	0	0
Total	36	395	431	34

Table 4. Contents of the lectures for “X-ray machines and Electron microscopes” in 2014 and 2015.

Lectures (one day)	Hours
Safe handling of X-ray machines	1.5
Radiological protection ordinance	0.5
Video for safe handling of radiation and radioisotopes	0.5

Table 5. Distribution of trainees for “X-ray machines and Electron microscopes” in 2014.

Department	Staff	Student	Total	English class
CYRIC	0	0	0	0
Medicine	7	1	8	0
Dentistry	3	5	8	0
Pharmacy	0	2	2	0
Science	1	29	30	1
Engineering	14	210	224	14
Agriculture	0	0	0	0
Research Institutes	29	46	75	15
The others	0	0	0	0
Total	54	293	347	30

Table 6. Distribution of trainees for “X-ray machines and Electron microscopes” in 2015.

Department	Staff	Student	Total	English class
CYRIC	0	0	0	0
Medicine	1	2	3	1
Dentistry	4	8	12	2
Pharmacy	1	2	3	0
Science	1	28	29	3
Engineering	16	217	233	26
Agriculture	0	0	0	0
Research Institutes	22	41	63	19
The others	0	0	0	0
Total	45	298	343	51

Table 7. Distribution of trainees for “Synchrotron radiation” in 2014.

Department	Staff	Student	Total	English class
CYRIC	0	0	0	0
Medicine	0	1	1	0
Dentistry	0	0	0	0
Pharmacy	0	0	0	0
Science	1	11	12	13
Engineering	3	51	54	5
Agriculture	0	0	0	0
Research Institutes	8	38	46	13
The others	0	0	0	0
Total	12	101	113	31

Table 8. Distribution of trainees for “Synchrotron radiation” in 2015.

Department	Staff	Student	Total	English class
CYRIC	1	0	1	0
Medicine	0	0	0	0
Dentistry	0	0	0	0
Pharmacy	0	0	0	0
Science	2	10	12	0
Engineering	6	56	62	10
Agriculture	0	0	0	0
Research Institutes	9	35	44	8
The others	0	0	0	0
Total	18	101	119	18

VIII. 2. Radiation Protection and Management

Yuki H.[1], Ohtomo K.[1], Watabe H.[1], and Nakae H.[2]

[1]Cyclotron and Radioisotope Center, Tohoku University
[2]Japan Environment Research Co., Ltd.

(1) Overview

During the fiscal year of 2014 and 2015, research and education in the center were conducted as active as usual.

(2) Unsealed radionuclides used in CYRIC

The species and amounts of the four most used unsealed radionuclides during the fiscal year of 2014 and 2015 are listed in Table 1. The table includes the isotopes produced by the cyclotron as well as those purchased from the Japan Radioisotope Association or taken over from other radioisotope institutes.

(3) Radiation exposure dose of individual worker

The exposure doses of the workers in CYRIC during 2014 and 2015 are given in Table 2. The doses were sufficiently lower than the legal dose limits.

(4) Radiation monitoring of the workplace

Radiation dose rates inside and outside of the controlled areas in CYRIC were monitored periodically and occasionally when needed. They were generally below the legal dose limits although there are several “hot spots” in mSv/hr range like slits or beam stopper of the 930 cyclotron and so on. Surface contamination levels of the floors inside the controlled areas were also measured with a smear method and a survey meter method. They were under the legal regulation levels.

(5) Wastes management

The radioactive wastes were delivered to the Japan Radioisotope Association in the

fiscal year of 2014 and 2015.

The concentration of radioisotopes in the air released from the stack after filtration was monitored with stack gas monitors. The values of concentration were well below the legal regulation levels. The radioactive water was stocked in the tanks at least for 3 days and then released to the sewerage after confirming that the concentration was lower than the legal regulation levels.

Table 1. The four most used unsealed radioisotopes used in CYRIC during the fiscal year of 2014 and 2015.

	2014	2015
C-11	373.41 GBq	528.42 GBq
O-15	0 GBq*	8.9340 GBq
F-18	755.13 GBq	1.1814 TBq
P-32	1.1193 GBq	1.9031 GBq

*The PET scanner for O-15 was not used because of repairing the building.

Table 2. Occupational radiation exposures in CYRIC during the fiscal year of 2014 and 2015.

Dose range (mSv)	Number of individuals	
	2014	2015
0.0 - 5.0	233	244
5.0 - 10.0	0	0
10.0 - 15.0	0	0
15.0 - 20.0	0	0
20.0 - 25.0	0	0
25.0 - 50.0	0	0
50.0 -	0	0
Total number of persons monitored	233	244

IX. SCIENTIFIC VISUALIZATION

IX. 1. Educational Practice of Scientific Visualization at CYRIC

Ariga K. and Tashiro M.

Cyclotron and Radioisotope Center, Tohoku University

Introduction

Scientific visualization is an interdisciplinary field including data visualization, imaging, photographs, computer graphics, infographics, illustrations, graphic design, animation, and so on. In the modern world, where personal computers and the internet are popular, visual images in science have been diversified and more colorful than ever. Nowadays, their impacts have been getting stronger and stronger.

In the field of scientific visualization, visual images designed for conveying certain scientific contents in a visually understandable state, such as illustrations, animation, infographics and graphic design, are essential for academic communication and public communication of science. Such visual representations are valuable because they call much attention of the audience to and promote their understanding of the scientific contents so that the conveyed information will remain in their mind more clearly. The popularization of graphics editors such as Adobe Illustrator (Adobe Systems Inc.) lets researchers and students draw illustrations easily. In Japan, however, there have been few opportunities for them to learn such skills, e.g. drawing and graphic design. A specialized educational system has been needed to enhance the visual effectiveness of their research.

At CYRIC, we have carried out education of scientific visualization in order to establish the educational system in Japan. In this report, we describe these educational practices.

Current Situation of Visual Education

In the Western Europe and North America, scientific illustrations have had a long history since the beginning of typography and early modern science[1,2]. Many professionals of scientific illustration, animation and design have been working in hospitals, universities,

research institutes and companies[3-6]. Professional educational systems have been already established in some universities[7,8]. Some teachers of these programs have also given educational lectures to the students who don't major in scientific illustrations but ordinary scientific subjects.

On the other hand, in Japan, the field of scientific visualization covering scientific illustration, design and infographic, has not been popular. It was not until 2011 that a professional course for medical illustrators was established in Kawasaki University of Medical Welfare[9]. There are only a few university teachers who can teach scientific illustration and design. They are scattered in different universities across the country[10]. Education in scientific visualization is not yet systematized in Japan, and almost no students nor researchers have sufficient opportunities to learn drawing and designing. It is necessary to construct a specialized educational system and teaching methods of scientific visualization.

One of important problems, however, is that there are few lectures for students to obtain an overview of the field of scientific visualization. So we have provided omnibus lectures of various fields in scientific visualization. We have also focused on people having different levels of interests and skills of drawing and designing. We have provided some different learning opportunities for various needs.

The University Lectures, "The Age of Visualization"

In 2015, we provided omnibus lectures, "The Age of Visualization ("Kashika no Jidai" in Japanese)", mainly for first-year undergraduates. In these lectures, students studied about medical imaging, image analysis, scientific illustration, infographics, graphic design, 3DCG and visualization in the society, so that they could have an overview of scientific visualization. The lectures were classroom learning, and partly included practical training such as drawing illustrations and making presentations (Fig. 1). The teachers were M. Tashiro (CYRIC), K. Watabe (CYRIC), K. Sato (Graduate School of Educational Informatics), S. Kubo (Graduate School of Information Sciences), K. Ariga (CYRIC) and T. Narashima (Tane+1 LLC). T. Narashima is a professional scientific illustrator. According to the results of questionnaires, students appreciated knowing diverse fields in scientific visualization. It is considered that these lectures broadened student's perspective.

The Lecture Presentation and the Workshop

We held a seminar, "The Technique of Visual Design and Presentation in Academic

Presentation", that was open for a wide range of participants including graduate students, professors and designers. In this seminar, we invited S. Tanaka (Associate Professor, Faculty of Art and Design, University of Tsukuba), Y. Miwa and M. Kobayashi (Assistant Professors, Faculty of Medicine, University of Tsukuba). S. Tanaka studies about education of visual design for scientists and wrote a book about a design guideline of academic presentation. They provided presentations about graphic design with PowerPoint and the method of fascinating presentation (Fig. 2). The audience of more than 50 came and listened to this seminar with attention.

We also held a workshop, "The Technique to Make Comprehensible Infographics." for a class of people having much interest in visual communication in science (Fig. 3). The guest speaker was H. Kimura (TUBE GRAPHICS Co., Ltd.). He has been a leading designer on infographics in Japan. About 20 people participated in this event, and were divided into small groups. Participants made infographics about smartphones on a large sheet of paper with pens in each group. This event was opened to the public, and participants included researchers, university public relations officers, technicians and creators. According to the results of questionnaires, this workshop achieved a high satisfaction level.

Visual Communication Seminar, "AS seminar"

We held a seminar called "AS seminar" to study about comprehensive visual communication. It was held on about twice a month, including two staffs of CYRIC and six students of Graduate School of Sciences and Faculty of Sciences at their own initiative. In this seminar, we made their original infographics through the following procedures. First, the members decided on a common theme (e.g. sunscreen) for their infographics. Second, they had so much discussion on the theme, media and target, and researched about the subject (Fig. 4). Third, they provided concrete ideas of visualization and made sketches of their own infographics. Fourth, they were instructed about designing graphics as well as using a software for visualization, Illustrator. Finally, each of them made a graphic of the common theme (Fig. 5). Through this seminar, the authors explored the effective way of learning complex processes of visual communication.

Conclusion

In this paper, we reported some education practices of scientific visualization. The practices included unique omnibus lectures for undergraduate students, a seminar and

workshop for university faculties and students, and a seminar for higher interested students and staffs. Providing omnibus lectures and multiple education opportunities for different levels of audiences is a unique activity in Japan.

There are some future considerations. These practices except for the omnibus lectures are not connected to university education. They are voluntary works, and it is not easy to continue in the long term. It is needed to appeal to the university administration in order to hold them regularly. We also have to grasp the needs of the researchers and students and develop the teaching method. For example, the workshop may not be fascinating for many researchers because the audience needed to spend long time for their homework and attendance. In the omnibus lectures, we were not able to tell students how each field of scientific visualization was related to others.

Our activity has just started. The authors hope that the design and drawing skills of researchers will increase and the presence of researches and the public understanding of science will be enhanced in Japan.

References

1) Ford BJ, *Images of Science: A History of Scientific Illustration*. The British Library Publishing Division (1993).
2) Roberts KB, Tomlinson JDW, *The Fabric of the Body: European Traditions of Anatomical Illustration*. Oxford: Clarendon Press (1992).
3) Association of Medical Illustrators (AMI) (http://www.ami.org/).
4) Guild of Natural Science Illustrators (GNSI) (http://www.gnsi.org/).
5) Institute of Medical Illustrators (http://www.imi.org.uk/).,
6) Australian Institute of Medical and Biological Illustration (AIMBI) (http://www.aimbi.org.au/).
7) Johns Hopkins University School of Medicine, Department of Art as Applied to Medicine (http://www.hopkins medicine.org/medart/).
8) University of Toronto Biomedical Communications (http://bmc.med.utoronto.ca/bmc/).
9) http://www.kawasaki-m.ac.jp/mw/design/
10) Ariga K, *Jap J Sci Commun* **17** (2015) 23-34 (in Japanese).

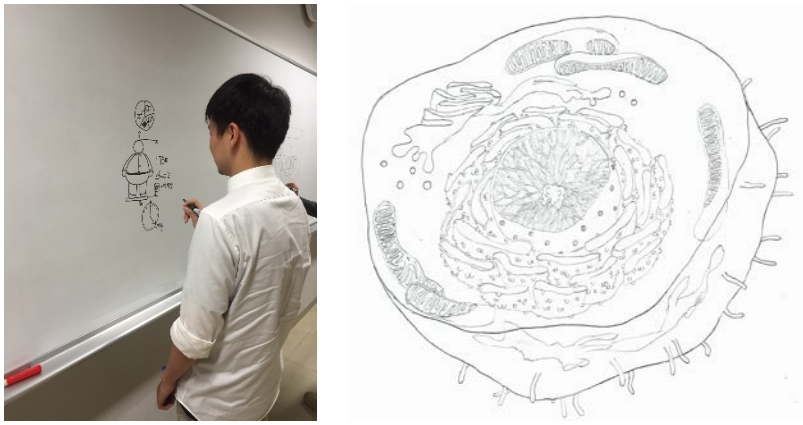

Figure 1. A scene of drawing practice on the white board in the lecture “The Age of Visualization” (LEFT) and the illustration of “Cell” by one of the students (RIGHT).

Figure 2. A scene of the seminar, “The Technique of Visual Design and Presentation in Academic Presentation.” The guest speaker, S. Tanaka gave a presentation about graphic design.

Figure 3. A scene of the workshop, “The Technique to Make Comprehensible Infographics.” The guest speaker, H. Kimura made a speech (Left) and participants had a discussion to make infographics (Right).

Figure 4. A scene of “AS seminar."

Figure 5. The parts of the infographics made by seminar members.

X. PUBLICATIONS

X. PUBLICATIONS

[912] Scintillating fiber detector for momentum tagging light unstable nuclei at intermediate energies.
Matsuda Y., Kobayashi T., Itoh M., Ozeki K., Sakaguchi H., Zenihiro J., Iwao Y., Otsu H., Takeda H., Terashima S.
Nucl. Instr. Meth. A, **670** (2012) 25-31.
http://dx.doi.org/ 10.1016/j.nima.2011.12.029.

[913] Effects of high-energy proton and electron irradiation on GaN Schottky diode.
Narita S., Hitora T., Yamaguchi E., Sakemi Y., Itoh M., Yoshida H., Kasagi J., Neichi K.
Nucl. Instr, Meth. A, **717** (2013) 1-4.
http://dx.doi.org/10.1016/j.nima.2013.04.003.

[914] Search for alpha inelastic condensed state in ^{24}Mg.
Kawabata T., Adachi T., Fujiwara M., Hatanaka K., Ishiguro Y., Itoh M., Maeda Y., Matsubara H., Miyasako H., Nozawa Y., Saito T., Sakaguchi S., Sasamoto Y., Shimizu Y., Takahashi T., Tamii A., Terashima S., Tokieda H., Tomida N., Uesaka T., Uchida M., Yasuda Y., Yokota N., Yoshida H.P., Zenihiro J.
J. Phys. Conf. Seri., **436** (2013) 012009.
http://dx.doi.org/10.1088/1742-6596/436/1/012009.

[915] Nature of 10 MeV state in ^{12}C.
Itoh M., Akimune H., Fujiwara M., Garg U., Kawabata T., Kawase K., Murakami T., Nakanishi K., Nakatsugawa Y., Sakaguchi H., Terashima S., Uchida M., Yasuda Y., Yosoi M., Zenihiro J.
J. Phys. Conf. Seri., **436** (2013) 012006.
http://dx.doi.org/10.1088/1742-6596/436/1/012006.

[916] Non-resonant Triple-α Reaction Rate at Low Temperature.
Tamii A., Aoi N., Fujita H., Fujita Y., Hatanaka K., Hashimoto T., Kawabata T., Miki K., Itoh M., Itoh T., Kamimura M., Ogata K., Ong H.J., Sakaguchi H., Shima T., Suzuki T., Yamamoto T.
Few Body System, **54** (2013) 1607-1610.
http://dx.doi.org/10.1007/s00601-013-0697-y.

[917] Testing the mutually enhanced magicity effect in nuclear incompressibility via the giant monopole resonance in the 204,206,208Pb isotopes.
Patel D., Garg U., Fujiwara M., Adachi T., Akimune H., Berg G.P.A., Harakeh M.N., Itoh M., Iwamoto C., Long A., Matta J.T., Murakami T., Okamoto A., Sault K., Talwar R., Uchida M., Yosoi M.
Phys. Lett. B, **726** (2013) 178-181.
http://dx.doi.org/10.1016/j.physletb.2013.08.027.

[918] Isoscalar giant resonance strengths in 32S and possible excitation of superdeformed

and $^{28}Si + \alpha$ cluster bandheads.
Itoh M., Kishi S., Sakaguchi H., Akimune, H., Fujiwara M., Garg U., Hara K., Hashimoto H., Hoffman J., Kawabata T., Kawase K., Murakami T., Nakanishi K., Nayak B.K., Terashima S., Uchida M., Yasuda Y., Yosoi M.
Phys. Rev. C, **88** (2013) 064313.
http://dx.doi.org/10.1103/PhysRevC.88.064313.

[919] Laser-cooled radioactive francium factory at CYRIC.
Kawamura H., Arikawa H., Ezure S., Harada K., Hayamizu T., Inoue T., Ishikawa T., Itoh M., Kato T., Sato T., Aoki T., Furukawa T., Hatakeyama A., Hatanaka K., Imai K., Murakami T., Nataraj S. H., Shimizu Y., Wakasa T., Yoshida P. H., Sakemi Y.
Nucl. Instr. Meth. B **317** (2013) 582-585.
http://dx.doi.org/10.1016/j.nimb.2013.07.038

[920] Search for permanent EDM using laser cooled Fr atoms.
Kawamura H., Aoki T., Arikawa H., Ezure S., Furukawa T., Harada K., Hatakeyama A., Hatanaka K., Hayamizu T., Imai K., Inoue T., Ishikawa T., Itoh M., Kato T., Murakami T., Nataraj S.H., Sato T., Shimizu Y., Wakasa T., Yoshida P. H., Sakemi Y.
Hyperfine Interact **214** (2013) 133-139.
doi:10.1007/s10751-013-0788-7

[921] Improvement of the energy stability of the Tohoku Dynamitron accelerator for microbeam and nanobeam applications.
Matsuyama S., Fujisawa M., Nagaya T., Ishii K., Terakawa A., Kikuchi Y., Fujiwara M., Watanabe K., Karahashi M., Nozawa Y., Yamauchi S., Ishiya M.
Int. J. PIXE, **23** (2013) 69-75.
http://dx.doi.org/10.1142/S0129083513400081.

[922] Improvement of ion beam brightness by reducing voltage ripple of an electrostatic accelerator for microbeam focusing by a triplet quadrupole lens system having large spherical aberration coefficient.
Matsuyama S., Watanabe K., Ishii K., Terakawa A., Fujisawa M., Koshio S., Toyama S., Itoh S., Fujisawa M., Nagaya T.
Int. J. PIXE, **23** (2013) 171-181.
http://dx.doi.org/10.1142/s012908351341009x.

[923] Studies on radioactive cesium and alkali elements in *lentinula edodes* (Shiitake) based on PIXE analysis.
Terakawa A., Ishii K., Matsuyama S., Hirakata Y., Kikuchi K., Matsuyama T., Fujita A., Kubo K., Toyama S., Watanabe K., Koshio S., Nagakubo K., Sakurada T., Sera K.
Int. J. PIXE, **23** (2013) 147-152.
http://dx.doi.org/10.1142/s0129083513410076.

[924] Use of commercial operational amplifiers in a low cost multi-channel preamplifier system.
Nakhostin M., Kikuchi Y., Ishii K., Matsuyama S., Yamazaki H.
Radiat. Phys. Chem., **85** (2013) 18-22.

[925] Chemical Property of the Size-resolved Asian Dust Particles Measured at Kosan Super-site During ACE-Asia.

Ma C.-J., Yamamoto M., Cao R., Matsuyama S., Sera K.
Earth Environ. Res., **7** (2013) 17-23.

[926] Multimerization of anti-(epidermal growth factor receptor) IgG fragments induces an antitumor effect: the case for humanized 528 scFv multimers.
Asano R., Hagiwara Y., Koyama N., Masakari Y., Orimo R., Arai K., Ogata H., Furumoto S., Umetsu M., Kumagai I.
FEBS J., **280** (2013) 4816-4826.
http://dx.doi.org/10.1111/febs.12451.

[927] Cluster structure of broad resonances near threshold in ^{12}C and ^{16}O.
Itoh M., Akimune H., Fujiwara M., Garg U., Hashimoto H., Kawabata T., Kawase K., Kishi, S., Murakami T., Nakanishi K., Nakatsugawa Y., Nayak B.K., Sakaguchi H., Terashima S., Uchida M., Yasuda Y., Yosoi M., Zenihiro J.
J. Phys. Conf. Seri., **569** (2014) 012009.
http://dx.doi.org/10.1088/1742-6596/569/1/012009.

[928] Characteristics of ZnO Schottky photodiode and effects of high-energy proton irradiation.
Narita S., Endo H., Chiba T., Sakemi Y., Itoh M., Yoshida H.
Phys. Status Solidi A, **211** (2014) 570-573
http://dx.doi.org/10.1002/pssa.201330214

[929] A new neutron detector with a high position resolution for the study of the (p, pn) reaction on rare isotopes.
Kubota Y., Sasano M., Uesaka T., Dozono M., Itoh M., Kawase S., Kobayashi M., Lee C.S., Matsubara H., Miya H., Ota S., Sekiguchi K., Taguchi T., Tang T.L., Tokieda H., Wakui T.
EPJ Web of Conf., **66** (2014) 11022
http://dx.doi.org/10.1051/epjconf/20146611022

[930] Restoration of accelerator facilities damaged by great east Japan earthquake at Cyclotron and Radioisotope Center, Tohoku University.
Wakui T., Itoh M., Shimada K., Yoshida H.P., Shinozuka T., Sakemi Y.
Tohoku J. Exp. Med., **233** (2014) 221-231
http://dx.doi.org/10.1620/tjem.233.221

[931] Excitation of giant monopole resonance in ^{208}Pb and ^{116}Sn using inelastic deuteron scattering.
Patel D., Garg U., Itoh M., Akimune H., Berg G.P.A., Fujiwara M., Harakeh M.N., Iwamoto C., Kawabata T., Kawase K., Matta J.T., Murakami T., Okamoto A., Sako T., Schlax K.W., Takahashi F., White M., Yosoi M.
Phys. Lett. B, **735** (2014) 387-390.
http://dx.doi.org/10.1016/j.physletb.2014.06.073.

[932] Further improvement of the upper limit on the direct 3α decay from the hoyle state in ^{12}C.
Itoh M., Ando S., Aoki T., Arikawa H., Ezure S., Harada K., Hayamizu T., Inoue T., Ishikawa T., Kato K., Kawamura H., Sakemi Y., Uchiyama A.
Phys. Rev. Lett., **113** (2014) 102501.
http://dx.doi.org/10.1103/PhysRevLett.113.102501.

[933] Development of francium atomic beam for the search of the electron electric dipole moment.
Sato T., Ando S., Aoki T., Arikawa H., Ezure S., Harada K., Hayamizu T., Inoue T., Ishikawa T., Itoh M., Kato K., Kato T., Kawamura K., Nataraj S. H., Uchiyama A., Aoki T., Furukawa T., Hatakeyama A., Hatanaka K., Imai K., Murakami T., Shimizu Y., Wakasa T., Yoshida P. H., Sakemi Y.
EPJ Web of Conferences, **66** (2014) 05019.
http://dx.doi.org/10.1051/epjconf/20146605019.

[934] Search for a permanent EDM using laser cooled radioactive atom.
Kawamura H., Ando S., Aoki T., Arikawa H., Ezure S., Harada K., Hayamizu T., Inoue T., Ishikawa T., Itoh M., Kato K., Kato T., Nataraj S. H., Sato T., Uchiyama A., Aoki T., Furukawa T., Hatakeyama A., Hatanaka K., Imai K., Murakami T., Shimizu Y., Wakasa T., Yoshida P. H., Sakemi Y.
EPJ Web of Conferences, **66** (2014) 05009.
http://dx.doi.org/10.1051/epjconf/20146605009.

[935] Development of the measurement system for the search of an electric dipole moment of the electron with laser-cooled francium atoms.
Inoue T., Ando S., Aoki T., Arikawa H., Ezure S., Harada K., Hayamizu T., Ishikawa T., Itoh M., Kato K., Kawamura H., Nataraj S. H., Sato T., Uchiyama A., Aoki T., Furukawa T., Hatakeyama A., Hatanaka K., Imai K., Murakami T., Shimizu Y., Wakasa T., Yoshida P. H., Sakemi Y.
EPJ Web of Conferences, **66** (2014) 05008.
http://dx.doi.org/10.1051/epjconf/20146605008.

[936] Radioactive ion beam transportation for the fundamental symmetry study with laser trapped atoms.
Arikawa H., Ando S., Aoki T., Ezure S., Harada K., Hayamizu T., Inoue T., Ishikawa T., Itoh M., Kawamura H., Kato K., Kato T., Uchiyama A., Aoki T., Furukawa T., Hatakeyama A., Hatanaka K., Imai K., Murakami T., Nataraj S. H., Sato T., Shimizu Y., Wakasa T., Yoshida P. H., Sakemi Y.
Rev. Sci. Instrum., **85** (2014) 02A732.
http://dx.doi.org/10.1063/1.4852218.

[937] Laser cooled francium factory for the electron electric dipole moment search.
Hayamizu T., Arikawa H., Ezure S., Harada K., Inoue T., Ishikawa T., Itoh M., Kato T., Kawamura H., Sato T., Ando S., Aoki T., Uchiyama A., Aoki T., Furukawa T., Hatakeyama A., Hatanaka K., Imai K., Murakami T., Nataraj S. H., Shimizu Y., Wakasa T., Yoshida P. H., Sakemi Y.
JPS Conf. Proc., **1** (2014) 013065.
http://dx.doi.org/10.7566/JPSCP.1.013065.

[938] 3D imaging of human cells using PIXE μCT.
Matsuyama S., Ishii K., Toyama S., Watanabe K., Koshio S., Kasahara K., Ito S., Terakawa A., Fujiwara M., Suzuki Y., Carmona A., Roudeau S., Ortega R.
Int. J. PIXE, **24** (2014) 67-75.
http://dx.doi.org/10.1142/S0129083514500089.

[939] Measurement of distributions of cesium and rubidium in rice grains using micro-PIXE for detailed examinations of contaminated food.

Koshio S., Ishii K., Matsuyama S., Terakawa A., Fujiwara M., Watanabe K., Oshikawa S., Kikuchi K., Itoh S., Kasahara K., Toyama S., Suzuki Y., Matsuyama T., Kamiya T., Satoh T., Koka M., Kitamura A.
Int. J. PIXE, **24** (2014) 17–27.
http://dx.doi.org/10.1142/S0129083514500028.

[940] Evaluating radiocesium retention ability of root-mat horizon using micro-PIXE analysis.
Arai H., Ishii K., Matsuyama S., Fujishiro F., Ishizaki A., Osada N., Sugai H., Koshio S., Kusano K., Nozawa Y., Yamauchi S., Karahashi M., Oshikawa S., Kikuchi K., Watanabe K., Suziki Y., Kikuchi Y., Terakawa A.
Int. J. PIXE, **24** (2014) 29-34.
http://dx.doi.org/10.1142/S012908351450003X.

[941] Concentrations of alkali elements in green tea leaves evaluated using PIXE analysis.
Terakawa A., Ishii K., MatsuyamaS., Matsuyama T., Sato T., Inano K., Shigihara K., Saneshige Y., Sera K.
Int. J. PIXE, **24** (2014) 35-39.
http://dx.doi.org/10.1142/S0129083514500041.

[942] Concentration of cisplatin-incorporated polymeric micelles in a murine solid tumor evaluated using PIXE analysis.
Terakawa A., Ishii K., Matsuyama S., Kikuchi Y., Kawamura T., Takahashi Y., Miura Y., Karahashi M., Kusano K., Yamazaki H., Funaki Y., Mizuno K., Ito N., Wada S., Sera K.
Int. J. PIXE, **24** (2014) 41-47.
http://dx.doi.org/10.1142/S0129083514500053.

[943] Effects of a vascular disrupting agent for cancer treatment on normal tissue evaluated by PIXE analysis using quantum dots.
Terakawa A., Ishii K., Matsuyama S., Kikuchi Y., Kusano K., Karahashi M., Nozawa Y., Yamauchi S., Kikuchi K., Furumoto S., Funaki Y., Ito N., Wada S., Sera K.
Int. J. PIXE, **24** (2014) 59-65.
http://dx.doi.org/10.1142/S0129083514500077.

[944] Improvement and recent applications of the Tohoku microbeam system.
Matsuyama S., Ishii K., Watanabe K., Terakawa A., Kikuchi Y., Fujiwara M., Sugai H., Karahashi M., Nozawa Y., Yamauchi S., Fujisawa M., Ishiya M., Nagaya T., Ortega R., Carmona A., Roudeau S.
Nucl. Instrum. Meth. Phys. Res. B, **318** (2014) 32-36.
http://dx.doi.org/10.1016/j.nimb.2013.06.056.

[945] Reducing logistical barriers to radioactive soil remediation after the Fukushima No. 1 nuclear power plant accident.
Ishii K., Terakawa A., Matsuyama S., Kikuchi Y., Fujishiro F., Ishizaki A., Osada N., Arai H., Sugai H., Takahashi H., Nagakubo K., Sakurada T., Yamazaki H., Kim S.
Nucl. Instrum. Meth. Phys. Res. B, **318** (2014) 70-75.
http://dx.doi.org/10.1016/j.nimb.2013.06.067.

[946] Micro-PIXE evaluation of radioactive cesium transfer in contaminated soil samples.
Fujishiro F., Ishii K., Matsuyama S., Arai H., Ishizaki A., Osada N., Sugai H., Kusano K.,

Nozawa Y., Yamauchi S., Karahashi M., Oshikawa S., Kikuchi K., Koshio S., Watanabe K., Suzuki Y.
Nucl. Instrum. Meth. Phys. Res. B, **318** (2014) 99-101.
http://dx.doi.org/10.1016/j.nimb.2013.06.059.

[947] Remediation of plants contaminated with cesium by aqueous cleaning.
Osada N., Ishii K., Matsuyama S., Sugai H., Kusano K., Nozawa Y., Yamauchi S., Karahashi M., Oshikawa S., Kikuchi K., Koshio S., Watanabe K., Itoh S., Suzuki Y., Terakawa A., Kikuchi Y., Fujishiro F., Ishizaki A., Arai H.
Nucl. Instrum. Meth. Phys. Res. B, **318** (2014) 102-104.
http://dx.doi.org/10.1016/j.nimb.2013.06.050.

[948] Concentration of Cs in plants and water resulting from radioactive pollution.
Ishizaki A., Ishii K., Matsuyama S., Fujishiro F., Arai H., Osada N., Sugai H., Koshio S., Yamauchi S., Kusano K., Nozawa Y., Karahashi M., Oshikawa S., Kikuchi K., Watanabe K., Itoh S., Kasahara, K. Toyama S., Suzuki Y.
Nucl. Instrum. Meth. Phys. Res. B, **318** (2014) 105-108.
http://dx.doi.org/10.1016/j.nimb.2013.06.049.

[949] PIXE analyses of cesium in rice grains.
Sugai H., Ishii K., Matsuyama S., Terakawa A., Kikuchi Y., Takahashi H., Ishizaki A., Fujishiro F., Arai H., Osada N., Karahashi M., Nozawa Y., Yamauchi S., Kikuchi K., Koshio S., Watanabe K.
Nucl. Instrum. Meth. Phys. Res. B, **318** (2014) 191-193.
http://dx.doi.org/10.1016/j.nimb.2013.06.060.

[950] Application of PIXE analysis to investigation of plants cultivated with contaminated soil of Fukushima.
Ishii K., Terakawa A., Matsuyama S., Ishizaki A., Arai H., Osada N., Sugai H., Takahashi H., Sera K., Sasaki H., Sasaki K., Sawamura T.
Nucl. Instrum. Meth. Phys. Res. B, **332** (2014) 46-49.
http://dx.doi.org/10.1016/j.nimb.2014.02.027.

[951] Development of a high-current microbeam system.
Matsuyama S., Ishii K., Suzuki S., Terakawa A., Fujiwara M., Koshio S., Toyama S., Ito S., Fujisawa, M. Nagaya T.
Int. J. PIXE, **24** (2014) 101-110.
http://dx.doi.org/10.1142/S0129083514400038.

[952] Development of a WDX-μ-PIXE system for chemical state mapping.
Toyama S., Matsuyama S., Ishii K., Terakawa A., Kasahara K., Sata D., Itoh S., Tanimukai T., Uegaki J., Tada T.
Int. J. PIXE, **24** (2014) 111-120.
http://dx.doi.org/10.1142/S012908351440004X.

[953] Development of a method for analyzing the composition of ambient PM2.5 floating dust particles by micro-PIXE.
Oshikawa S., Itoh S., Matsuyama S., Ishii K., Terakawa A., Koshio S., Watanabe K., Toyama S., Kasahara K., Ma C.-J.
Int. J. PIXE, **24** (2014) 121-129.

http://dx.doi.org/10.1142/S0129083514400051.

[954] Micro-PIXE analysis of the distribution of cesium in clay particles for environmental remediation of Fukushima.
Ishii K., Itoh S., Sata D., Matsuyama S., Terakawa A., Kim S., Arai H., Osada N., Satoh T., Koka M., Kitamua A., Kamiya T.
Int. J. PIXE, **24** (2014) 131-136.
http://dx.doi.org/10.1142/S0129083514400063.

[955] An X-ray pinhole camera using metallic radioisotopes emitting only characteristic X-rays.
Ishii K., Kawano H., Inagaki S., Sato Y., Maruyama T., Fujiwara M., Arai H., Terakawa A., Matsuyama S.
Int. J. PIXE, **24** (2014) 189-195.
http://dx.doi.org/10.1142/S0129083514400117**.**

[956] Accumulation and localization of alkali elements in Lentinula edodes studied by PIXE analysis.
Terakawa A., Ishii K., Matsuyama S., Hirakata H., Fujita A., Kikuchi K., Matsuyama T., Toyama S., Watabe K., Koshio S., Nagakubo K., Sakurada T., Sera K.
Int. J. PIXE, **24** (2014) 197-204.
http://dx.doi.org/10.1142/S0129083514400129.

[957] In vivo evaluation of a novel tau imaging tracer for Alzheimer's disease.
Villemagne V.L., Furumoto S., Fodero-Tavoletti M.T., Mulligan R.S., Hodges J., Harada R., Yates P., Piguet O., Pejoska S., Doré V., Yanai K., Masters C.L., Kudo Y., Rowe C.C., Okamura N.
Eur. J. Nucl. Med. Mol. Imaging, **41** (2014) 11.
http://dx.doi.org/10.1007/s00259-013-2681-7.

[958] Assessing THK523 selectivity for tau deposits in Alzheimer's disease and non-Alzheimer's disease tauopathies.
Fodero-Tavoletti M.T., Furumoto S., Taylor L., McLean C.A., Mulligan R.S., Birchall I., Harada R., Masters C.L., Yanai K., Kudo Y., Rowe C.C., Okamura N., Villemagne V.L.
Alzheimers. Res. Ther., **6** (2014) 816-826.
http://dx.doi.org/10.1186/alzrt240.

[959] Non-invasive assessment of Alzheimer's disease neurofibrillary pathology using ^{18}F-THK5105 PET.
Okamura N., Furumoto S., Fodero-Tavoletti M.T., Mulligan R.S., Harada R., Yates P., Pejoska S., Kudo Y., Masters C.L., Yanai K., Rowe C.C., Villemagne V.L.
Brain, **137 (Pt 6)** (2014) 1762-1771.
http://dx.doi.org/10.1093/brain/awu064.

[960] Tau PET imaging in Alzheimer's disease.
Okamura N., Harada R., Furumoto S., Arai H., Yanai K., Kudo Y.
Curr. Neurol. Neurosci. Rep., **14** (2014) 500.
http://dx.doi.org/10.1007/s11910-014-0500-6.

[961] Voyage au bout de la nuit: Aβ and tau imaging in dementias.

Zwan M.D., Okamura N., Fodero-Tavoletti M.T., Furumoto S., Masters C.L., Rowe C.C., Villemagne V.L.
Q. J. Nucl. Med. Mol. Imaging, **58** (2014) 398-412.

[962] Rearranging the domain order of a diabody-based IgG-like bispecific antibody enhances its antitumor activity and improves its degradation resistance and pharmacokinetics.
Asano R., Shimomura I., Konno S., Ito A., Masakari Y., Orimo R., Taki S., Arai K., Ogata H., Okada M., Furumoto S., Onitsuka M., Omasa T., Hayashi H., Katayose Y., Unno M., Kudo T., Umetsu M., Kumagai I.
MAbs., **6** (2014) 1243-1254.
http://dx.doi.org/ 10.4161/mabs.29445.

[963] Synthesis and preliminary evaluation of 2-arylhydroxyquinoline derivatives for tau imaging.
Tago T., Furumoto S., Okamura N., Harada R., Ishikawa Y., Yanai K., Iwata R., Kudo Y.
J. Label. Compd. Radiopharm., **57** (2014) 18-24.
http://dx.doi.org/10.1002/jlcr.3133.

[964] Standardized uptake value in high uptake area on positron emission tomography with ^{18}F-FRP170 as a hypoxic cell tracer correlates with intratumoral oxygen pressure in glioblastoma.
Beppu T., Terasaki K., Sasaki T., Fujiwara S., Matsuura H., Ogasawara K., Sera K., Yamada N., Sugai T., Kudo K., Sasaki M., Ehara S., Iwata R., Takai Y.
Mol. Imag. Biol., **16**, (2014) 127-135.
http://dx.doi.org/10.1007/s11307-013-0670-7.

[965] Analysis of early phase [^{11}C]BF-227 PET, and its application for anatomical standardization of late-phase images for 3D-SSP analysis.
Kaneta T., Okamura N., Arai A., Takanami K., Furukawa K., Tashiro M., Furumoto S., Iwata R., Takahashi S., Arai H., Yanai K., Kudo Y.
Jpn. J. Radiol., **32** (2014) 138-44.
http://dx.doi.org/ 10.1007/s11604-013-0276-7.

[966] Pitfalls of voxel-based amyloid PET analysis for diagnosis of Alzheimer's disease: Artifacts due to non-specific uptake in the white matter and skull.
Arai A., Kaneta T., Okamura N., Tashiro M., Iwata R., Takanami K., Fukuda H., Takahashi S., Yanai K., Kudo Y., Arai H.
Tohoku J. Exp. Med., **234** (2014) 175-181.
http://dx.doi.org/10.1620/tjem.234.175.

[967] Effects of magnesium deficiency on magnesium uptake activity of rice root, evaluated using ^{28}Mg as a tracer.
Tanoi M., Kobayashi N.I., Saito T., Iwata N., Kamada R., Iwata R., Suzuki H., Hirose A., Ohmae Y., Sugita R., Nakanishi T.M.
Plant Soil, **384** (2014) 69-77.
http://dx.doi.org/10.10807/s11104-014-2197-3.

[968] Distribution of intravenously administered acetylcholinesterase inhibitor and acetylcholinesterase activity in the adrenal gland: ^{11}C-Donepezil PET study in the normal rat.
Watabe T., Naka S., Ikeda H., Horitsugi G., Kanai Y., Isohashi K., Ishibashi M., Kato H.,

Shimosegawa E., Watabe H., Hatazawa J.
Pros One, **9** (2014) e107427.
http://dx.doi.org/10.1371/journal.pone.0107427.

[969] Three-layer GSO depth-of-interaction detector for high-energy gamma camera.
Yamamoto S., Watabe H., Kawachi N., Fujimaki S., Kato K., Hatazawa J.
Nucl. Inst. Meth. Phys. Res. SecA, **743** (2014) 124-129.
http://dx.doi.org/10.1016/j.nima.2014.01.011.

[970] Development of a PET/Cerenkov-light hybrid imaging system.
Yamamoto S., Hamamura F., Watabe T., Ikeda H., Kanai Y., Watabe H., Kato K., Ogata Y., Hatazawa J.
Med. Phys., **41** (2014) 092504.
http://dx.doi.org/10.1118/1.4893535

[971] Development of a high-resolution YSO gamma camera system that employs 0.8-mm pixels.
Yamamoto S., Watabe H., Kanai Y., Kato K., Hatazawa J.
Ann. Nucl. Med., **28** (2014) 232-40.
http://dx.doi.org/10.1007/s12149-013-0800-y.

[972] Rapid synthesis of ^{62}Zn-labeled S-glycosylated porphyrin as positron emission tomography tracers for in vivo PET imaging.
Tamura M., Matsui H., Hirohara S., Kakiuchi K., Tanihara M., Takahashi N., Nakai K., Kanai Y., Watabe H., Hatazawa J.
Chem. Lett., **43** (2014) 778-80.
http://dx.doi.org/10.1246/cl.140056.

[973] Ultrahigh-resolution Cerenkov-light imaging system for positron radionuclides: potential applications and limitations.
Suto T., Meguro K., Nakatsuka M., Kato Y., Tezuka K., Yamaguchi S, Tashiro M.
Psychogeriatrics, **26** (2014) 1127-1138.
http://dx.doi.org/10.1017/S1041610214000532.

[974] Disorders of “taste cognition” are associated with insular involvement in patients with Alzheimer’s disease and vascular dementia: “Memory of food is impaired in dementia and responsible for poor diet.”
Yamamoto S., Watabe T., Ikeda H., Kanai Y., Watabe H., Ogata Y., Kato K., Hatazawa J.
Ann. Nucl. Med., **28** (2014) 961-9.
http://dx.doi.org/10.1007/s12149-014-0892-z.

[975] Differences in muscle activities during shoulder elevation in patients with symptomatic and asymptomatic rotator cuff tears: analysis by positron emission tomography.
Shinozaki N., Sano H., Omi R., Kishimoto K.N., Yamamoto N., Tashiro M, Itoi E.
J. Shoulder Elbow Surg., **23** (2014) 61-67.
http://dx.doi.org/10.1016/j.jse.2013.06.009.

[976] Muscle activity pattern of the shoulder external rotators differs in adduction and abduction: an analysis using positron emission tomography.
Kurokawa D., Sano H., Nagamoto H., Omi R., Shinozaki N., Watanuki S., Kishimoto K.N.,

Yamamoto N., Hiraoka K., Tashiro M., Itoi E.
J. Shoulder Elbow Surg., **23** (2014) 658-664.
http://dx.doi.org/10.1016/j.jse.2013.12.021.

[977] Enhanced [^{18}F]fluorodeoxyglucose accumulation in the right ventricular free wall predicts long-term prognosis of patients with pulmonary hypertension: a preliminary observational study.
Tatebe S., Fukumoto Y., Oikawa-Wakayama M., Sugimura K., Satoh K., Miura Y., Aoki T., Nochioka K., Miura M., Yamamoto S., Tashiro M., Kagaya Y., Shimokawa H.
Eur. Heart J. Cardiovasc. Imaging, **15** (2014) 666-672.
http://dx.doi.org/10.1093/ehjci/jet276.

[978] Nonquenched isoscalar spin- M1 excitations in sd -shell nuclei.
Matsubara H., Tamii A., Nakada H., Adachi T., Carter J., Dozono M., Fujita H., Fujita K., Fujita Y., Hatanaka K., Horiuchi W., Itoh M., Kawabata T., Kuroita S., Maeda Y., Navrátil P., Von Neumann-Cosel P., Neveling R., Okamura H., Popescu L., Poltoratska I., Richter A., Rubio B., Sakaguchi H., Sakaguchi S., Sakemi Y., Sasamoto Y., Shimbara Y., Shimizu Y., Smit F.D., Suda K., Tameshige Y., Tokieda H., Yamada Y., Yosoi M., Zenihiro J.
Phys. Rev. Lett., **115** (2015) 102501.
http://dx.doi.org/10.1103/PhysRevLett.115.102501.

[979] Splitting of ISGMR strength in the light-mass nucleus ^{24}Mg due to ground-state deformation.
Gupta Y.K., Garg U., Matta J.T., Patel D., Peach T., Hoffman J., Yoshida K., Itoh M., Fujiwara M., Hara K., Hashimoto H., Nakanishi K., Yosoi M., Sakaguchi H., Terashima S., Kishi S., Murakami T., Uchida M., Yasuda Y., Akimune H., Kawabata T., Harakeh M.N.
Phys. Lett. B, **748** (2015) 343-346.
http://dx.doi.org/10.1016/j.physletb.2015.07.021.

[980] Experimental search for the electron electric dipole moment with laser cooled francium atoms.
Inoue T., Ando S., Aoki T., Arikawa H., Ezure S., Harada K., Hayamizu T., Ishikawa T., Itoh M., Kato K., Kawamura H., Uchiyama A., Aoki T., Asahi K., Furukawa T., Hatakeyama A., Hatanaka K., Imai K., Murakami T., Nataraj S. H., Sato T., Shimizu Y., Wakasa T., Yoshida P. H., Yoshimi A., Sakemi Y.
Hyperfine Interaction, **231** (2015) 157-162.
doi:10.1007/s10751-014-1100-1.

[981] Development of laser light sources for trapping radioactive francium atoms toward tests of fundamental symmetries.
Harada K., Ezure S., Hayamizu T., Kato K., Kawamura H., Inoue T., Arikawa H., Ishikawa T., Aoki T., Uchiyama A., Itoh M., Ando S., Aoki T., Hatakeyama A., Hatanaka K., Imai K., Murakami T., Shimizu Y., Sato T., Wakasa T., Yoshida P. H., Sakemi Y.
JPS Conf. Proc., **6** (2015) *030128*.
http://dx.doi.org/10.7566/JPSCP.6.030128.

[982] Development of Magnetometer Based on the Nonlinear Magneto-Optical Rotation Effect Toward the Measurement of the Electron Electric Dipole Moment.
Inoue T., Ando S., Aoki T., Arikawa H., Ezure S., Harada K., Hayamizu T., Ishikawa T., Itoh M., Kato K., Kawamura H., Uchiyama A., Aoki T., Asahi K., Furukawa T., Hatakeyama A.,

Hatanaka K., Imai K., Murakami T., Nataraj S. H., Sato T., Shimizu Y., Wakasa T., Yoshimi A., Yoshida P. H., Sakemi Y.
JPS Conf. Proc., **6** (2015) *030070*.
http://dx.doi.org/10.7566/JPSCP.6.030070.

[983] Towards the Measurement of the Electric-Dipole Moment of Radioactive Francium using Laser-Cooling and Trapping Techniques.
Kawamura H., Ando S., Aoki T., Arikawa H., Ezure S., Harada K, Hayamizu T., Inoue T., Ishikawa T., Itoh M, Kato K., Uchiyama A., Aoki T., Furukawa T., Hatakeyama A., Hatanaka K., Imai K., Murakami T., Nataraj S. H., Sato T., Shimizu Y., Wakasa T., Yoshida P. H., Sakemi Y.
JPS Conf. Proc., **6** (2015) *030068*.
http://dx.doi.org/10.7566/JPSCP.6.030068.

[984] Magneto-optical trapping of radioactive atoms for test of the fundamental symmetries.
Kawamura H., Ando S., Aoki T., Arikawa H., Harada K., Hayamizu T., Inoue T., Ishikawa T., Itoh M., Kato K., Köhler L., Mathis J., Sakamoto K., Uchiyama A., Sakemi Y.
Hyperfine Interaction **236** (2015) 53-58.
http://dx.doi.org/10.1007/s10751-015-1193-1.

[985] A micro-pattern gaseous detector for beam monitoring in ion-therapy.
Terakawa A., Ishii K., Matsuyama S., Kikuchi Y., Togashi T., Arikawa J., Yamashita W., Takahashi Y., Fujishiro F., Yamazaki H., Sakemi Y.
Nucl. Instrum. Meth. Phys. Res. B, **365** (2015) 606-610.
http://dx.doi.org/10.1016/j.nimb.2015.09.023

[986] The Determination of Soil-Plant Transfer Coefficients of Cesium-137 and Other Elements by γ-Ray Measurement and PIXE Analysis, For Use in the Remediation of Fukushima.
Ishii K., Fujita A., Toyama S., Terakawa A., Matsuyama S., Arai H., Osada N., Takyu S., Matsuyama T., Koshio S., Watanabe K., Ito S., Kasahara K.
Phys. Procedia, **66** (2015) 278-286.

[987] *In vivo* 3D PIXE-micron-CT imaging of Drosophila melanogaster using a contrast agent.
Matsuyama S., Hamada N., Ishii K., Nozawa Y., Ohkura S., Terakawa A., Hatori Y., Fujiki K., Fujiwara M., Toyama S.
Nucl. Instrum. Meth. Phys. Res. B, **348** (2015) 123-126.
http://dx.doi.org/10.1016/j.nimb.2014.11.039.

[988] Pre-computed system matrix calculation based on a piece-wise method for PET
Ahmed A.M., Kikuchi Y., Matsuyama S., Terakawa A., Takyu S., Sugai H., Ishii K.
Radiol. Phys. Tech., **8** (2015) 88-96.
http://dx.doi.org/10.1007/s12194-014-0293-y.

[989] [^{18}F]THK-5117 PET for assessing neurofibrillary pathology in Alzheimer disease.
Harada R., Okamura N., Furumoto S., Furukawa K., Ishiki A., Tomita N., Hiraoka K., Watanuki S., Shidahara M., Miyake M., Ishikawa Y., Matsuda R., Inami A., Yoshikawa T., Tago T., Funaki Y., Iwata R., Tashiro M., Yanai K., Arai H., Kudo Y.
Eur. J. Nucl. Med. Mol. Imag., **42** (2015) 1052-1061.

http://dx.doi.org/10.1007/s00259-015-3035-4.

[990] High-uptake areas on positron emission tomography with the hypoxic radiotracer ^{18}F-FRP170 in glioblastomas include regions retaining proliferative activity under hypoxia.
Beppu T., Sasaki T., Terasaki K., Saura H., Matsuura H., Ogasawara K., Sasaki M., Ehara S., Iwata R., Takai Y.
Ann. Nucl. Med., **29** (2015) 336-341.
http://dx.doi.org/10.1007/s12149-015-0951-0.

[991] Histamine H_1 receptor occupancy by the new-generation antipsychotics olanzapine and quetiapine: a positron emission tomography study in healthy volunteers.
Sato H., Ito C., Hiraoka K., Tashiro M., Shibuya K., Funaki Y., Yoshikawa T., Iwata R., Matsuoka H., Yanai K.
Psychopharmacol., **232** (2015) 3497-3505.
http://dx.doi.org/10.1007/s00213-015-4002-2.

[992] Quantitative kinetic analysis of PET amyloid imaging agents [^{11}C]BF227 and [^{18}F]FACT in human brain.
Shidahara M., Watabe H., Tashiro M., Okamura N., Furumoto S., Watanuki S., Furukawa K., Arakawa Y., Funaki Y., Iwata R., Gonda K., Kudo Y., Arai H., Ishikawa Y., Yanai K.
Nucl. Med. Biol., **47** (2015) 734-744.
http://dx.doi.org/10.1016/j.nucmedbio.2015.05.001.

[993] Longitudinal assessment of tau pathology in patients with Alzheimer's disease using [^{18}F]THK-5117 positron emission tomography.
Ishiki A., Okamura N., Furukawa K., Furumoto S., Harada R., Tomita N., Hiraoka K., Watanuki S., Ishikawa Y., Tago T., Funaki Y., Iwata R., Tashiro M., Yanai K., Kudo Y., Arai H.
Plos One, **10** (2015) e0140311.
http://dx.doi.org/10.1371/journal.pone.0140311.

[994] Cortical laminar binding of PET amyloid and tau tracers in Alzheimer disease.
Li Y., Tsui W., Rusinek H., Butler T., Mosconi L., Pirraglia E., Mozley D., Vallabhajosula S., Harada R., Furumoto S., Furukawa K., Arai H., Kudo Y., Okamura N., de Leon M.J.
J. Nucl. Med., **56** (2015) 270-273.
http://dx.doi.org/10.2967/jnumed.114.149229.

[995] Amyloid deposits and response to shunt surgery in idiopathic normal-pressure hydrocephalus.
Hiraoka K., Narita W., Kikuchi H., Baba T., Kanno S., Iizuka O., Tashiro M., Furumoto S., Okamura N., Furukawa K., Arai H., Iwata R., Mori E., Yanai K.
J. Neurol. Sci., **356** (2015) 124-128.
http://dx.doi.org/10.1016/j.jns.2015.06.029.

[996] Development of dual-layer GSO depth-of-interaction block detector using angled optical fiber.
Okumura S., Yamamoto S., Watabe H., Kato N., Hamamura H.
Nucl. Inst. Meth. Phys. Res. SecA, **781** (2015) 65-70.
http://dx.doi.org/10.1016/j.nima.2015.01.102.

[997] Development of an Optical Fiber-Based MR Compatible Gamma Camera for SPECT/MRI Systems.
Yamamoto S., Watabe T., Kanai Y., Watabe H., Hatazawa J.
IEEE Trans. Nucl. Sci., **62** (2015) 76-81.
http://dx.doi.org/10.1109/TNS.2014.2387432.

[998] Pharmacological MRI response to a selective dopamine transporter inhibitor, GBR12909, in awake and anesthetized rats.
Kashiwagi Y., Rokugawa T., Yamada T., Obata A., Watabe H., Yoshioka Y., Abe K.
Synapse, **69** (2015) 203-212.
http://dx.doi.org/10.1002/syn.21803.

[999] Cell-sheet therapy with omentopexy promotes arteriogenesis and improves coronary circulation physiology in failing heart.
Kainuma S., Miyagawa S., Fukushima S., Pearson J., Chen Y.C., Saito A., Harada A., Shiozaki M., Iseoka H., Watabe T., Watabe H., Horitsugi G., Ishibashi M., Ikeda H., Tsuchimochi H., Sonobe T., Fujii Y., Naito H., Umetani K., Shimizu T., Okano T., Kobayashi E., Daimon T., Ueno T., Kuratani T., Toda K., Takakura N., Hatazawa J., Shirai M., Sawa Y.
Mol. Therapy, **23** (2015) 374-86.
http://dx.doi.org/10.1038/mt.2014.225.

[1000] Singing can improve speech function in aphasics associated with intact right basal ganglia and preserve right temporal glucose: Implications for singing therapy indication.
Akanuma K., Meguro K., Satoh M., Tasiro M., Itoh M.
J. Neurosci., **126** (2016) 39-45.
http://dx.doi.org/10.3109/00207454.2014.992068.

[1001] Prediction of outcomes in mild cognitive impairment by using ^{18}F-FDG-PET: a multicenter study.
Ito K., Fukuyama H., Senda M., Ishii K., Maeda K., Yamamoto Y., Ouchi Y., Ishii K., Okumura A., Fujiwara K., Kato T., Arahata Y., Washimi Y., Mitsuyama Y., Meguro K., Ikeda M.; Sead-J Study Group.
J. Alzheim. Disease, 45(2015) 543-552.
http://dx.doi.org/10.3233/JAD-141338.

[1002] Brain histamine H1 receptor occupancy measured by PET after oral administration of levocetirizine, a non-sedating antihistamine.
Hiraoka K., Tashiro M., Grobosch T., Maurer M., Oda K., Toyohara J., Ishii K., Ishiwata K., Yanai K.
Expert Opin. Drug Saf., **14** (2015) 199-206.
http://dx.doi.org/10.1517/14740338.2015.989831.

XI. MEMBERS OF COMMITTEES

XI. MEMBERS OF COMMITTEES (as of Jan. 1, 2016)

General

(Chairman)	Kazuhiko	Yanai	(Graduate School of Medicine)
	Sadayoshi	Itou	(Executive Vice President)
	Kimiko	Sekiguchi	(Graduate School of Science)
	Kazuaki	Iwasa	(Graduate School of Science)
	Yoshio	Hosoi	(Graduate School of Medicine)
	Keiichi	Sasaki	(Graduate School of Dentistry)
	Noriyasu	Hirasawa	(Graduate School of Pharmaceutical Sciences)
	Akira	Hasegawa	(Graduate School of Engineering)
	Keiichi	Konoki	(Graduate School of Agricultural Science)
	Kazuhiro	Sogawa	(Graduate School of Life Sciences)
	Atsuki	Terakawa	(Graduate School of Biomedical Engineering)
	Asao	Yamamura	(Institute for Materials Research)
	Yasuyuki	Taki	(Institute of Development, Aging and Cancer)
	Nobuaki	Sato	(Institute of Multidisciplinary Research for Advanced Materials)
	Keiichi	Jingu	(University Hospital)
	Toshimi	Suda	(Research Center for Electron Photon Science)
	Yasuhiro	Sakemi	(CYRIC)
	Manabu	Tashiro	(CYRIC)
	Hiroshi	Watabe	(CYRIC)
	Shozo	Furumoto	(CYRIC)
	Masatoshi	itoh	(CYRIC)
	Hirokazu	Tamura	(Graduate School of Science)
	Yoshitaka	Kinouchi	(Institute for Excellence in Higher Education)
	Keiichi	Itoi	(Radiation Safety Committee, Research

Promotion Council)

Cyclotron

(Chairman)	Yasuhiro	Sakemi	(CYRIC)
	Toshio	Kobayashi	(Graduate School of Science)
	Hirokazu	Tamura	(Graduate School of Science)
	Kimiko	Sekiguchi	(Graduate School of Science)
	Kazuaki	Iwasa	(Graduate School of Science)
	Yasushi	Kino	(Graduate School of Science)
	Akira	Hasegawa	(Graduate School of Engineering)
	Atsuki	Terakawa	(Graduate School of Engineering)
	Yuki	Satoh	(Institute for Materials Research)
	Nobuaki	Sato	(Institute of Multidisciplinary Research)
	Toshimi	Suda	(Research Center for Electron Photon Science)
	Manabu	Tashiro	(CYRIC)
	Hiroshi	Watabe	(CYRIC)
	Shozo	Furumoto	(CYRIC)
	Masatoshi	Itoh	(CYRIC)

Radiation Protection and Training of Safe Handling

(Chairman)	Kazuhiko	Yanai	(Graduate School of Medicine)
	Naohito	Iwasa	(Graduate School of Science)
	Yoshihiko	Uehara	(Graduate School of Medicine)
	Noriyasu	Hirasawa	(Graduate School of Pharmaceutical Sciences)
	Atsuki	Terakawa	(Graduate School of Engineering)
	Katuya	Gomi	(Graduate School of Agricultural Science)
	Kennsaku	Mizuno	(Institute for Materials Research)
	Yasuyoshi	Nagai	(Institute for Materials Research)
	Motoaki	Sugiura	(Institute of Development, Aging and Cancer)
	Kentaro	Takanami	(University Hospital)
	Manabu	Tashiro	(CYRIC)
	Hiroshi	Watabe	(CYRIC)

	Shozo	Furumoto	(CYRIC)

Life Science

(Chairman)	Manabu	Tashiro	(CYRIC)
	Kazuhiko	Yanai	(Graduate School of Medicine)
	Haruo	Saito	(Graduate School of Medicine)
	Yoshio	Hosoi	(Graduate School of Medicine)
	Kei	Takase	(Graduate School of Medicine)
	Nobuyuki	Okamura	(Graduate School of Medicine)
	Mikiko	Suzuki	(Graduate School of Medicine)
	Keiichi	Sasaki	(Graduate School of Dentistry)
	Masahiro	Hiratsuka	(Graduate School of Pharmaceutical Sciences)
	Atsuki	Terakawa	(Graduate School of Biomedical Engineering)
	Kensaku	Mizuno	(Graduate School of Engineering)
	Toshihiko	Ogura	(Graduate School of Life Sciences)
	Yukitsuka	Kudo	(Innovation of New Biomedical Engineering Center)
	Nariyasu	Mano	(University Hospital)
	Yasuhiro	Sakemi	(CYRIC)
	Hiroshi	Watabe	(CYRIC)
	Shozo	Furumoto	(CYRIC)
	Yoshihito	Funaki	(CYRIC)
	Kotaro	Hiraoka	(CYRIC)

Prevention of Radiation Hazards

(Chairman)	Manabu	Tashiro	(CYRIC)
	Naohito	Iwasa	(Graduate School of Science)
	Yasushi	Kino	(Graduate School of Science)
	Keizo	Ishii	(Graduate School of Engineering)
	Yasuhiro	Sakemi	(CYRIC)
	Hiroshi	Watabe	(CYRIC)
	Shozo	Furumoto	(CYRIC)
	Masatoshi	Itoh	(CYRIC)
	Hideyuki	Yuki	(CYRIC)
	Katsuo	Aizawa	(CYRIC)

Research Program

(Chairman)	Yasuhiro	Sakemi	(CYRIC)
	Hirokazu	Tamura	(Graduate School of Science)
	Kazushige	Maeda	(Graduate School of Science)
	Kimiko	Sekiguchi	(Graduate School of Science)
	Kazuhiko	Yanai	(Graduate School of Medicine)
	Shin	Fukudo	(Graduate School of Medicine)
	Etsuro	Mori	(Graduate School of Medicine)
	Akira	Hasegawa	(Graduate School of Engineering)
	Atsuki	Terakawa	(Graduate School of Engineering)
	Akira	Takahashi	(Graduate School of Medicine)
	Yuki	Satoh	(Institute for Materials Research)
	Hiroyuki	Arai	(Institute of Development, Aging and Cancer)
	Yasuyuki	Taki	(Institute of Development, Aging and Cancer)
	Keiichi	Jingu	(University Hospital)
	Toshimi	Suda	(Research Center for Electron Photon Science)
	Hidetoshi	Kikunaga	(Research Center for Electron Photon Science)
	Tsutomu	Sekine	(Institute Excellence in Higher Education)

	Manabu	Tashiro	(CYRIC)
	Hiroshi	Watabe	(CYRIC)
	Shozo	Furumoto	(CYRIC)
(Observer)	Masatoshi	Itoh	(CYRIC)
(Observer)	Hideyuki	Yuki	(CYRIC)

XII. STAFF AND STUDENTS

XII. STAFF AND STUDENTS (as of Jan. 1, 2016)

Director Kazuhiko Yanai

Division of Accelerator

Masatoshi	Itoh
Tomohiro	Hayamizu
Tsutomu	Shinozuka[1)]
Yoshihiro	Shimbara[2)]
Yasuaki	Ohmiya[3)]
Naoto	Takahashi[3)]
Jyunya	Suzuki[3)]
Ken	Takahashi[3)]
Takayuki	Honma[3)]

Division of Instrumentations

Yasuhiro	Sakemi
Hirokazu	Tamura[4)]
Atsuki	Terakawa[5)]
Umakanth	Dammalapati
Kenichi	Harada
Takeshi	Inoue[6)]
Hirokazu	Kawamura[6)]
Hikonojo	Orihara[1)]

Division of Radiopharmaceutical Chemistry

Shozo	Furumoto
Yukitsuka	Kudo[7)]
Yoshihito	Funaki
Yoichi	Ishikawa

Ren	Iwata[1,8)]
Kazuko	Takeda
Kiichi	Ishiwata[1)]
Kazutoshi	Suzuki[1)]

Division of Cyclotron Nuclear Medicine

Manabu	Tashiro
Nobuyuki	Okamura[9)]
Miho	Shidahara[9)]
Kotaro	Hiraoka
Shoichi	Watanuki
Kana	Ariga
Keiichiro	Yamaguchi[1)]
Kazuo	Kubota[1)]
Hiroshi	Fukuda[1)]
Iwao	Kanno[1)]
Ikuo	Onoda[1)]
Takeshi	Ogura[2)]
Tomoyuki	Narashima[2)]
Jo	Morishita[2)]
Kyokuto	Dan[2)]

Division of Radiation Protection and Safety Control

Hiroshi	Watabe
Keizou	Ishi[5)]
Shigeo	Matsuyama[5)]
Masayasu	Miyake
Hideyuki	Yuki
Takashi	Nakamura[1)]
Mamoru	Baba[1)]
Esshu	Kuraoka[1)]
Kazuhiro	Ohtomo
Shinichi	Kikuchi
Hirokazu	Nakae[11)]

Division of Geriatric Behavioral Neurology

Kenichi	Meguro
Takashi	Seki
Kei	Nakamura
Mari	Kasai[1)]
Hideki	Yamazaki[1)]
Yoritoshi	Kobayashi[2)]
Keiko	Chida
Keiichi	Kumai
Yuriko	Kato
Junko	Takada
Konomi	Takahashi

Undergraduates and Graduate Students

Kou	Kato	(Graduate School of Science)
Takahiro	Aoki	(Graduate School of Science)
Aiko	Uchiyama	(Graduate School of Science)
Kousuke	Sakamoto	(Graduate School of Science)
Jun	Okamoto	(Faculty of Science)
Saki	Ito	(Faculty of Science)
Yu	Nasu	(Faculty of Science)
Tetsuro	Tago	(Graduate School of Pharmaceutical Sciences)
Takahiro	Tominaga	(Graduate School of Pharmaceutical Sciences)
Kazumi	Mikado	(Graduate School of Pharmaceutical Sciences)
Naoya	Sonoda	(Graduate School of Pharmaceutical Sciences)
Yujyu	Abe	(Graduate School of Pharmaceutical Sciences)
Azusa	Kazama	(Faculty of Pharmaceutical Sciences)
Ryo	Akita	(Faculty of Pharmaceutical Sciences)

Yoshimi	Hayakawa	(Faculty of Pharmaceutical Sciences)
Kosuke	Emura	(Faculty of Pharmaceutical Sciences)
Rei	Takeuchi	(Faculty of Pharmaceutical Sciences)
Rinn	Matsuda	(Graduate School of Medicine)
Akie	Inami	(Graduate School of Medicine)
Ying Hwey	Nai	(Graduate School of Medical Engineering)
Fairuz Binti	Mohd Nasir	(Graduate School of Medical Engineering)
Yuto	Nagao	(Graduate School of Medical Engineering)
Takayuki	Ose	(Graduate School of Medical Engineering)

Office Staff

Toshimitsu	Okamura
Katsuo	Aizawa
Shinichi	Suenaga
Shinya	Terui
Kyoko	Fujisawa
Kei	Ito
Nayoko	Aota
Ryoko	Ito
Fumiko	Mayama
Ikuko	Tojo

1) Research professor
2) Research fellow
3) SUMI-JU Accelerator Service Ltd.
4) Graduate School of Science
5) Graduate School of Engineering
6) Frontier Research Institute for Interdisciplinary Sciences
7) Institute of Development, Aging and Cancer
8) JSPS researcher
9) Graduate School of Medicine
10) Japan Radiation Protection Co., Ltd.

Edited by *Ren IWATA*
Ikuko TOJO

Published by *CYRIC PR Committee*